Fabrication and Characterization of Surfactant-Free PbSe Quantum Dot Films and PbSe-Polymer Hybrid Structures

by

Gayan S. Dedigamuwa

A dissertation submitted in partial fulfillment
of the requirement for the degree of
Doctor of Philosophy
Department of Physics
College of Arts and Sciences
University of South Florida

Major Professor: Sarath Witanachchi, Ph.D.
Pritish Mukherjee, Ph.D.
Hariharan Srikanth, Ph.D.
Xiaomei Jiang, Ph.D.

Date of Approval:
March 22, 2010

Keywords: thin films, lead selenide quantum dots, nanoparticles, multiple exciton generation, exciton dissociation, solar cells

ACKNOWLEDGMENTS

I would like to thank Dr. Sarath Witanachchi, my advisor for his suggestions and unwavering support. Everything I know about research has come from him. His vast experience and creativity helped me greatly along the way, and were essential to completion of this dissertation. I would also like to thank Dr. Pritish Mukherjee, Dr. Hariharan Srikanth and Dr. Xiaomei Jiang for agreeing to serve on my Committee and providing advice.

Further, I would also like to thank Dr. Xiaomei Jiang and Dr. Zhang for assisting me with colloidal PbSe nanoparticle growth and conducting optical measurements of my samples. Also I would like to thank all my lab mates specially Robert Hyde and Postdoctoral Associate Dr. Tara Dhakal for the assistance they gave me throughout this project.

And last, but not least, I would like to thank my wife Nilusha and my parents Premadase and Jayanthi who encouraged me along and helped me through the difficult times.

TABLE OF CONTENTS

LIST OF FIGURES

FABRICATION AND CHARACTERIZATION OF SURFACTANT FREE PbSe QUANTUM DOTS FILMS AND PbSe-POLYMER HYBRID STRUCTURES

Gayan S. Dedigamuwa

ABSTRACT

This work describes an experimental investigation of methods of synthesis, determination of structural and physical properties, and analysis and correlation of the properties to the structures of semiconductor quantum dots and quantum dot-polymer hybrid structures. These structures are investigated for applications in flexible solar cell devices. The main synthesis process used in the work was a Laser-Assisted Spray (LAS) process that was developed in our laboratory to deposit surfactant-free PbSe quantum dot (QD) films directly on a substrate. The QD films formed by this technique are in close contact with each other forming a percolation path for charge transport. Analytical instruments that include Atomic Force Microscopy (AFM) and Transmission Electron Microscopy (TEM) were used for structural characterization while optical absorption spectroscopy and photoluminescence were used for determining the quantum confinement of charge carriers in PbSe QDs. In addition, charge transport across

lithographically patterned paths was used to determine the transport characteristics and generation of photocurrent in the fabricated structures.

Absorption spectroscopy confirmed the quantum confinement of PbSe QDs deposited by LAS deposition. Room temperature current-voltage measurements across a 2μm tunnel junction formed by the QDs produced a power-law dependence of the form $I \propto V^{2.19}$ that describes a percolation path of dimensionality slightly above two-dimensional. Absence of surfactants in LAS deposited films improved the conductivity by more than three orders of magnitude. Temperature dependent conductance studies showed thermally activated transport at high temperatures and temperature independent tunneling followed by previously unobserved metallic conduction at low temperatures.

The LAS system was successfully modified by incorporating two spray nozzles to transport aerosols of two different precursors, one containing the QDs and the other containing the polymer. This new co-deposition system was successfully used to deposit QDs/Polymer hybrid structures. The TEM and XRD studies of LAS co-deposited films were shown to be uniformly distributed and crystalline. The photo-current experiments of QD/polymer hybrid composites showed clear evidence of enhanced carrier generation and transport as a result of intimate contact between quantum dots (QDs).

CHAPTER 1

INTRODUCTION & BACKGROUND

1.1.Advantage of Nanocrystalline Materials

Nanocrystalline materials have attracted tremendous interest in the chemistry and physics communities because of their novel properties. Nanocrystalline materials exhibit exceptional mechanical properties, representing an exciting new class of structural materials for technological applications. The advancement of this important field depends on the development of new fabrication methods, new characterization methods and an appreciation of the underlying nanoscale and interface effects. The first major identifiable activity in the field of nanocrystalline (or nanostructured, or nanophase) materials was reported in the early 1980s by Gleiter and coworkers [1], who synthesized ultrafine-grained materials by the in-situ consolidation of nanoscale atomic clusters. The ultra-small size (< 100 nm) of the grains in these nanocrystalline materials can result in dramatically improved or different properties from conventional grain-size (> 1 μm) polycrystalline or single crystal materials of the same chemical composition. The differences were attributed to two main physical phenomena that become prominent as the material dimension changes from three dimensions (3D) to zero dimension (0D). These include classical mechanical effects [2], as well as quantum mechanical effects, for example the

"quantum size effect" where the electronic and optical properties of solids are altered due to changes in the band structures. Additionally, the enhanced surface/volume ratio in nano dimensions forces more than 33% of the atoms to be on the surface (for 10nm dot [35]), drastically altering the physical properties such as having lower melting temperature and lower sintering temperature, and higher diffusion force at elevated temperatures.

Electronic devices incorporating nanocrystalline materials are being extensively studied to exploit the unique electrical and optical properties that arise from "quantum-confinement" of charge carriers. A good example of the manipulation of optical properties is variation of emission spectra obtained from different size Cadmium Selenide (CdSe) quantum dots.[3]

Fig. 1.1: The image above represents the fluorescent-emission colors of cadmium selenide nanocrystals, or "quantum dots," excited with a near-ultraviolet lamp [3]

The excitation fluorescence depends on the nanocrystal size which is characteristic of the particle's band gap energy. As the physical dimensions of the particle become smaller, the band gap energy becomes higher. Therefore, different size particles of the same material have different band gaps and therefore emit different colors.

Since particle size determines the optical and electrical properties, as demonstrated for CdSe, ability to produce monodispersed pure nanoparticles with a narrow size distribution is very important. The average size and the size distribution of the nanoparticles are largely determined by the technique that is used to produce them. Out of many techniques developed to fabricate nanoparticles, chemical precipitation techniques are the most suitable for producing narrow particle distributions.

1.2. Semiconductor Nanocrystals (Quantum Dots)

In a bulk semiconductor material, the energy levels are closely spaced within bands. The number of available energy levels given in an interval of energy is described as the density of state. In the case of a bulk semiconductor the top occupied band, known as the valence band, is mostly filled. The conduction band of a semiconductor is mostly empty, and it is separated from the valance band by a bad gap where the density of states within the gap for a pure semiconductor is zero. Electrons in the valence band are not free electrons because they are bonded by Coulomb forces formed by the nucleus and the covalent bonds formed by the neighboring electrons. If an electron in the valence band gains energy that is greater than or equal to band gap energy, the electron can breaks these bonds to dissociate from the atom and become associated with the conduction band,

yet subjected to the periodic potentials of the lattice. This process therefore, forms an electron and a hole in the conduction and valance bands, respectively. This vacancy can be filled easily by another electron in the valence band. In other words, the vacancy can move freely in the layers due to continuous density of state in the bulk material. Since this generated electron and hole pair can move freely in the lattice of the bulk semiconductor, the pairs are unbounded. When a semiconductor having bulk properties is reduced in size to a few hundred atoms (zero dimension), the density of states in valence and conduction band is changed drastically. The continuous density of state in the bands is replaced by a set of discrete energy levels, *i.e* S, P and D levels, which may have energy level spacing, e.g. $E_p - E_s$, much larger than the thermal energy $k_B T$ (at room temperature). This new arrangement of density of states in quantum levels changes the optical and electronic properties of the material.[4]

In semiconductor quantum dots, excitation of an electron by optical radiation into the unfilled conduction band to create an electron-hole pair requires more energy that that required by a bulk semiconductor of the same material.[4] In quantum dot, the electron-hole pairs generated by absorption of photons are not free as in bulk material because of the discrete nature of the energy levels. These bound electron-hole pairs are known as excitons. Also, when the electron and hole are confined within a particle dimension that is closer to or less than the Bohr exciton size, they interact strongly with one another through Coulomb forces. As the size of a semiconductor nanocrystal decreases below the bulk semiconductor Bohr exciton size, the exciton experiences increasingly strong confinement effects which significantly alter the allowed energy levels and result in increasingly discrete electronic structures. [4]

In theory, the separation of energy levels is mainly governed by the dimensionality of the semiconductor dot. As explained in the above section, when the size of the material is reduced from bulk to nano, the density of state is changed from being continuous to discrete by replacing continuous energy band with discrete energy levels. Then these discrete levels can be found by solving the Schrodinger equation for different particle dimensions.

In the case of a bulk semiconductor material, electron wavefunction is delocalized and allows electrons to move freely throughout the entire medium. Then, one can use free particle wavefuction without any confinement condition to solve the Schrodinger equation for finding possible energy values. According to this analysis the energy of the electron in three-dimensional (3D) free space can be expressed as

$$E(k) = \frac{\hbar^2\left(k_x^2+k_y^2+k_z^2\right)}{2m_e^*} \qquad (1)$$

where k is a wave vector and m_e^* is the effective mass of an electron. As the dimensions of the semiconductor is reduced, the energy of the discrete states for 2D (thin films), 1D (nano wires) and 0D (quantum dots) for spatial dimensions of *Lx*, *Ly*, and *Lz* can be given by,

For 2D $$E(k) = \frac{h^2 n_x^2}{8m_e^* L_x^2} + \frac{\hbar^2\left(k_y^2+k_z^2\right)}{2m_e^*} \qquad (2)$$

For 1D $$E(k) = \frac{h^2}{8m_e^*}\left(\frac{n_x^2}{L_x^2} + \frac{n_y^2}{L_y^2}\right) + \frac{\hbar^2(k_z^2)}{2m_e^*} \qquad (3)$$

And for 0D $$E(k) = \frac{h^2}{8m_e^*}\left(\frac{n_x^2}{L_x^2} + \frac{n_y^2}{L_y^2} + \frac{n_z^2}{L_z^2}\right) \qquad (4)$$

Where $k_x = \pi\left(\frac{n_x^2}{L_x^2}\right)^{1/2}$, $k_y = \pi\left(\frac{n_y^2}{L_y^2}\right)^{1/2}$, and $k_z = \pi\left(\frac{n_z^2}{L_z^2}\right)^{1/2}$ for a bound quantum dot.

Similarly, the energy eigen values for spherical quantum dots are given by, [5]

$$E^h = \frac{\hbar^2}{2m_h}\left(\frac{\alpha_{n_h \ell_h}}{R}\right)^2 \qquad (5)$$

$$E^e = E_g + \frac{\hbar^2}{2m_e}\left(\frac{\alpha_{n_e \ell_e}}{R}\right)^2 \qquad (6)$$

$$E = E^h + E^e = E_g + \frac{\hbar^2}{2m_e}\left(\frac{\alpha_{n_e \ell_e}}{R}\right)^2 + \frac{\hbar^2}{2m_h}\left(\frac{\alpha_{n_h \ell_h}}{R}\right)^2 \qquad (7)$$

In these equations $\alpha_{n_e \ell_e}$ is the n^{th} root of the ℓ^{th} order Bessel function for the electron while $\alpha_{n_h \ell_h}$ is the n^{th} root of the ℓ^{th} order Bessel function for the hole.

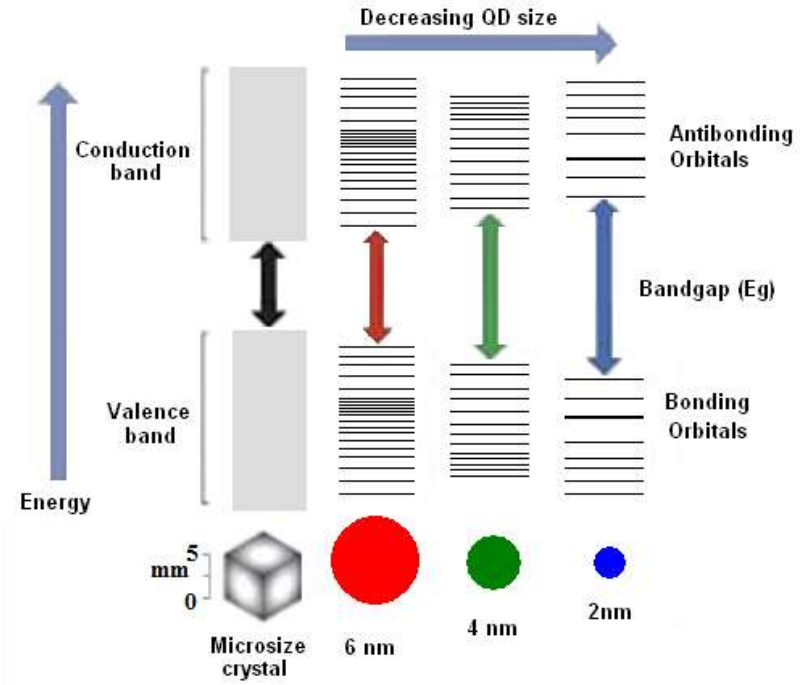

Fig.1. 2: change in band-gap energy E_g with particle size.

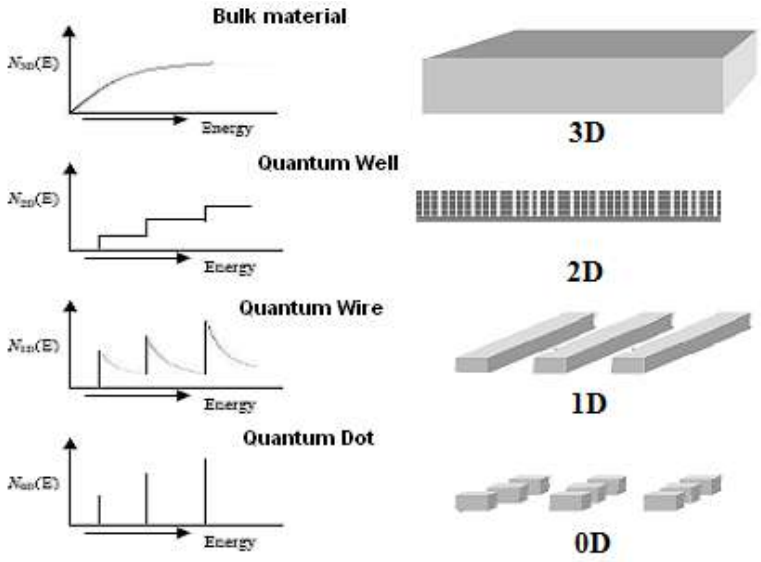

Fig.1.3: The progression of confinement and effects on the density of states.

Additionally, E_g is the band gap energy for the bulk semiconductor material. According to Eq.7, the effective band gap, the energy required by an electron to transfer from the highest valence band energy to the lowest conduction band energy, increases with decreasing particle size. The Fig.1.2 shows the increasing bandgap energy and intra-band spacing with quantum confinement.

The quantum confinement effect is what allows the tuning of absorption and emission wavelengths over the entire visible spectrum as a function of quantum dot size. As is shown in Fig. 1.2 and 1.3, the density of states changes from being continuous at all energy levels for a bulk material to becoming discrete transitions at certain energy levels for the quantum dot.

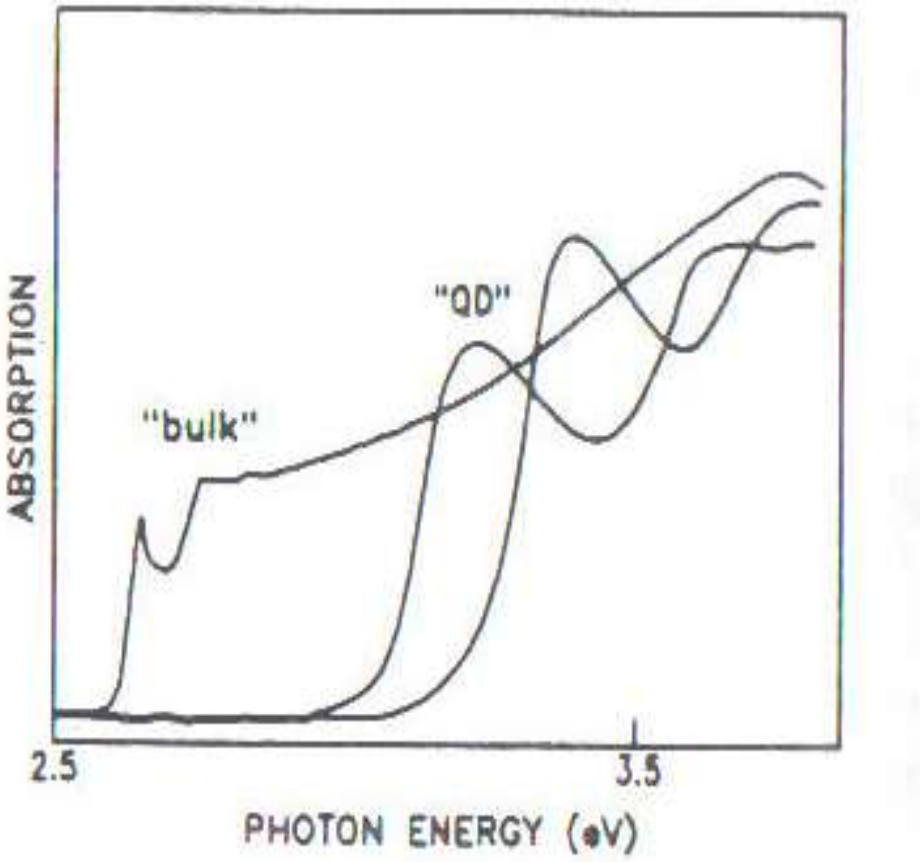

Fig. 1.4: Linear absorption spectra at 10K of CdS crystalline in glass. The two spectra labeled "QD" refers to two samples with small crystal sizes in the quantum-confinement regime. The bulk sample has large crystal sizes, exhibiting bulk CdS properties. [6]

Furthermore, the quantum-mechanical wave functions of electrons and holes are confined within the limits of the material. Hence, when the confinement increases, the wave functions also become more localized .[5] Quantum confinement leads to altered emission lifetimes as well as altered luminescence quantum efficiency in quantum dots .[6] Additionally, quantum confined structures exhibit a shifted band edge that allows the production of varied emission peak wavelengths as dictated by the strength of the confinement (i.e. the size of the quantum dot) (Fig1.4).

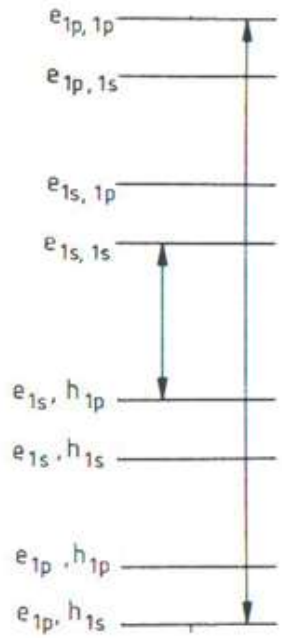

Fig. 1.5: Schematic representation of the electron-hole pair transition in a semiconductor quantum dot.

Fig. 1.4 displays the absorption spectra for bulk and quantum dot CdS sample at a temperature of T=10K. The lower temperature reduces the phonon broadening which was not discussed within the previous theoretical discussion of energy levels and increasing confinement. Several effects are omitted for simplicity's sake that must be mentioned here. The two peaks observed in CdS quatum dot samples show the simultaneous electron-hole transition between the inter-bands during the light absorption. The first peak shows the $1S_e$-$1S_h$, 1st intraband transition, while second peak shows the $1S_e$-$1P_h$/$1S_h$-$1P_e$, 2^{nd} intraband transition (Fig. 1.5). The transition lines in Fig 1.4 are much broader than transitions in bulk materials. The width of the transition results from

homogeneous and inhomogeneous broadening effects that cause the theoretically discrete transitions to become Gaussian distributions of transitions.

Homogeneous broadening is the result of phonon and other scattering effects that occur during the excited electron's lifetime. Inhomogeneous broadening effects occur because, when looking at a set of quantum dots, there is a distribution of sizes and aspect ratios that translate into a small distribution of emission wavelengths rather than performing as a single discrete transition.

The electrical and optical properties of semiconductor nanoparticles are mainly governed by the quantum size effects. The size of the structure limits the exciton-Bohr radius of the bound electron-hole pairs, leading to altered electronic and optical properties, and causes high surface energy, which alters the physical properties.[7] The physical material is actually smaller than the natural exciton-Bohr radius (i.e. radius of lowest energy Bohr orbital). For Si this is reached at 4.9 nm, for PbSe at 6.1 nm, defined to be:

$$a_B = \frac{e_o h^2}{m_r e^2} \qquad (8)$$

where e_o is the dielectric constant of the Quantum Dot (QD) (at low frequencies), h is Planck's constant, and m_r is the reduced electron-hole mass.[7]

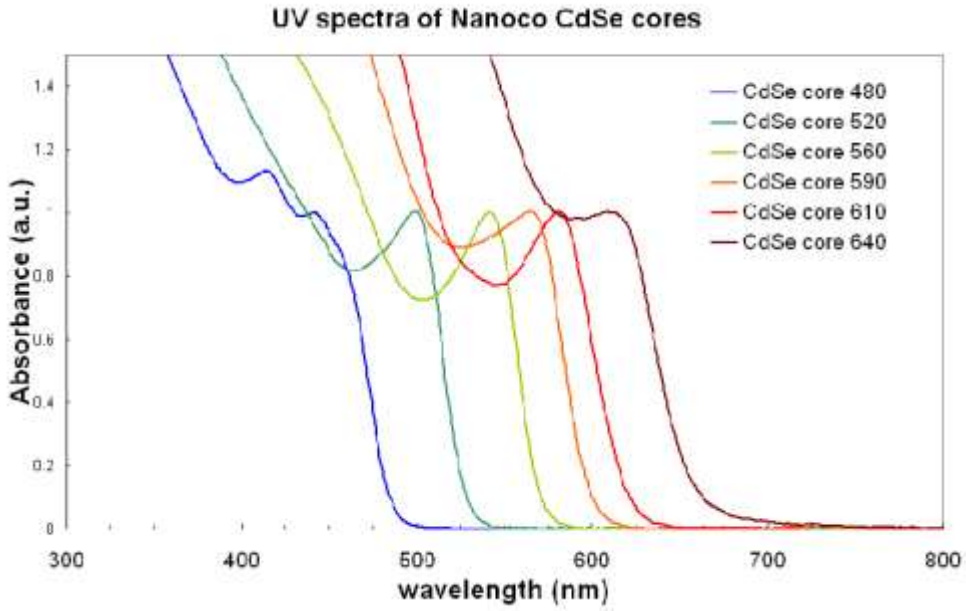

Fig. 1.6: An example of size related absorbance of the CdSe QDs. The peaks determine the 1S transition of each QDs size distribution. (Image taken from Sigma-Aldrich Material Sciences website.)

1.3. Semiconductor-based Conventional Solar Cells

Bulk semiconductors absorb optical photons to generate unbound e-h pairs. Bandgap (E_g) of the semiconductor material plays an important role in the process of photo-generation. In an ideal case, photons with an energy $hv < E_g$ will not contribute to the photo-generation, whereas all photons with an energy $hv > E_g$ will each contribute to the photo-generated electron-hole pair followed by spontaneous recombination. If these electron-hole pairs can be separated before they spontaneously recombine, a current can be generated. However, several energy-loss mechanisms limit the current extraction from such a device. When an electron is excited to a level above the edge of the conduction band, the energy in excess of the band gap will be lost as heat as a result of e-

phonon coupling, and the electron is relaxed to the edge of the conduction band. Finally, the electron at the band edge will spontaneously recombine with a hole, radiatively or non-radiatively. Schematic diagram in Fig. 1.7 shows a semiconductor based traditional p-n junction solar cell.

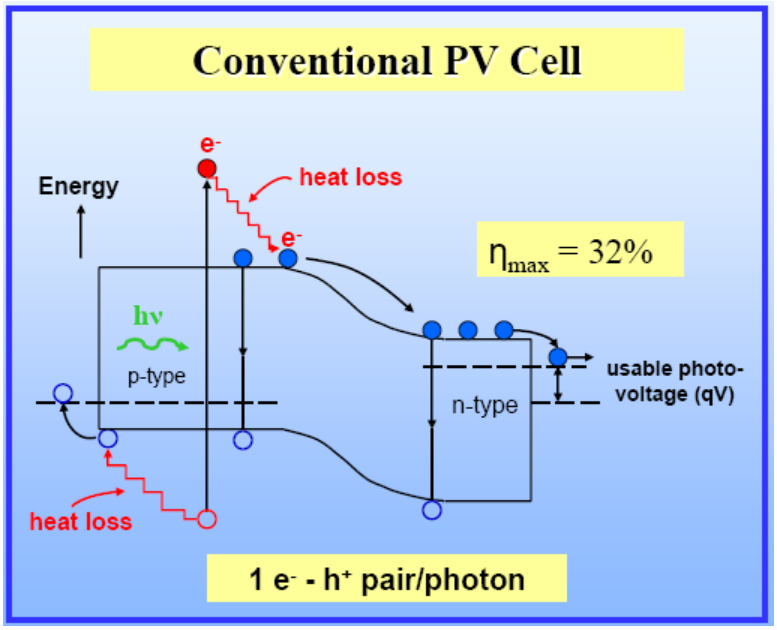

Fig. 1.7: Schematic diagram of a semiconductor based traditional pn junction solar cell (Fig taken from J. Nozik, NREL report).

As a result of above-discussed energy loss mechanisms, and considering the fact that one photon generates only one e-h pair, the maximum achievable efficiency of a solar device has been computed to be 33%.Traditional single junction silicon solar cells today exhibit efficiencies between 11-20% as a result of light loss due to reflection from the front surface of the cell, shadowing by the electrical contacts, and ohmic losses at the semiconductor/electrode junctions.

1.4. Absorption of Solar Radiation by Semiconductors

Examination of the solar spectrum (Fig. 1.8) reveals that the optimum coupling of sunlight should take place in the wavelength region of 300-1100 nm (4 eV- 1.1 eV). Typical silicon solar cells (band gap 1.1eV) absorb all the radiation left of the red line (90% of sun light).

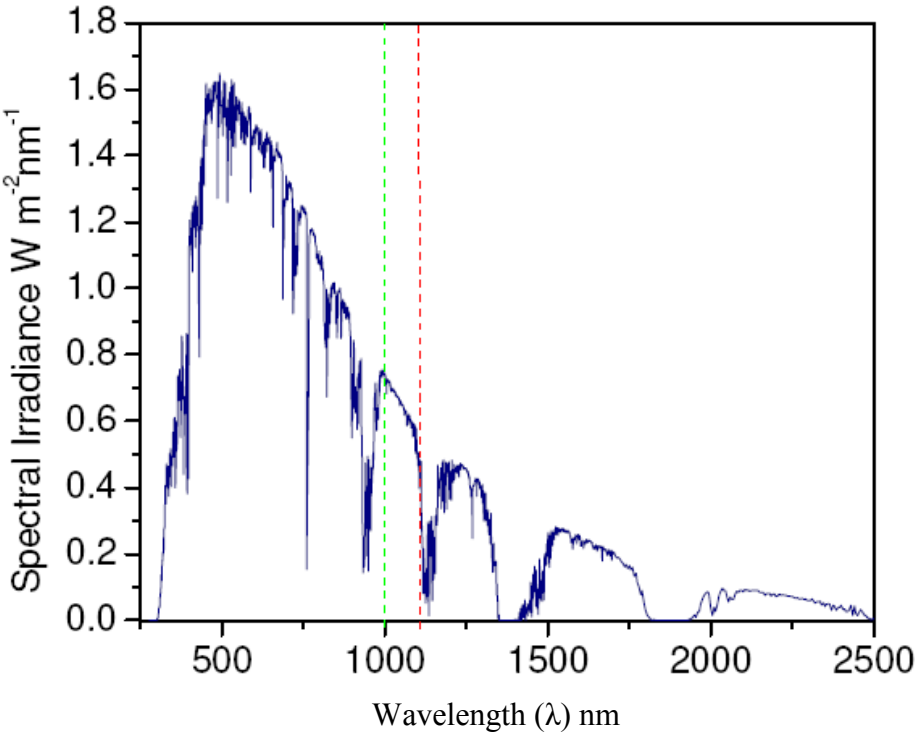

Fig. 1.8: Air Mass (AM) 1.5 solar spectrum. The dashed lines in green and red represent limits of organic and silicon based solar cells, respectively. (Taken from :www.solems.com/Radiometry-basics)

The Air mass 1.5 (AM1.5), the conventional spectrum used in the photovoltaic industry, corresponds to the sun being at an angle of elevation of 42^0 and at an integrated power density of 100 mW cm^{-2}. Referring to the AM1.5 spectrum shown in Fig. 1.8, close to 50% of the sun's energy lies in the infrared.

As a result, the optimal bandgaps for solar cells in both the single-junction and even the tandem architectures lie beyond 850 nm. High efficiency multijunction solar cells offer the prospect of exceeding 40% efficiency [8] through the inclusion of infrared-bandgap materials. For double and triple junction solar cells, the smallest-bandgap junction optimally lies at 1320 nm and 1750 nm respectively [8]. When the absorber band gap is optimized around 1.1-1.4 eV, the excess energy of high energy photons are wasted as heat. This is one of the main limiting factors of the conventional p-n junction solar devices.

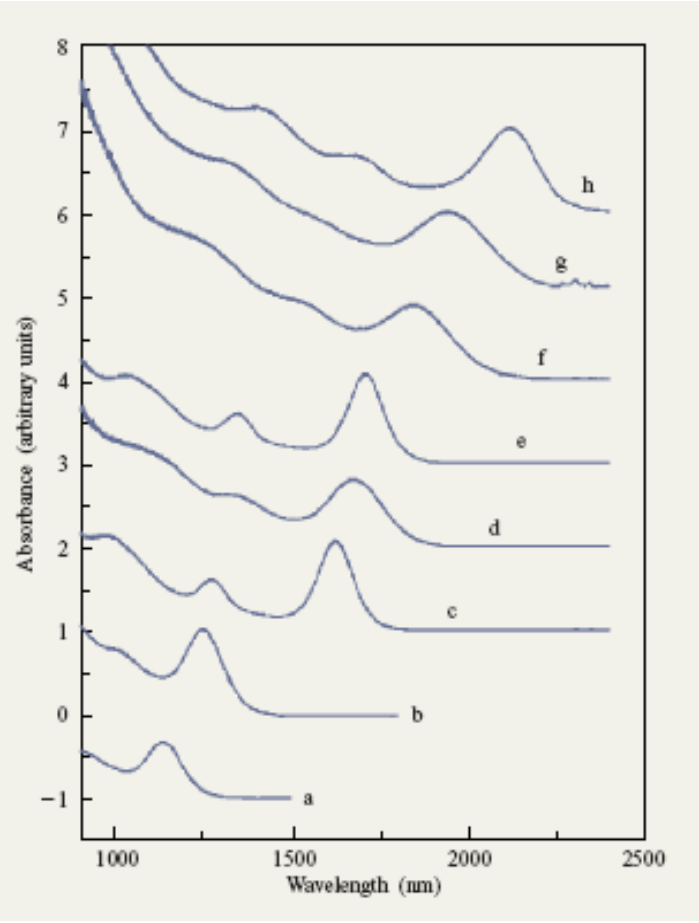

Fig.1.9: Room-temperature optical absorption spectra for a series of PbSe NC samples measuring (a) 3.0 nm, (b) 3.5 nm, (c) 4.5 nm, (d) 5 nm, (e) 5.5 nm, (f) 7 nm, (g) 8 nm, and (h) 9 nm in diameter.[53]

1.5. PbSe Quantum Dots (QDs)

PbSe is a direct band gap semiconductor with a bandgap of 0.26eV that corresponds to absorption wavelength of 4770nm. As a result of the long wavelength, PbSe nanoparticles found application in IR detectors. However, reducing crystal size to a few nanometers can bring the band gap into visible region. A PbSe QD diameter of 5.7 nm will have a band gap of 0.72 eV, corresponding to absorption wavelength of 1720nm, compared to bulk of 0.26 eV.[6]

While size tunability of QDs enable manipulation of the band gap, shown in Fig. 1.9 , large Bohr radius (23nm) allows PbSe to provide an alternate way to change the band gap and quantum levels without having to decrease the QD size very much. This allows larger QD sizes to have higher photon absorption cross-sections. Also the equal effective electron and hole mass in PbSe allows strong quantum confinement, due to phonon bottle neck in both valance and conduction band, compared to other semiconductor materials such as Cadmium selenide, Indium phosphate, Gallium Arsenide etc.(Fig. 1.10). This strong quantum confinement in the PbSe QDs provides a unique opportunity for electro-optical applications. Also researchers have shown that due to phonon bottle neck in both valance and conduction band, the Multiple Exciton Generation (MEG) in PbSe NCs is highly efficient, extremely fast, and occurs in wavelength range that has a potential to provide significantly increased solar cell power conversion efficiency.[6]

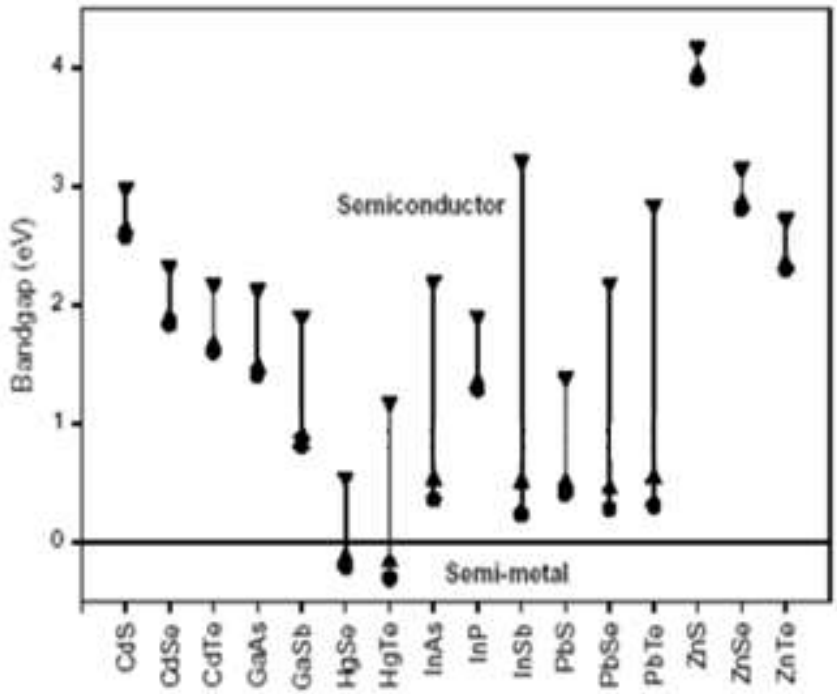

Fig.1.10: Bandgap increment in various semiconductor QDs due to quantum confinement (from bulk to 3.9nm). (Taken from H. Weller, *Pure Appl. Chem.* 72, 295 (2000).)

In bulk semiconductors, the absorption of one photon of energy greater than the bandgap leads to one electron-hole pair by losing the excess energy as heat through electron-phonon scattering and subsequent phonon emission, as the hot photogenerated carriers (hot carrier) relax to their respective band edges (Fig. 1.7). The main approach to reduce this loss in efficiency has been to use a stack of cascaded multiple p-n junctions with bandgaps better matched to the solar spectrum (Fig. 1.8). In the limit of an infinite stack of bandgaps perfectly matched to the solar spectrum, the ultimate conversion efficiency at one-sun intensity can increase to about 66%.[6]

Another approach is to use the hot carriers before they relax to the band edge via phonon emission.[6] There are two fundamental ways to use the hot carriers for enhancing the efficiency of photon conversion. One way produces an enhanced photovoltage, and

the other way produces an enhanced photocurrent. The former requires that the carriers be extracted from the photoconverter before they cool [6]. To achieve the enhanced photovoltage, the rates of photogenerated carrier separation, transport, and interfacial transfer across the contacts to the semiconductor must all be fast compared to the rate of carrier cooling. The latter requires the energetic hot carriers to produce a second (or more) electron-hole pair (Fig. 1.11). The formation of multiple electron-hole pairs per absorbed photon is a process explained by impact ionization (I.I.). In this process, an electron or hole with kinetic energy greater than the semiconductor bandgap produces one or more additional electron-hole pairs. The kinetic energy can be created either by applying an electric field or by absorbing a photon with energy above the semiconductor bandgap energy. In order to have efficient multiple exciton generation, [6] the rate of impact ionization has to be greater than the rate of carrier cooling and other relaxation processes for hot carriers.

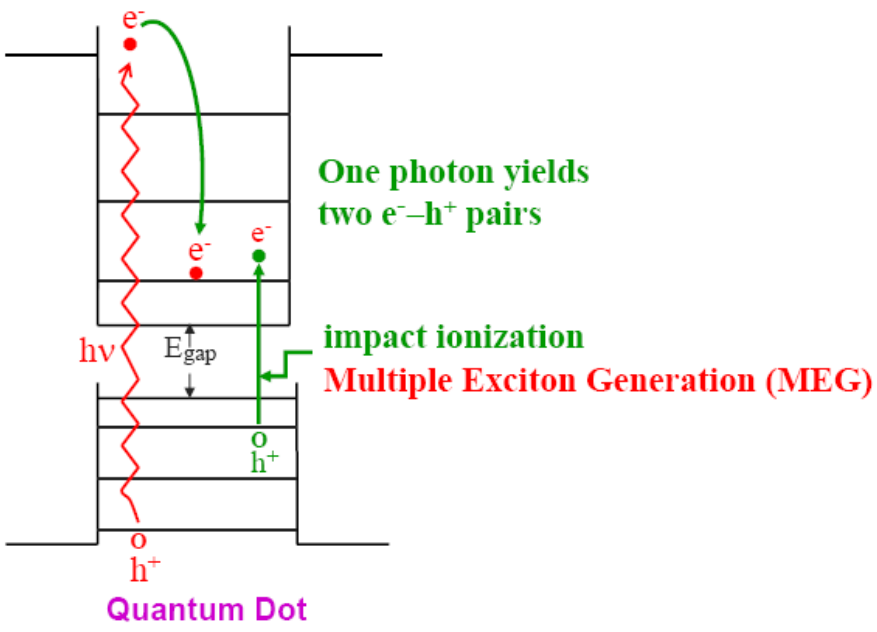

Fig.1.11: Multiple excitons generation of quantum dot PV solar cells
(Taken from J. Nozik, NERL)

In quantum dots, the relaxation dynamics of photogenerated carriers are largely affected by the quantization effects. The reason for that is, when the carriers in the semiconductor are confined by a potential barrier to a region of space that is smaller than or comparable to their deBroglie wavelength or to Bohr radius of excitons in the semiconcuctor bulk, the cooling rate of hot carriers is dramatically reduced, and the rate of impact ionization could become competitive with the rate of carrier cooling.[9]

The threshold photon energy for multiexciton generation is given by $hv = \left(2 + \frac{m_e^*}{m_h^*}\right) E_g$ where, m_e^* and m_h^* are electron and hole effective masses, respectively and E_g is the bandgap of the quantum dot. If $m_e^* \approx m_h^*$,which is the case for PbSe , the excess energy of the initial exciton will be equally shared between the electron and the hole in generating the second e-h pair, and thus, the threshold energy for carrier multiplication is $\geq 3Eg$ [9]. For example, 9.5nm QD where band gap is .65eV can harvest maximum solar power according to the AM 1.5 solar spectrum shown in Fig 1.8.

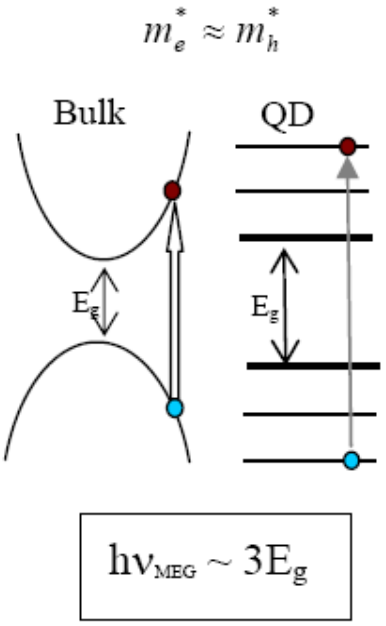

Fig.1.12: Comparison of energy levels and threshold energy for MEG in QDs for (a) $m_e^* \sim m_h^*$.

1.5.1. Exciton Dissociation

The success of electronic devices based on semiconductor quantum dots hinges on the ability to efficiently extract charge carriers from QD and to transport the carriers between electrodes. For example, in quantum dot photovoltaic devices, bound electron-hole pairs (excitons) generated by light absorption must be dissociated and the resulting carriers must be collected by electrodes.[10] This mechanism depends on several properties of the interface between the QD and the transporting medium. (1) The coupling between QD and transporting medium must be strong enough to separate the electron-hole pairs either by charge transfer across the boundary or diffusing one exciton to the next medium prior to non-radiative Auger recombination. (2) Intimate contact between the QD and the transporting medium, which lowers the interface traps. (3) Large cross section area between the QD and transporting medium. (4) Built-in electric field between electrodes to drive the charges to electrodes. Polymer/QD composites have been recognized to posse both the attributes where charge separation is enhanced at interfaces and the electron and hole transport takes place in two different materials[11].The most important parameters that control exciton dissociation are; ionization potential, electron affinity, band gaps of polymer and QD, density of QDs, distribution of QDs within the polymer, and the nature of contact between polymer and QD. The effect of these parameters on exciton dissociation is discussed below.

Choice of the polymer is crucial for effective coupling between the QD and the polymer. In order for the holes in the QD to transfer into the HOMO level of the polymer, the ionization potential of the polymer must be less than that for the QD. Similarly,

transfer of an electron in the LUMO level of the polymer to the QD is possible only if electron affinity of the QD is higher than that of the polymer.

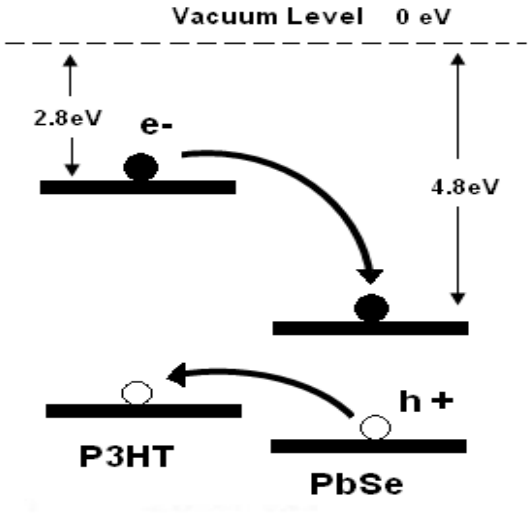

Fig.1.13: The schematic energy level diagram for PbSe nanodots and P3HT(polymer) showing the charge transfer of electrons to PbSe and holes to P3HT.

The range of diffusion for excitons in polymers is 5-15nm [11]. Only the excitons generated close to an interface can be dissociated. For this reason, density of QDs in the polymer plays a crucial role in dissociation of excitons in the polymer. Therefore, it is important to maintain an optimum density of QD for a given system for efficient dissociation process.

Uniform distribution of QDs within the polymer is important to avoid formation of isolated QD aggregates surrounded by polymer. Electrons accumulated in QD aggregates become trapped and eventually lead to carrier recombination. Such aggregation is readily observed in polymer/QD composites when surfactants are removed prior to mixing [12]. Therefore, the removal of surfactant has to happen just before the QDs are mixed with the polymer. Several chemical treatments including hydrazine (N_2H_4) treatment have been developed to remove the surfactant coating from QDs that are

deposited on substrates [13]. However, to fabricate QD/host composite structures, chemical washing to remove surfactants has to be done prior to embedding them in the host, which inevitably leads to agglomeration and non-uniform distribution of the QDs in the host material. Therefore, washing-off of the organic surfactant using a hydrazine solution is not suitable to make a composite of quantum dots and polymers. In addition, toxicity of hydrazine is also a concern.

The nature of the contact between the polymer and the quantum dot is important for fast dissociation. If QD makes an intimate contact with the polymer such that there is significant overlap of the wave functions between the two materials, tunneling of one charge carrier type of the exciton into the other material is energetically favorable [14]. This mechanism that is dominant in QDs without surfactants is known as the Dexter mechanism [14]. If there is a significant spectral overlap between the emission and absorption spectrum of the two materials, a Coulomb dipole-dipole interaction promotes energy transfer between the two materials. This mechanism that is not hindered by the presence of an interfacial surfactant layer is known as the Forster mechanism.[14] Exciton dissociation through Dexter and Forster mechanisms are shown in Fig. 1.14. [15,16]

According to the diagram in Fig 1.14, in order to have an efficient Forster mechanism, the band gap of the QD and the polymer have to be in the same range. For example, single exciton dissociation in surfactant-coated CdSe nanoparticles (band gap 2.0-2.6 eV) and the polymer MEH-PPV (*poly[2-methoxy-5-(2'-ethyl-hexyloxy)-p-phenylenevinylene*), band-gap ~2.1 eV, have been observed while such a transition is absent in MEH-PPV and surfactant coated QDs of CdS (band gap 2.6-3.1 eV)[14].

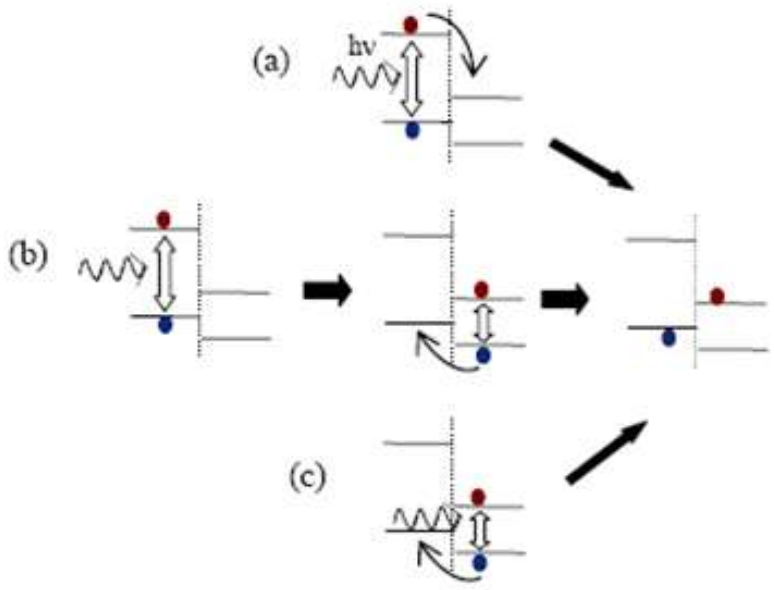

Fig.1.14: Possible paths for exciton dissociation in polymer/QD composites. (a) Generation of an exciton in polymer followed by electron transfer to QD by Dexter mechanism. (b) Generation of an exciton in polymer followed by exciton transfer to QD by Forster mechanism. Exciton in QD can dissociate by transferring the hole to the polymer. (c) Generation of an exciton in QD and transfer of the hole to the polymer by Dexter mechanism.

In order to have an efficient Dexter mechanism, the surfactant has to be removed from the quantum dot during the interaction. Efficient exciton dissociation between uncoated CdS and MEH-PPV has been observed due to the Dexter mechanism. [14] Finally, these results have led to the conclusion that for a polymer/QD composite where the band gaps of the two materials are far apart, presence of surfactants at the interface suppresses the exciton dissociation process. Therefore, one of the primary focuses of this project is to develop a method to deposit surfactant-free quantum dots on a substrate and to produce QDs/Polymer hybrid structure with direct contact between quantum dots and the polymer.

CHAPTER 2

NANOCRYSTALLINE GROWTH & PROPERTY CHARACTERIZATION TECHNIQUES

2.1. Nanoparticle Synthesis

Currently, there are several different techniques available for nanoparticle growth that include sol-gel processing [17], chemical synthesis [18], chemical vapour deposition (CVD) [19], plasma or flame spray synthesis [20], laser pyrolysis [21], and atomic or molecular condensation [22]. Chemical synthesis permits the manipulation of matter at the molecular level. Because of mixing at the molecular level, good chemical homogeneity can be achieved. Also, by understanding the relationship between how matter is assembled on an atomic and molecular level and the resulting macroscopic properties, molecular synthetic chemistry can be tailored to prepare novel compounds.

2.1.1. Chemical Synthesis of Nanoparticles

Chemical synthesis is a well-established industrial process for the generation of colloidal nanoparticles from liquid phase. Nanoparticles with diameters in the range of 1 to 15 nm with narrow distributions have been chemically synthesized. Typical size

variances are about 20%; however, for measurable enhancement of the quantum effect, this must be reduced to less than 5% [53]. Size distribution of semiconductor, metal and metal oxide nanoparticles can be manipulated by either dopant introduction [23]or heat treatment [24]. Better size and stability control of quantum-confined semiconductor nanoparticles can be achieved through the use of inverted micelles [25], polymer matrix architecture based on block copolymers [26] or polymer blends [27], porous glasses [28], and ex-situ particle-capping techniques [29]. However, these techniques involve elaborate steps of solid–liquid separation, washing, and drying to separate the nanoparticles for applications.

As a result of the large surface area-to-volume ratio of nanoparticles, the Van der Waal's attraction between adjacent particles is considerably high. These forces tend to cause agglomeration of particles as they are formed. Surfactants are used to prevent agglomeration in almost all the chemical processes. The surfactants coat the particles and prevent them from aggregating. When the nanoparticles are close to each other, they encounter a repulsive potential stemming from surface-bound organic molecules.

The organic surfactants consist of head groups that "stick" to the nanoparticle surface via dative bonds, actual covalent bonds or electrostatic attraction. The surfactant molecule also possesses a "tail" which points away from the nanoparticle surface, extending into the surrounding liquid medium as shown in Fig. 2.1. This tail is important because its polar/nonpolar nature dictates the nanoparticle solubility within the surrounding organic or aqueous media. For many chemically synthesized nanoparticles, their primary solubility will be within organic solvents.

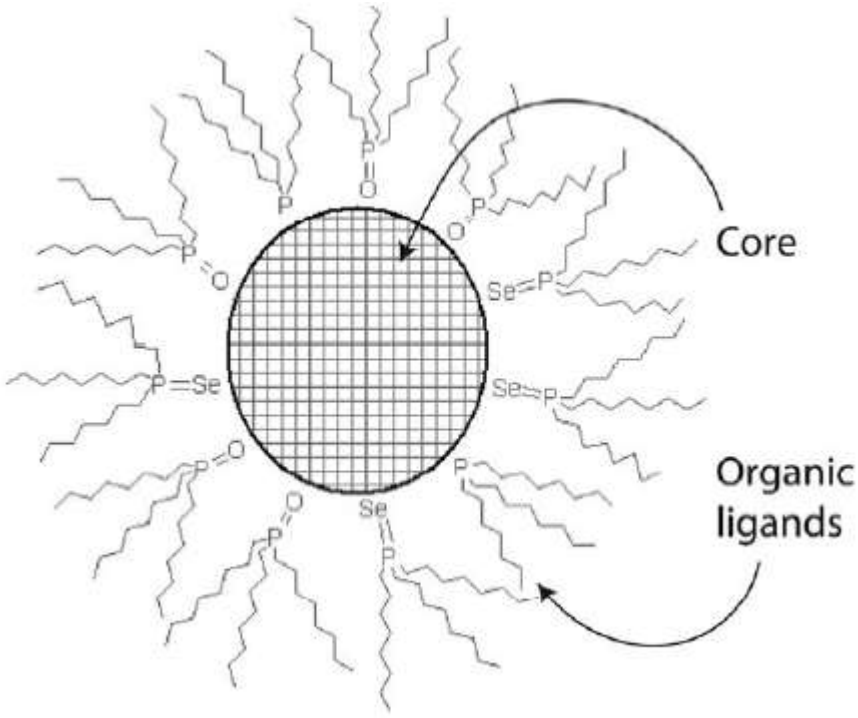

Fig. 2.1: The figure shows the Surfactant coated nanoparticle. Head groups of the surfactant attaches to the particle while tails are extended to the surrounding liquid (Taken from http://www.freepatentsonline.com/.)

2.2. Spray Pyrolysis

Spray Pyrolysis technique has been used for the growth of coatings of a variety of materials, including semiconductors and oxides.[30] The main component of a spray pyrolysis system is an atomizer that generates microdroplets of a precursor solution dissolved in a relatively volatile solvent. The droplets, in the form of a fine spray, are carried out of a nozzle onto a heated substrate by a carrier gas that can be inert or reactive. The constituents of the droplets decompose and react on the hot substrate to form the chemical compound. The substrate temperature should be high enough to evaporate the volatile solvents. The spray nozzle is usually scanned continuously during

the growth to coat a large area of the substrate. Even though this technique produces low quality films compared to Chemical Vapor Deposition (CVD) or Sputtering, it has been used over the years due to numerous advantages such as simplicity, low cost, non toxic precursors, good reproducibility and no need for high vacuum.

2.3. Laser Assisted Spray Process

Laser Assisted Spray (LAS) techniques have been used to generate nanaocrystalline powders and coatings.[31] In contrast to the spray pyrolysis, the droplets interact with a continuous wave laser beam as they come out of the nozzle. If the molecules of the precursor have a strong absorption band at the wavelength of laser beam, the molecule is dissociated. This method has been used to form amorphous nanoparticles of Si/N/C.[32] However, this method is restricted to compounds that have resonance absorption bands at an available laser wavelength.

The sizes of the produced droplets depend on the technique used to atomize the solution. The simplest way to generate an aerosol spray is by a pneumatic process. In this method, the pressure drop at the orifice of a nozzle from a high flow rate of gas causes the dispersion of the solution into microdroplets. However, control of the particle size distribution produced by this method is very difficult. On the other hand, ultrasonic nebulizers (model 241CST; Sonaer Ultrasonic, Farmingdale, NY) are known to produce a fairly uniform distribution of micrometer-size droplets. Generally, the nebulizer is operated at a frequency of 2.4MHz, where the precursor solution is converted into an aerosol of particles in a range of 1-2μm in diameter. These particles have lack sufficient

inertia and thus have to be transported by a carrier gas. Because the aerosol-generating rate is independent of the gas flow rate, the transport of the droplets to the substrate can be controlled without affecting the function of the nebulizer.

When the droplets impinge upon the heated substrate, the precursor is decomposed to form the compound. The subsequent film formation and the morphology of the film are dependent on the velocity of the drop, the rate of reaction, and the rate of evaporation of the solvent. At high velocities, the droplets will flatten on the substrate leading to large particle size.[33] If most of the solvent is evaporated by the laser heating, the salt in the drop condenses into a solid particle and thus forms a smaller grain on the substrate. Therefore, by controlling the concentration of the solvent, the size of the grains deposited on the substrate can be controlled.

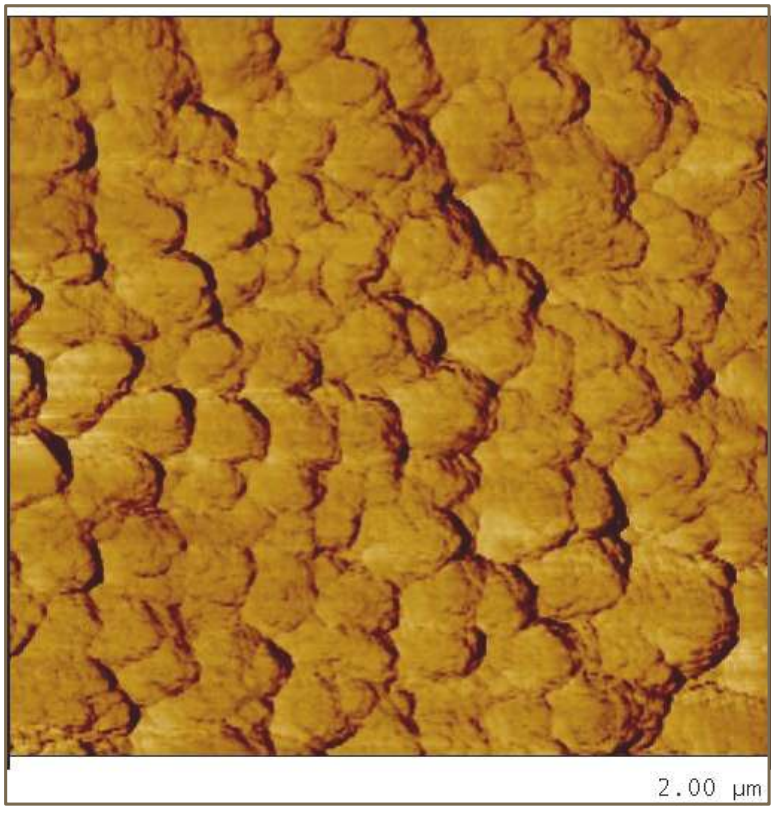

(a)

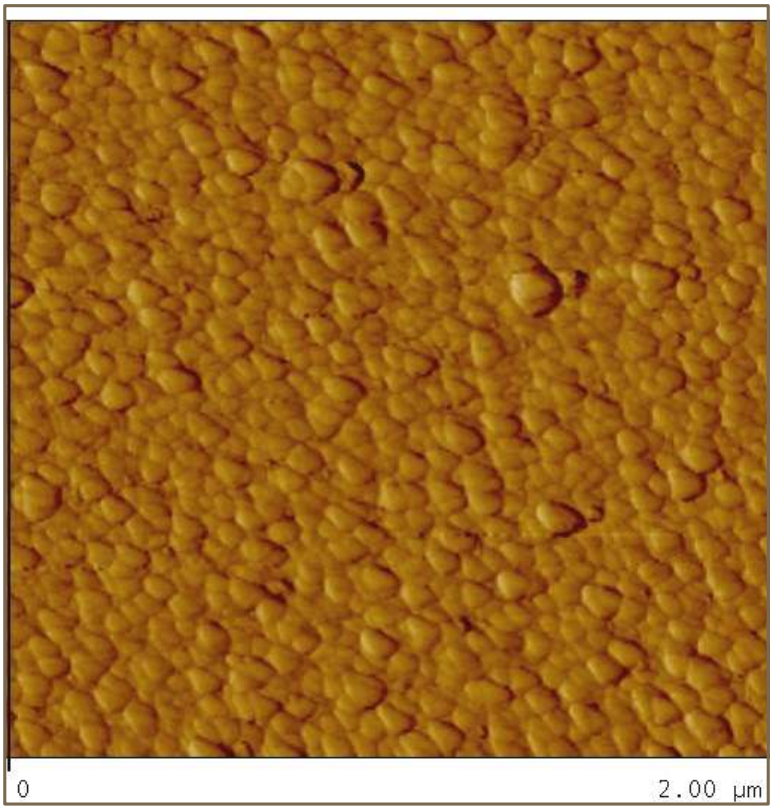

(b)

Fig.2.2: Particle size difference between regular spray pyrolysis Vs Laser-assisted spray process (a) AFM image of film deposited by regular spray pyrolysis (b) AFM image of the film deposited by LAS technique.

The Fig.2.2 shows the difference between Regular spray pyrolysis vs Laser-assisted spray pyrolysis. The average particle size in regular spray pyrolysis is about 250nm. Also irregular particle shape and size is visible due to flattening of the drops on the substrate. In comparison, films deposited by laser-assisted spray technique show a distribution of well-defined particles with an average size of about 80nm.[54]

2.4. Structural Characterization of Nanoparticles

The primary tool used for the structural analysis of nanoparticles is the Transmission Electron Microscope (TEM). Both high resolution (~1 nm) and low resolution (~10 nm) TEM have been used to study the nanoparticles smaller than 10nm. In addition X- ray diffraction (XRD) of coatings also provides evidence of crystallinity in coatings of nanoparticles. Unlike bulk materials, the diffraction peaks of nanomaterials tend to be much broader. Fig. 2.3 is a TEM image, which shows the crystalline planes of a nanocrystalline particle.

2.4.1. Analysis by Transmission Electron Microscope

TEM is used to study nanoparticles, which synthesis in this project. High resolution TEM enables near atomic resolution and thus allows the observation of atomic planes in single crystalline nanoparticles. In order to obtain the best result in TEM, the thickness of the film needs to be comparable with the mean free path of the electrons. Much thinner films exhibit too little scattering to provide better images, and in thick films multiple scattering events dominate, making the images blurred and difficult to interpret. Therefore, it is very important to maintain a thickness of the sample less than 100nm when preparing samples for TEM studies

.

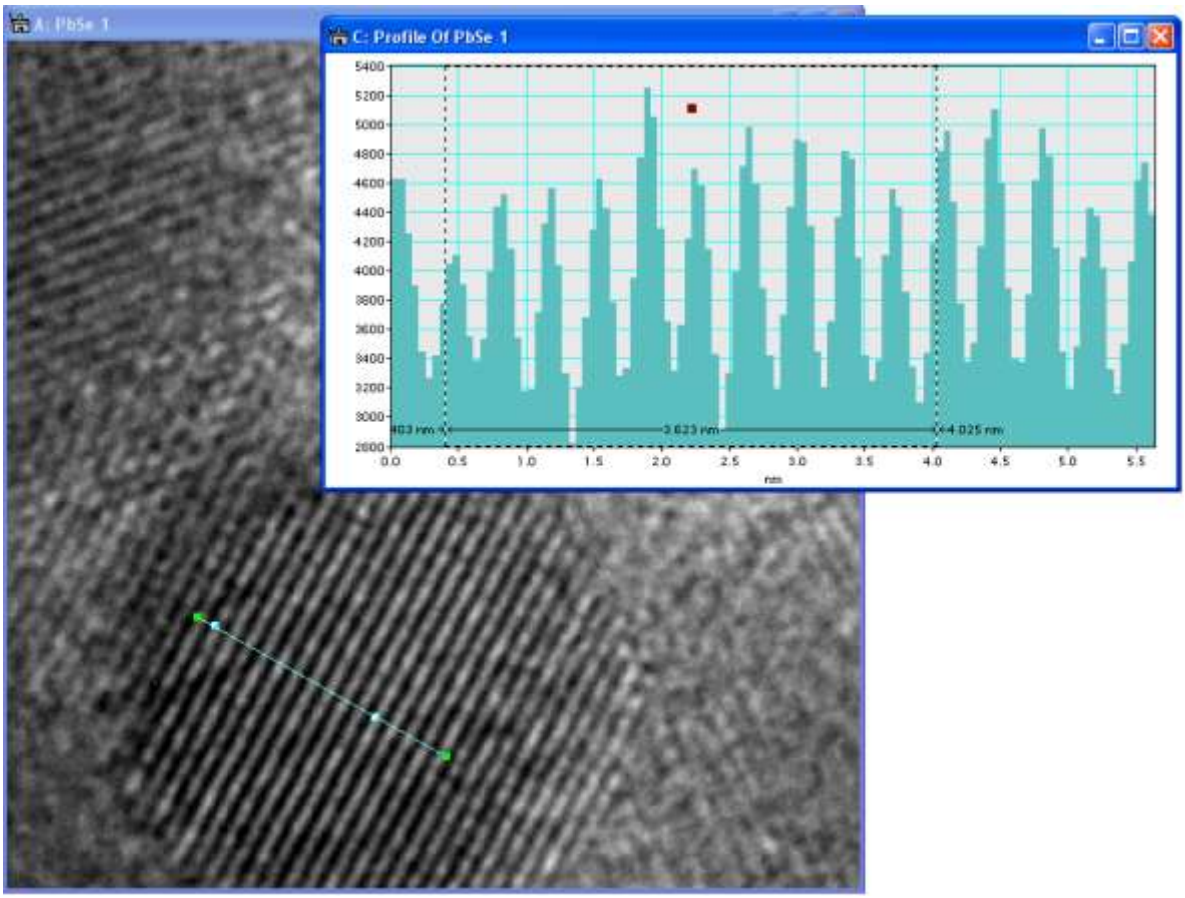

Fig 2.3: TEM image of PbSe quantum dot, which was produced by sol-gel technique. The image shows the spacing d for 200 planes.

2.5. Optical Characterization of Nanoparticles

As the semiconductor particle radius approaches the value of exciton Bohr radius, there are interesting new effects manifest due to quantum confinement. The most striking property of semiconductor nanoparticles is the pronounced changes in their optical properties, indicating a change in the band structure compared to that of the bulk semiconductor material.

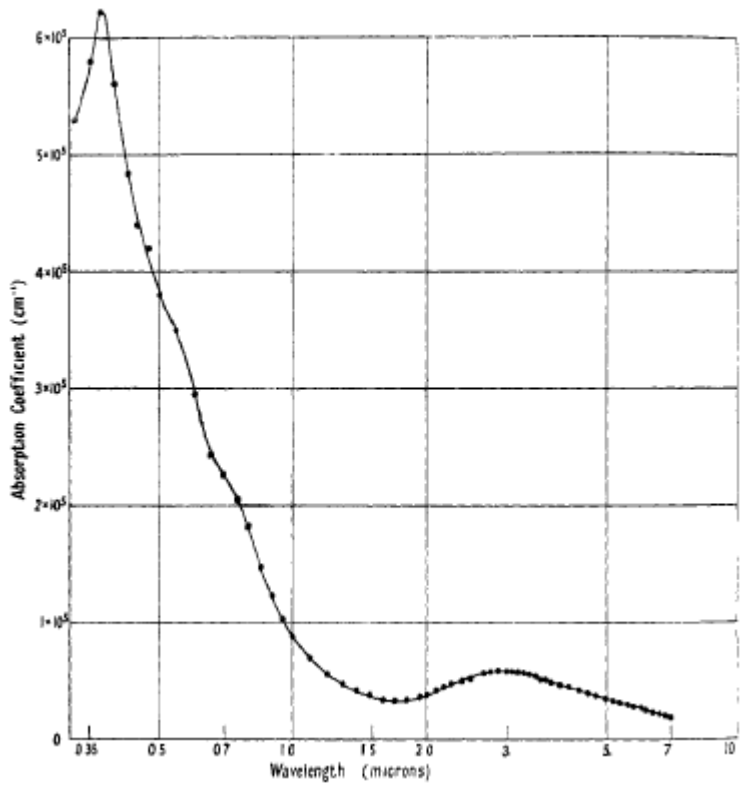

Fig.2.4: Absorption spectra of chemically deposited lead selenide. (Taken from A. F. Gibson, "*The absorption spectra of solid lead sulfide, selenide, telluride*" 1950.

In bulk semiconductor material, as explained in Section 1.1, Chapter 1, absorption of a photon by an electron in valance band undergoes a transition to the conduction band. This can be observed in optical absorbance spectra for bulk semiconductor materials. For example Fig 2.4 shows the optical absorption spectra of a chemically deposited Lead Selenide (PbSe) film on a glass substrate. The onset of absorption corresponds to the band gap of PbSe (0.26eV).

There are two interesting changes that can be seen in absorption spectra as the size of the nanoparticle becomes smaller than or comparable to the orbital radius of the electron-hole pair. First, the energy levels become quantized according to equation 4 given in section 1.2. Light- induced transition between these energy levels produced a

series of optical absorptions that can be labeled by the principal quantum numbers of the excitonic levels. Secondly, the absorption spectrum is shifted due to the confinement of the electron movement within the exciton Bohr radius. [34] This can be clearly seen in Fig 1.9, change in optical absorption spectra of a PbSe nanoparticle with change in particle size.

One can see that lowest energy absorption region, referred to as the absorption edge, is shifting to higher energy with decreasing size of the particle. Since the absorption edge is due to the band gap, this means that the band gap increases as decreases the size of the particle. Notice also that the intensity of the absorption decreases as the particle size decreases due to reduced absorption cross section.

2.5.1. Photoluminescence

Photoluminescence spectroscopy is a contactless, nondestructive method of probing the electronic structure of the material. [34] Photo-excitation of a sample causes electrons within the material to move into permissible excited states. When these electrons return to their equilibrium states, the excess energy is released and may include the emission of light (a radiative process) or may not (a nonradiative process). The energy of the emitted light (photoluminescence) relates to the difference in energy levels between the two electron states involved in the transition between the excited state and the equilibrium state. The intensity of the emitted light is related to the relative contribution of the radiative process.

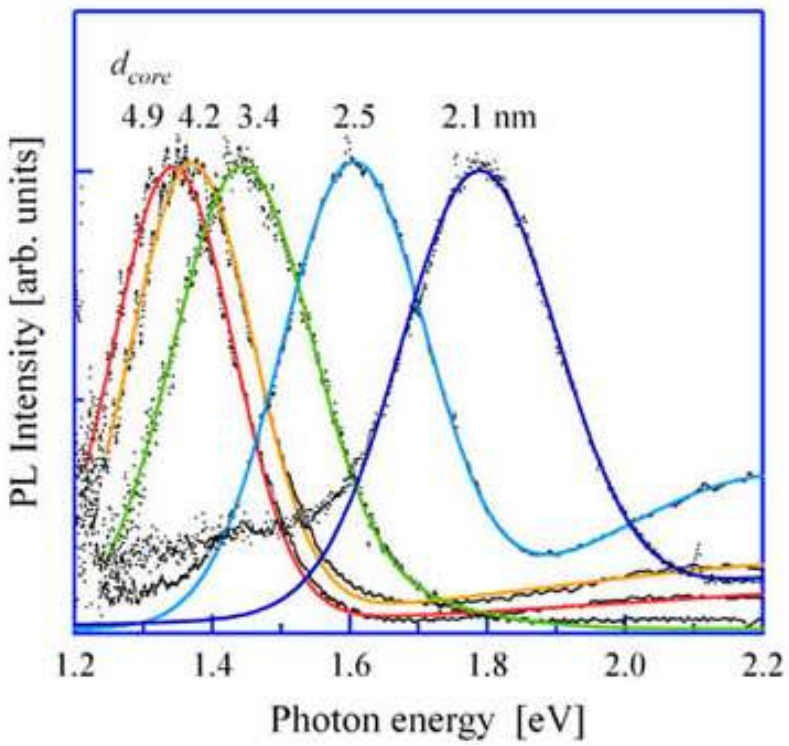

Fig. 2.5: Photoluminescence spectra from various size Si nanoparticles.
The image is taken from "unit.aist.go.jp/.../lanproc/en/contents.html".

The photoluminescence technique involves scanning the frequency of the excitation signal, and recording the emission due to recombination within a very narrow spectral range. Since this process is ultra fast (of the order of 10 nanoseconds) short pulse (< nanosecond FWHM) laser is needed to excite the electron into the higher levels.

Fig. 2.5 shows the photoluminescence spectra of various size silicon nanoparticle samples. As shown in figure 2.5, since most common transition in semiconductors is between states in the conduction and valence bands, the bandgap of the material can be easily determined by using this technique. Since radiative transition also occurs from the defect levels of the semiconductor, the photoluminescence energy associated with these

levels can be used to identify specific defects, and the amount of photoluminescence can be used to determine their concentration. This study can be further extended to determine the quality of the material by quantifying the amount of radiative recombination. [35]

Measurement Principle

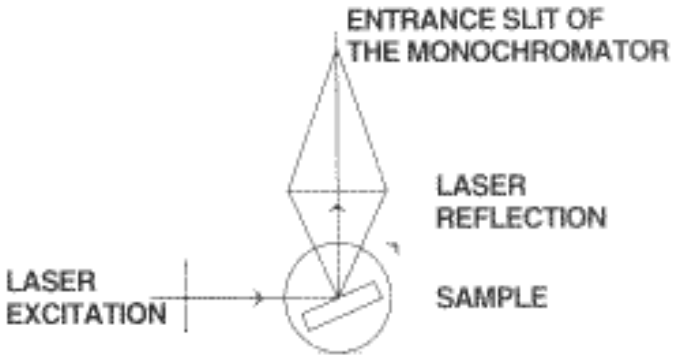

Fig.2.6: Schematic diagram of the Photoluminesence set-up

An Argon pulse laser (λ=1090nm) beam is focused on the sample which is located in the center of the sample compartment. If the energy of photons coming from the laser source is greater than the energy gap of the semiconductor, the sample emits photons. These are collected and analyzed with a dual flat field spectrograph. This system allows investigation of bandgap energies from 0.75 to 2.4 eV.

CHAPTER 3

EXPERIMENTAL PROCEDURE

3.1. Synthesis of Surfactant free PbSe Nanocrystalline Films

Synthesis of PbSe nanocrystalline films involves two steps. (1) Preparation of PbSe nanocrystals in a colloidal precursor using chemical synthesis. (2) Laser Assisted Spray deposition of surfactant free PbSe nanocrystalline films using the colloidal precursor prepared in step (1).

3.1.1. Preparation of PbSe Colloidal Precursor

Chemicals used for PbSe nanoparticle growth:
Lead Oxide (99.99%), Oleic Acid (90%), Selenium (99.5%), Trioctylphosphine (90%), 1-Octadecene (90%), Tertrachloroethylene (99%), Chloroform, Methanol, Hexane and Toluene. [53]

PbSe semiconductor nanocrystals were synthesized in a three-neck flask equipped with an electro-thermal magnetic stirrer, condenser and a thermocouple. The procedure included the preparation of two separate solutions and subsequent mixing under controlled conditions. Solution (1) was prepared by mixing 0.64g of selenium powder in

5.76g of trioctylphosphine solution at 100-150^{o}C under inert gas (argon), and stirring until the selenium powder was completely dissolved. Solution (2) was prepared by mixing 0.892g of Lead Oxide, 2.825g of Oleic acid in 12.283g of 1-Octadecene (ODE) solution at 150^{o}C under inert gas. The mixture was further heated to 180 ^{o}C where it became colorless. When the temperature was at 180 ^{o}C, solution (1) was quickly injected into solution (2). The solution immediately changed color from colorless to dark brown. The reaction mixture was allowed to cool down to 150 ^{o}C for growth of the PbSe semiconductor nano-crystals. The nanocrystals continue to grow until the solution is diluted with Chloroform. The time between injecting the solution (2) and adding Chloroform to the mixture determine the size of the PbSe nanocrystal in the solution. For our experiment, we recovered solution after 20s, 60s and 120s and added equal volume of room temperature chloroform into each solution to stop the reaction. The chloroform solution was extracted twice with equal volume of methanol. Addition of acetone caused the precipitation of the PbSe nanocrystals. The precipitated PbSe nanocrystals

Fig.3.1: Setup for synthesis PbSe NC colloidal solutions. Taken from *C. B. Murray et al.*[53])

were redispersed in hexane again by excess methanol. Then the solution was centrifuged at 3500 RPM for about 2 mins to precipitate remaining PbSe nanoparticles. The clear solution was removed from the bottle and hexane was added to redissolve the PbSe nanocrystals. These steps were repeated three times to remove all the excess surfactant from the PbSe nanocrystals.[53]

3.1.2. Laser Assisted Spray (LAS) Deposition of PbSe Quantum Dots

The PbSe nanoparticle (10nm) immersed in hexane was used as a precursor in the Laser-Assisted Spray deposition. The aerosols of the precursor with an average drop size of 1.5 μm were generated by an ultrasonic nebulizer (Model 241T) which operated at a frequency of 2.4 MHz. Each aerosol drop contained ≈ 10^6 of PbSe nanoparticles. The aerosol was carried through a conical nozzle into the growth chamber by the SF_6 gas at a flow rate of 0.68slpm. The schematic diagram of the laser-assisted spray system is shown in Fig.3.2. The droplets and the SF_6 gas interact with a focused continuous wave

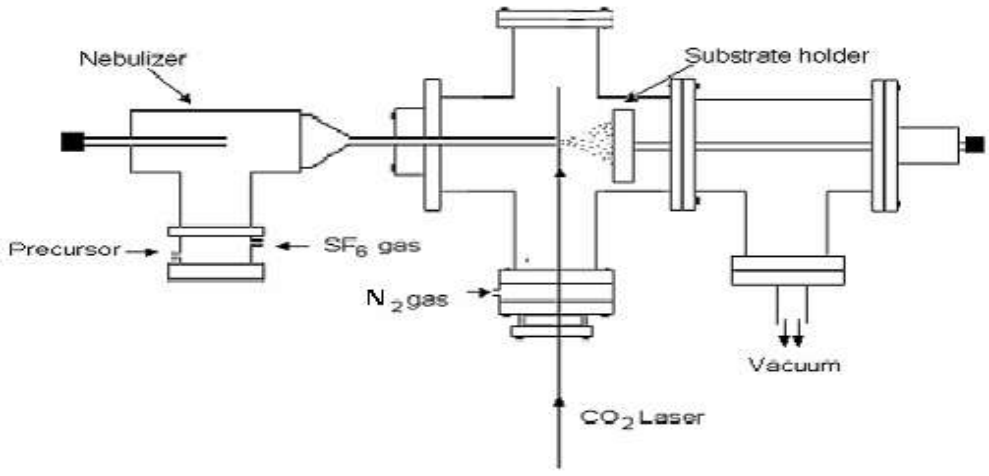

Fig.3.2: Schematic diagram of the laser-assisted spray film growth system.

(CW) CO_2 laser beam at the nozzle. The CO_2 laser radiation at a wavelength of 10.6μm is strongly absorbed by the SF_6 gas through vibrational excitation. The laser power of 14W used in the experiment was sufficient to increase the temperature of the gas and subsequently the droplets to about 300^oC. The temperature of the flow just after the laser interaction was measured by using a thermocouple. The graph in Fig.3.3 shows the variation of temperature with the flow rate. The nitrogen gas was introduced to the growth chamber to maintain the pressure at about 650Torr. The substrates were placed 4cm away from the nozzle to obtain a uniform coating.

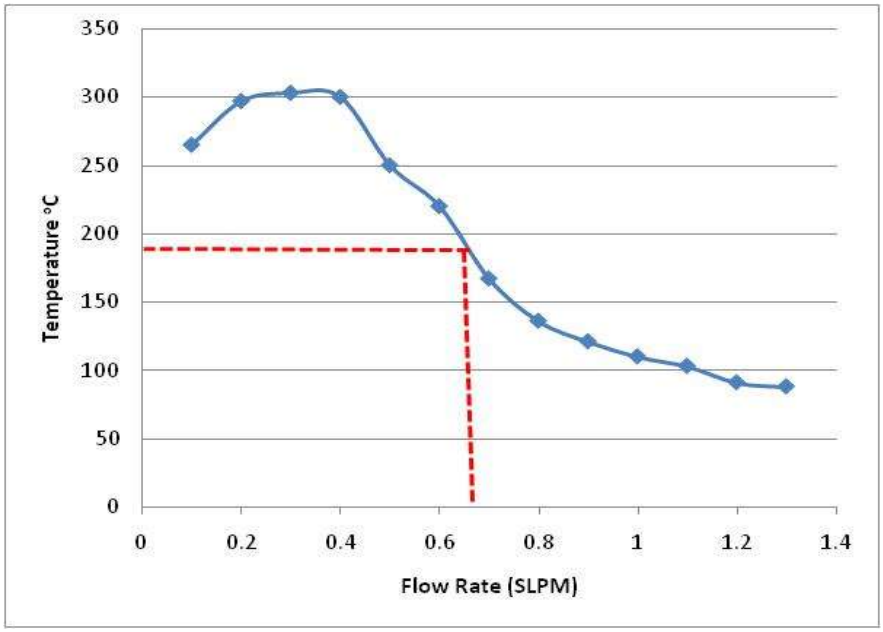

Fig.3.3: The graph of temperature of the gas flow vs flow rate of SF_6 gas. The line shows the optimum flow rate of the system.

3.2. Sample Preparation for TEM Studies

PbSe nanoparticles that are heated by the laser were deposited on carbon coated TEM grids for about a minute to form a PbSe quantum dot monolayer on the grid. Films

were deposited under different flow rates to obtain different plume temperatures according to the graph in Fig 3.3.

3.3. Sample Preparation for Conductivity Measurements

One of the expected outcomes of the LAS process is the formation of QD films without the surfactant barrier between adjacent particles. The close contact between particles is expected to enhance the conductivity of QD films. Nanoparticle coatings with and without the laser heating were deposited on glass substrates under similar growth conditions. Substrates were pre-patterned with gold-titanium pads to produce gaps with spacing of 2μm, 5μm, 10μm and 20μm for conductivity measurements

There are several techniques available for fabricating Au/Ti electrodes on glass substrate. The aim is to produce precise patterning of the electrodes with well-defined gap sizes. The photolithography lift-off technique followed by a thermal evaporation method was used to fabricate the Au/Ti electrodes. First, well cleaned glass substrates were spin-coated by a photo-resist and a pattern to generate two electrodes of 50 μm width. Inter-electrode spacing of 2, 5, 10, and 20 μm were etched away by the photolithographic lift-off technique. Then a 20nm Ti adhesive layer followed by a 200nm Au layer was deposited using thermal evaporation. Finally the remaining photo-resist was removed to expose the Ti/Au electrodes as shown in Fig. 3.4.

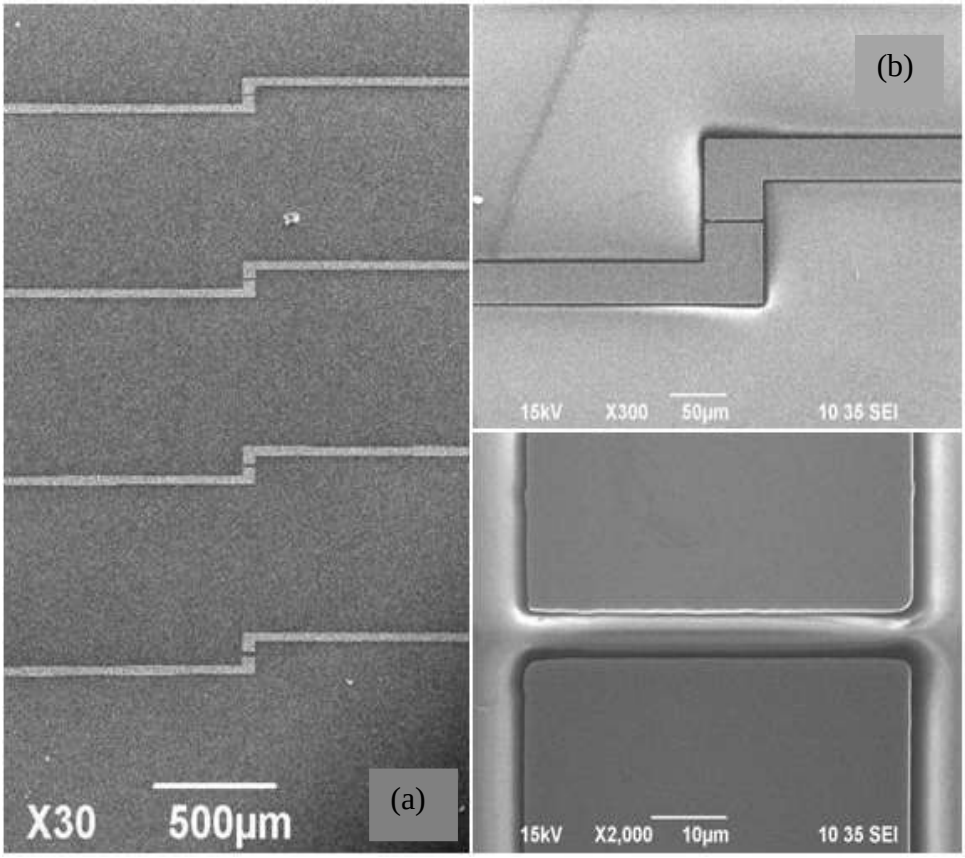

Fig.3.4: SEM images of Au/Ti electrodes fabricated for conductivity measurements. (a) Electrodes with 2µm, 5µm, 10µm and 20µm gap sizes. (b) and (c) Zoom in image of 5µm gap.

3.2.2. Deposition of PbSe QD layer on Electrodes

The deposition of surfactant free PbSe layer for conductivity measurement was performed according to the procedure discussed in following section with an additional step of shadow masking the substrate. A shadow mask provided a well defined area for deposition over the gap. The shadow mask was set up on the substrate in the following manner. During the masking, thin spacers were placed between the substrate and shadow-masked to protect the electrodes from scratching.

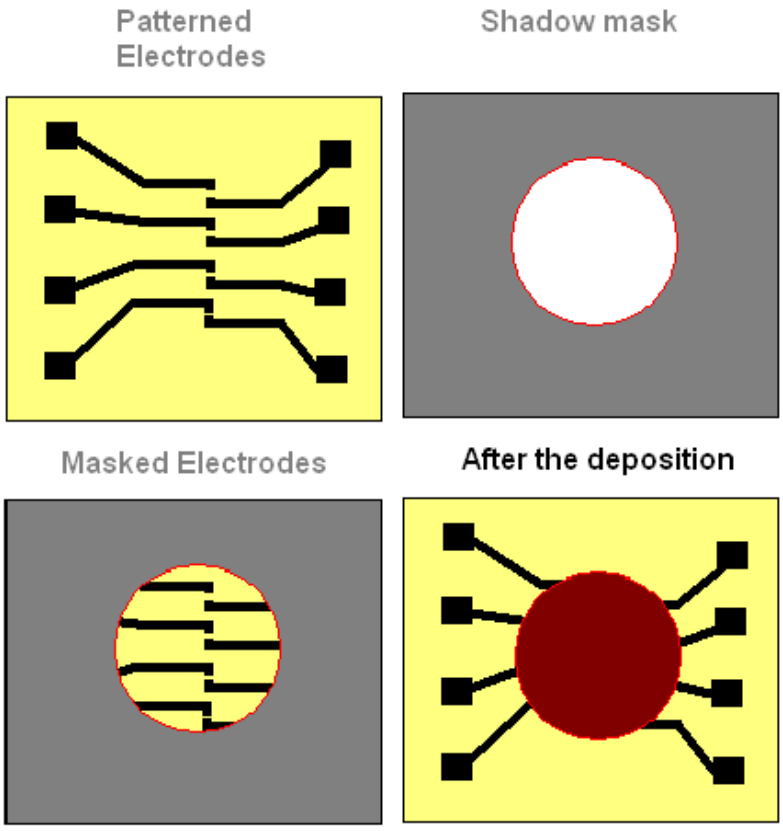

Fig.3.5: Method of using a Shadow mask for QDs deposition

Prior to the deposition, the patterned glass substrates were cleaned thoroughly with ultrasonic agitator to remove all organic surface contamination. The PbSe QD layer was deposited on electrodes by using LAS for two conditions (with and without laser) and the conductivity was measured. The deposition was carried out for about 30mins to obtain a thickness of about 200nm. The thickness and the morphology of the deposited layer were measured by a Mechanical Profilometer and the Scanning Electron Microscope (SEM).

3.4. Synthesis of the P3HT Polymer Coating

Typically, polymer coatings are formed by spin-coating a substrate with a solution containing the polymer. Subsequent heating evaporates the solvent to form a dense polymer film.[36] In order to enable co-deposition of QDs and the polymer, the possibility of using the LAS process for the fabrication of the polymer film was investigated. The precursor, which contained 5mg/ml Poly(3-hexylthiophene-2,5-diyl) (P3HT)+Toluene was prepared by heating the mixture for 2hrs in Nitrogen environment. (The chemicals were purchased from Sigma-Aldrich). Since the polymer can decompose due to high temperature of the Laser, during the polymer deposition, the process was run without turning the laser. The substrate was heated below glass transition temperature of the polymer ($<150^{o}$ C). Prior to the deposition, the system was flushed with Nitrogen for 5 mins to remove all the oxygen from the system. The pressure of the chamber was set to 650T in order to maintain a pressure difference for adiabatic expansion though the nozzle. The process was run for about 30min to deposit a 400nm layer on the heated glass substrate. Several sets of samples were obtained by changing the substrate temperature and the thickness of the films. After the deposition, the samples were cooled down in the chamber with constant nitrogen flow and then carefully transferred for optical measurement with minimum exposure to the atmosphere.

The crystallinity of the deposited films was investigated by an X-ray Diffraction technique at very low angles, since the highest peak for crystalline P3HT was reported at $2\Theta \approx 5.1^{o}$ (degree). The morphology of the films was studied by AFM using "Noncontact

mode". The Noncontact mode was used because of the softness of the films. The results for these studies are shown and discussed in chapter 4 under section 4.2.

3.5. Co-Deposition of QD/Polymer Composite Films

In the formation of QD/polymer composite coatings for applications in solar devices, the uniform distribution of QDs within the polymer is crucial for optimum performance. The conventional practice is the mixing of the QDs and the polymer in a common solvent and spin-coating the mixture on a substrate followed by thermal treatment to evaporate the solvent.[37] There are two drawbacks in this method; (1) the QDs will have a surfactant barrier between the particle and the polymer surrounding it, which adversely affected charge transport, (2) obtaining a uniform distribution of particles within the polymer matrix is not possible through spin-coating and leads to pockets of agglomerated QDs. The LAS process enables co-deposition of QDs and polymer, and thus provides a way to deposit the composite structures with uniform coverage. The co-deposition system comprised two spray nozzles to transport aerosols of two different precursors, one containing the QDs and the other containing the polymer. The schematic diagram of the modified system is shown in Fig 3.6.

As shown in Fig 3.6, the two nozzles are attached to the two nebulizers and therefore can be controlled independently to spray two different materials. In the case of PbSe QDs/Polymer deposition, one nozzle carries the aerosol of PbSe quantum dots/hexane precursor while the other nozzle carries the aerosol of P3HT polymer precursor. The CW CO_2 laser is focused on to the nozzle that carries the PbSe QDs to

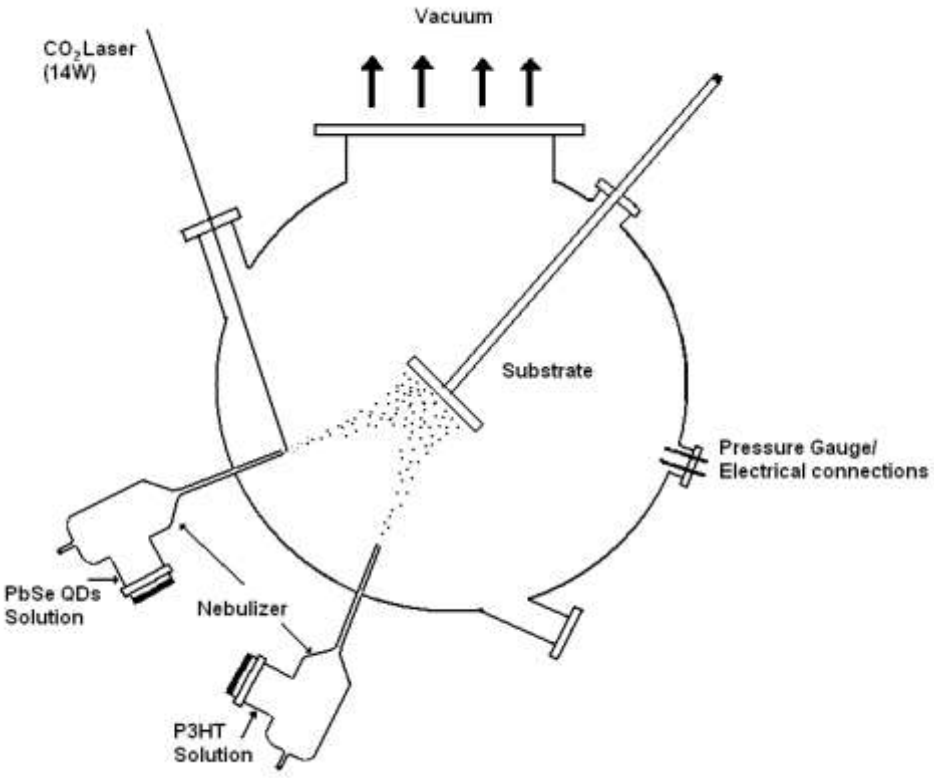

Fig. 3.6: Schematic diagram of Laser Assisted Co-deposition system

burn the surfactant during the deposition. The P3HT polymer droplets are deposited on the substrate without any laser interaction. Polymer aerosols were not laser-heated to prevent solidification prior to arriving at the substrate. During the deposition, both P3HT polymer and surfactant free QDs are combined at the substrate to form a hybrid structure. The gas flow rate through the nebulizer controls the growth rate of each species at the substrate. This co-deposition technique provides clean surface contacts between the QDs and the polymer for the PbSe QDs to transfer generated excitons to the P3HT polymer during the dissociation process.

The precursor containing the PbSe QDs was made by dispersing PbSe QDs in hexane as discussed in section 3.1.1 and P3HT solution was made by mixing P3HT

powder with Toluene as discussed in section 3.4. The substrate was heated below glass transition temperature of the polymer. Prior to the deposition, the system was flushed with Nitrogen for 5mins to remove all the oxygen from the system. The flow rate of 0.68slpm of SF_6 and 0.68slpm of Nitrogen were maintained respectively through PbSe and P3HT nebulizers to carry the aerosol to the nozzles. The pressure of the chamber was set to 650T in order to maintain a pressure difference for adiabatic expansion though the nozzle. A 400 nm film was deposited within about 30 min. Several sets of samples were obtained with different film thicknesses. After the deposition, the samples were cooled down in the chamber with constant nitrogen flow and then carefully transferred for optical measurement with minimum oxygen contamination. The crystallinity of the deposited films was investigated by X-ray diffraction technique. Initial stage of growth was studied by depositing a thin coating of the composite on TEM grids.

3.6. Fabrication of PbSe QDs/P3HT Solar Cell Structures

Typical structure of a QDs/Polymer Solar cell consists of an ITO coated glass substrate as the bottom electrode, spin coated transparent layer of *polyethyl-enedioxythiophene* (PEDOT), spin coated layer of QD/Polymer(P3HT) blend and a thermally evaporated aluminum film as the top electrode. [37] In this device structure photons in the visible and infrared region of the solar spectrum are absorbed by the polymer P3HT and the PbSe QDs to generate electron-hole pairs. PbSe will accept electron and transport them to the Al electrode through the PbSe nanocrystal network, while P3HT will accept holes and transport them through PEDOT to the ITO electrode.

PEDOT layer in the structure will minimize the hole extraction barrier at the anode surface.

Therefore, the fabrication of a solar cell device starts by solution casting of PEDOT on the ITO glass substrate followed by a 30min annealing at 200^{o}C in N_2 gas flow to create an 80nm thick hole transport layer. Then the solutions of PbSe QDs and P3HT dissolved in Toluene were sprayed on to the heated PEDOT layer at 150^{o}C by using Laser Assisted Co-Deposition under N_2 environment. The thickness of the composite layer was maintained at about 500nm to form the active region of the photovoltaic device. Then the sample was further heated in N_2 gas inside the chamber at about 150^{o}C for 10mins in order to fully remove the solvent and to crystallize the P3HT in the composite film. Finally, an aluminum electrode was thermally evaporated through a shadow mask onto the film. A simplified structural layout of the PbSe QDs-P3HT solar device is shown in Fig. 3.7.

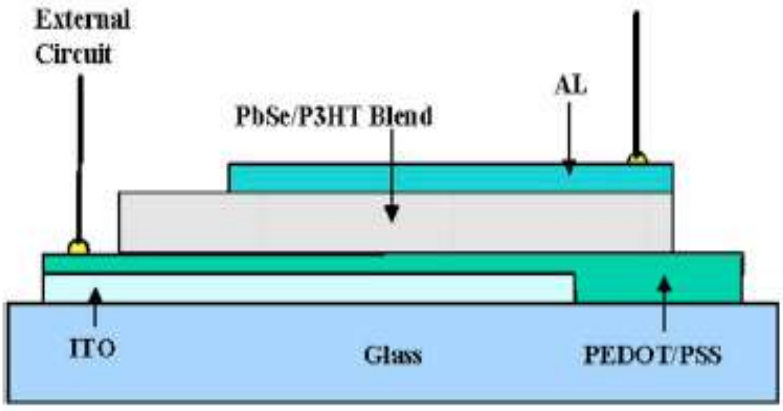

Fig. 3.7: Schematic layout of the PbSe-P3HT based hybrid solar cell structure.

CHAPTER 4

EXPERIMENTAL RESULTS

4.1. Characteristics of Self-Assembled PbSe nanoparticles

The distribution of PbSe nanoparticles prepared by the solvothermal technique that is outlined in Chapter 3 is shown in the low-resolution TEM images (Fig. 4.1). Figs. 4.1 (a), 4.1 (b) and 4.1 (c) correspond to particle growth times of 20, 60 and 180 seconds, respectively. The samples were prepared by drop-casting the final solution onto carbon coated TEM grids purchased form Electron Microscopy Sciences. Gradual increase of the average particle size from 8nm to 12nm with increasing reaction time can be observed.

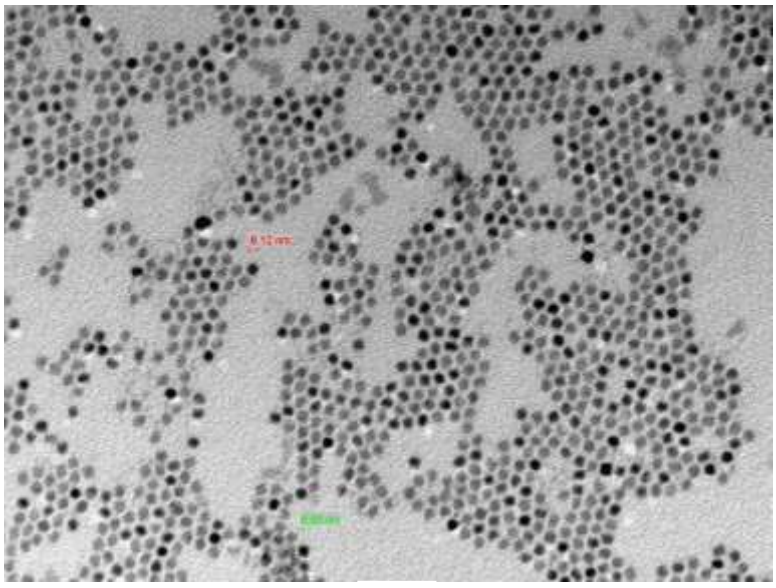

(a)

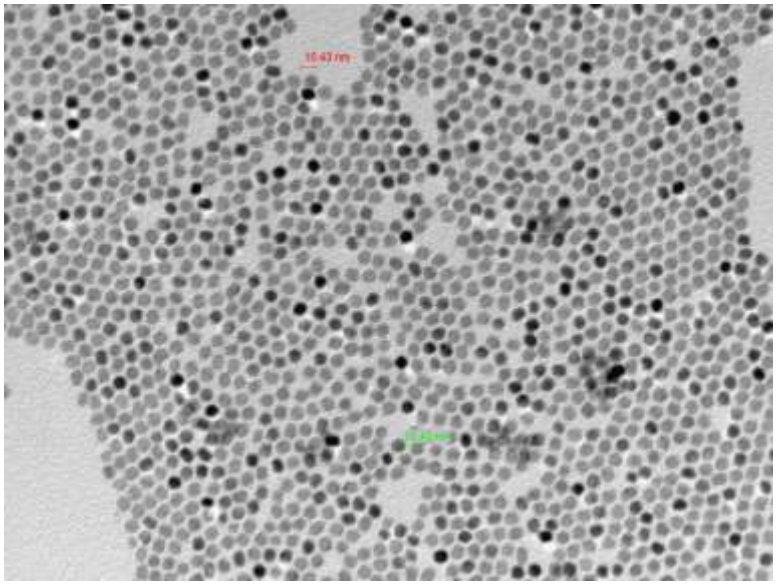

(b)

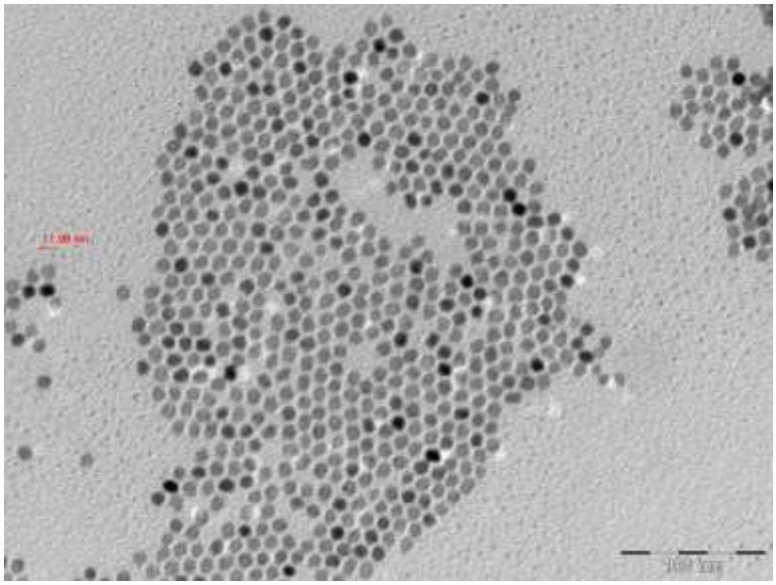

(c)

Fig. 4.1: PbSe particles separated from the solution after (a) 20s (b) 60s (c) 120s.

These low-resolution TEM images also show that the PbSe NCs are packed in a simple hexagonal mono-layer with the long organic ligands filling the interstices between NCs. When the temperature of the mixture (solution 1 and 2) was at 180^{o}C, the PbSe

particles started to nucleate. Lowering the reaction temperature immediately after injection terminated the formation of new nuclei. Low temperature permits the nuclei to grow continuously until the growth is stopped by adding chloroform. Therefore, larger particle sizes can be obtained at 120s compared to 20s. The images provide clear evidence of particle size variation over the course of reaction between lead oxide and selenium trioctylphosphine. These images also show the particle size distribution to be relatively narrow. For particles of average diameter of 10 nm, the standard deviation was about 10-15%. High resolution TEM micrographs of these PbSe nanocrystals show the single crystal nature of the nanoparticles (Fig. 4.2).

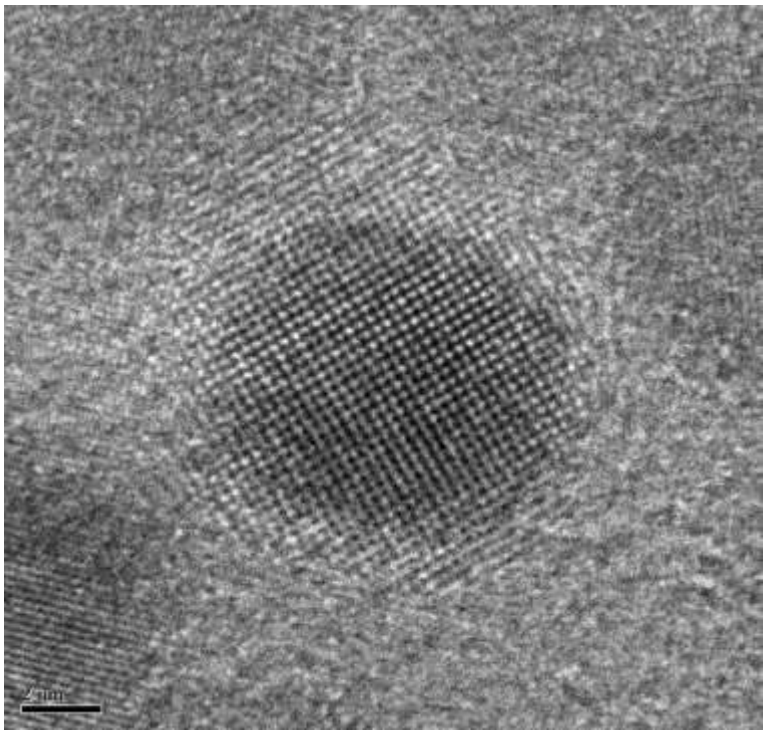

Fig. 4.2: High-resolution TEM image of individual PbSe semiconductor nanocrystal. The singal-crystal structure is clearly apparent.

In addition, electron diffraction from the nanoparticles showed circular patterns corresponding to the crystal planes of PbSe (Fig. 4.3). Since the diffraction image results from a collection of randomly distributed single crystal nanoparticles, the patterns resemble that of a polycrystalline sample. However, the bright spots on the circles correspond to single crystal diffraction from each particle.

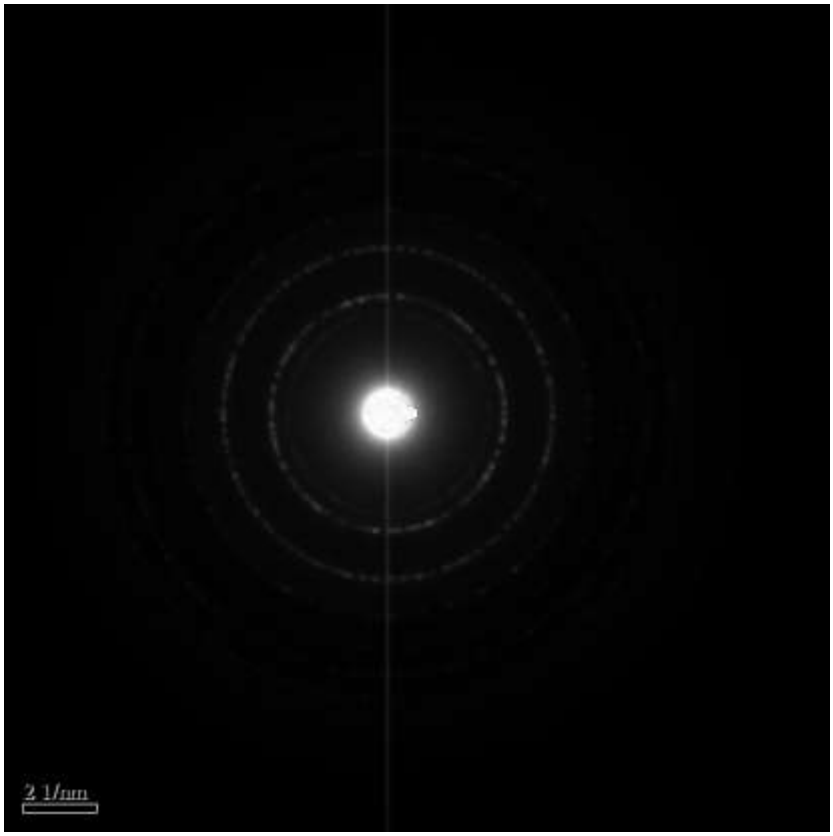

Fig. 4.3: Electron diffractogram of the PbSe nanocrystals

X-ray diffraction was performed by using a Bruker AXS D8 X-Ray diffractometer on samples made by three different nanoparticle size distributions. Samples for XRD were prepared by forming multiple layers with multiple drop-casting steps.

The XRD patterns of PbSe nanoparticle coatings prepared by drop-casting show all possible peaks for PbSe crystals within the observed range of angles. Since all "*h,k,l*" values were all even or all odd, one can confirm that the PbSe nanocrystals have a perfect rock-salt (FCC-Fm-3m) structure.

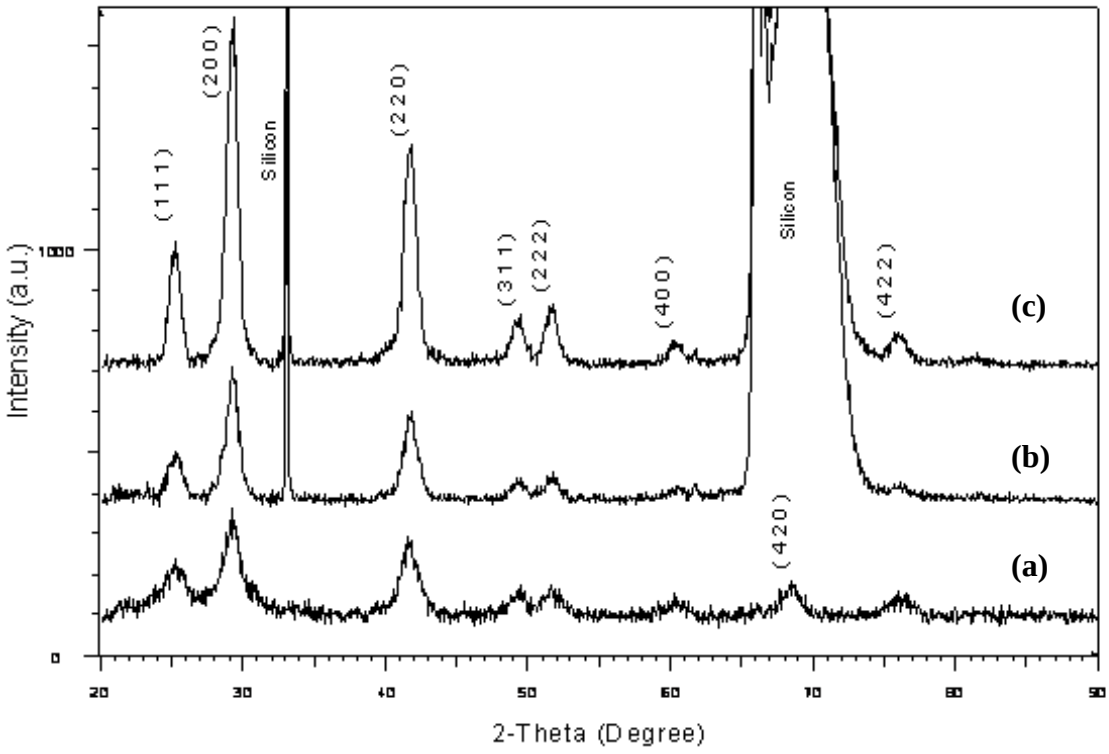

Fig. 4.4: X-ray diffraction pattern of the samples made by three different particle distributions (a) 8-9nm (b) 9-10nm (c) 10-12nm.

Also from X-ray diffraction pattern one can determine the "lattice parameter" of PbSe nanocrystals. It can be calculated by using following equation.

$$a = \frac{\lambda\sqrt{h^2 + k^2 + l^2}}{2\sin(\Theta)} \qquad 4.1$$

Where λ=1.5406 A^o and *h,k.l* are corresponding miller indices for each θ angle. Table 4.1 shows the calculated values for lattice parameter for each XRD peak.

Angle (2θ)	*h, k, l*	Lattice parameter (a) A^o
25.16	(111)	6.125
29.12	(200)	6.128
41.66	(220)	6.127
49.35	(311)	6.120
51.62	(222)	6.128
60.38	(400)	6.127
66.44	(331)	6.128
68.41	(420)	6.128
76.04	(422)	6.127
81.58	(511)	6.127

Fig. 4.5: Table of Miller indexes and Lattice parameters of PbSe nanocystals calculated from XRD peaks obtained from Fig. 4.4.

According to the table, the lattice parameter for PbSe nanocrystals was found to be 6.1265 A^o. The calculated values of lattice parameters are in excellent agreement with the cubic (rock salt) bulk PbSe lattice parameter of 6.128A^o.

4.1.1. Optical Characterization of PbSe Nanoparticles

The visible- IR absorption spectra of nanocrystalline PbSe in PCE is shown in Fig. 4.6 for different particle sizes prepared by the method outlined in Section 3.1.1.

According to Fig. 4.6, one can clearly see three absorption peaks in each absorption spectrum. The first strong absorption peak corresponds to the first inter-band transition ($1S_h$ to$1S_e$), the second absorption peak corresponds to the second inter-band

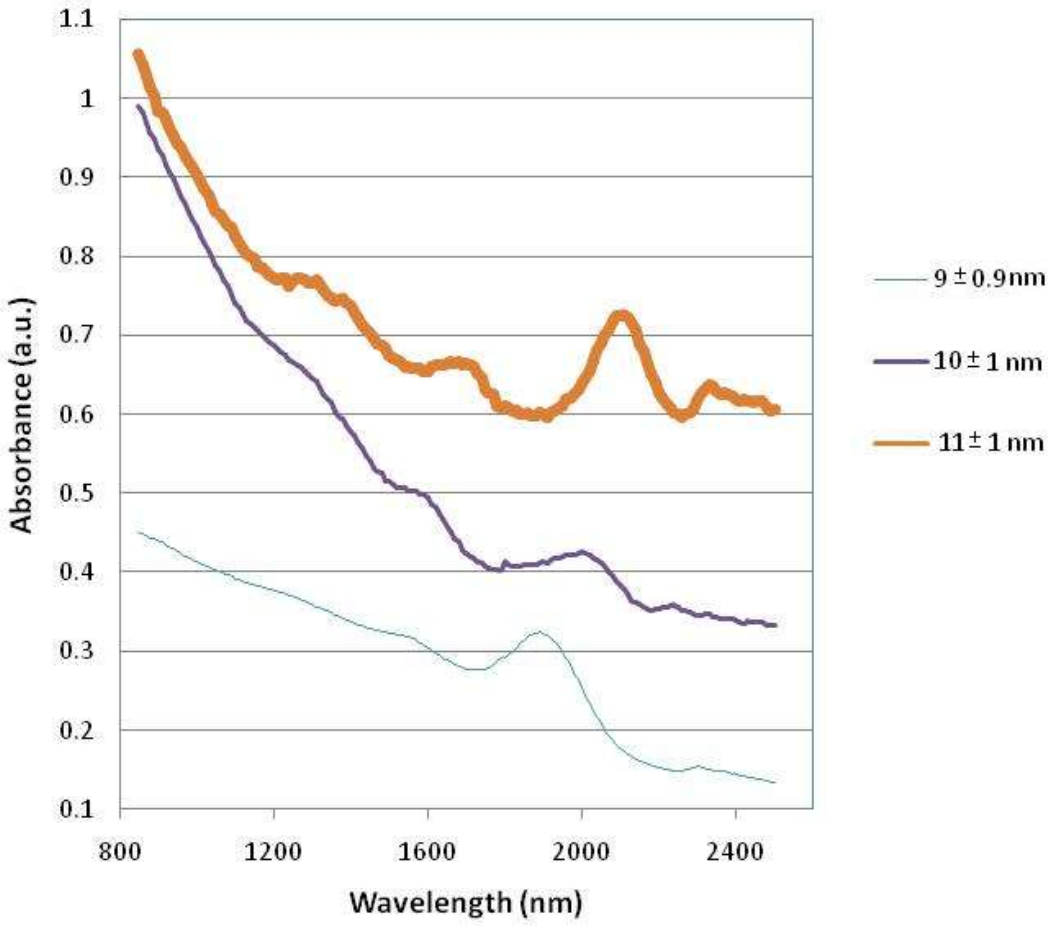

Fig. 4.6: Near-infrared absorption spectra of as-prepared PbSe semiconductor nanocrystals immersed in PCE. (In collaboration with Dr. Jiang's lab)

transitions$1S_h$ to$1P_e$ and $1P_h$ to $1S_e$, and the third broad absorption peak corresponds to the $1P_h$ to $1P_e$ transition.

These absorption peaks confirm the quantum confinement of these PbSe semiconductor nanocrystals. As the size of the semiconductor NC decreases, the absorption peaks shifted towards high energy, thus confirming the increasingly strong confinement effects. The band gap of the QDs can be computed based on the 1st absorption peak. Fig. 4.7 shows the change in bandgap of PbSe nanocrystals with nanocrystalline size that was derived from the absorption data. These values are compared with values computed from equation 4.2. The variation between the calculated and experimentally determined bandgaps (~8% for particle sizes of 9 $\pm$ 0.9 nm) may be due to the size distribution.

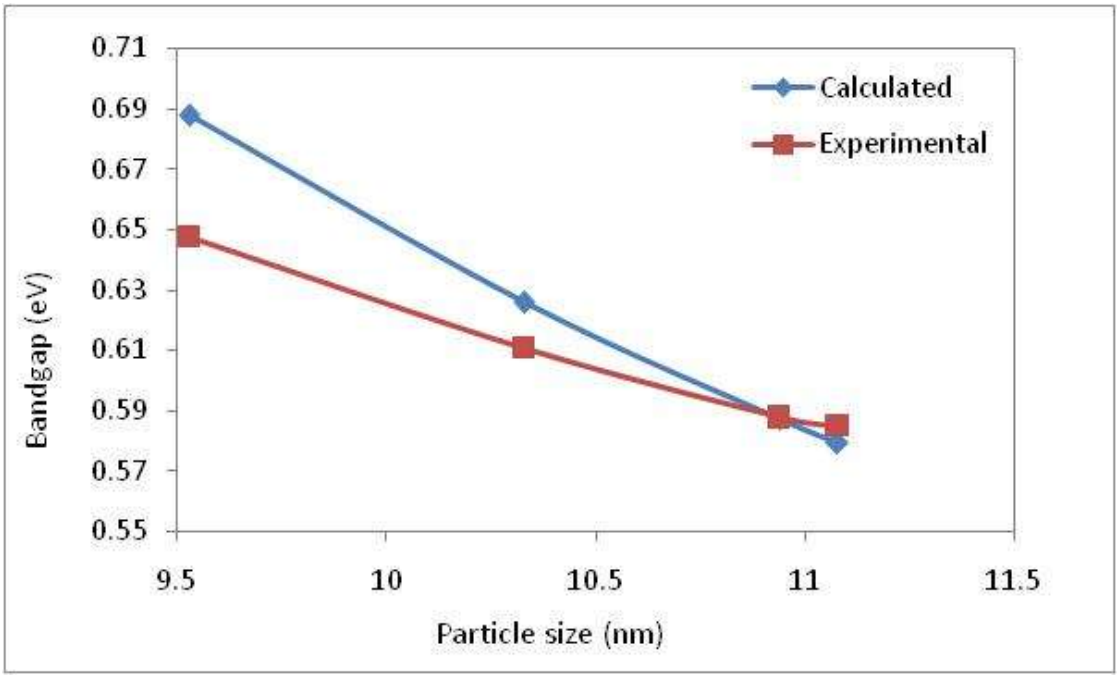

Fig. 4.7: Change in bandgap energy with particle size; (red line) is experimental, (blue line) is calculated.

$$E_{eff} = E_g + \frac{h^2}{8m_e^*}\left(\frac{1}{L_x^2}+\frac{1}{L_y^2}+\frac{1}{L_z^2}\right)+\frac{h^2}{8m_h^*}\left(\frac{1}{L_x^2}+\frac{1}{L_y^2}+\frac{1}{L_z^2}\right) \quad 4.2$$

E_g is the bandgap energy for bulk PbSe, m^*_e and m^*_h are effective masses of PbSe (for PbSe $m^*_e \approx m^*_h$) and L is the particle size (for Quantum dot $L_x = L_y = L_z$).

Photoluminescence spectroscopy was performed in order to confirm the excitation energy levels of the PbSe nanoparticles in the solution. The Photoluminescence spectra for two particle size distributions with average sizes of 11 nm and 9 nm are presented in Fig. 4.8 and Fig. 4.9, respectively.

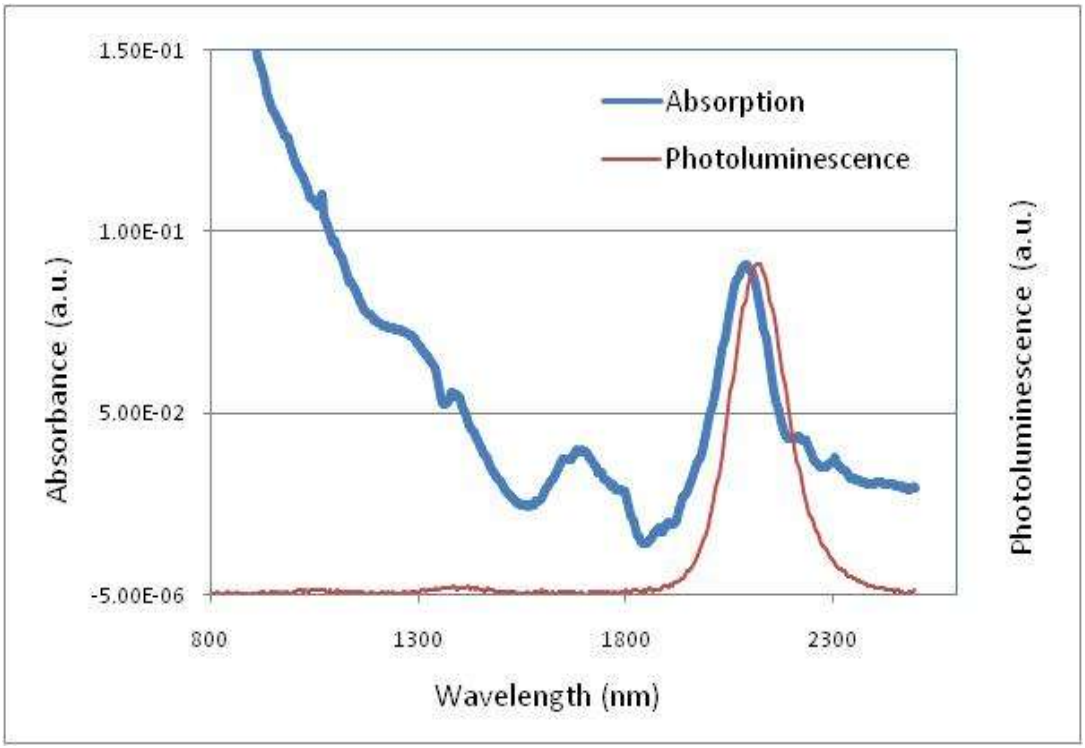

Fig. 4.8: Absorbance and Photoluminescence spectra of 11nm PbSe semiconductor nanocrystals. (In collaboration with Dr. Jiang's lab)

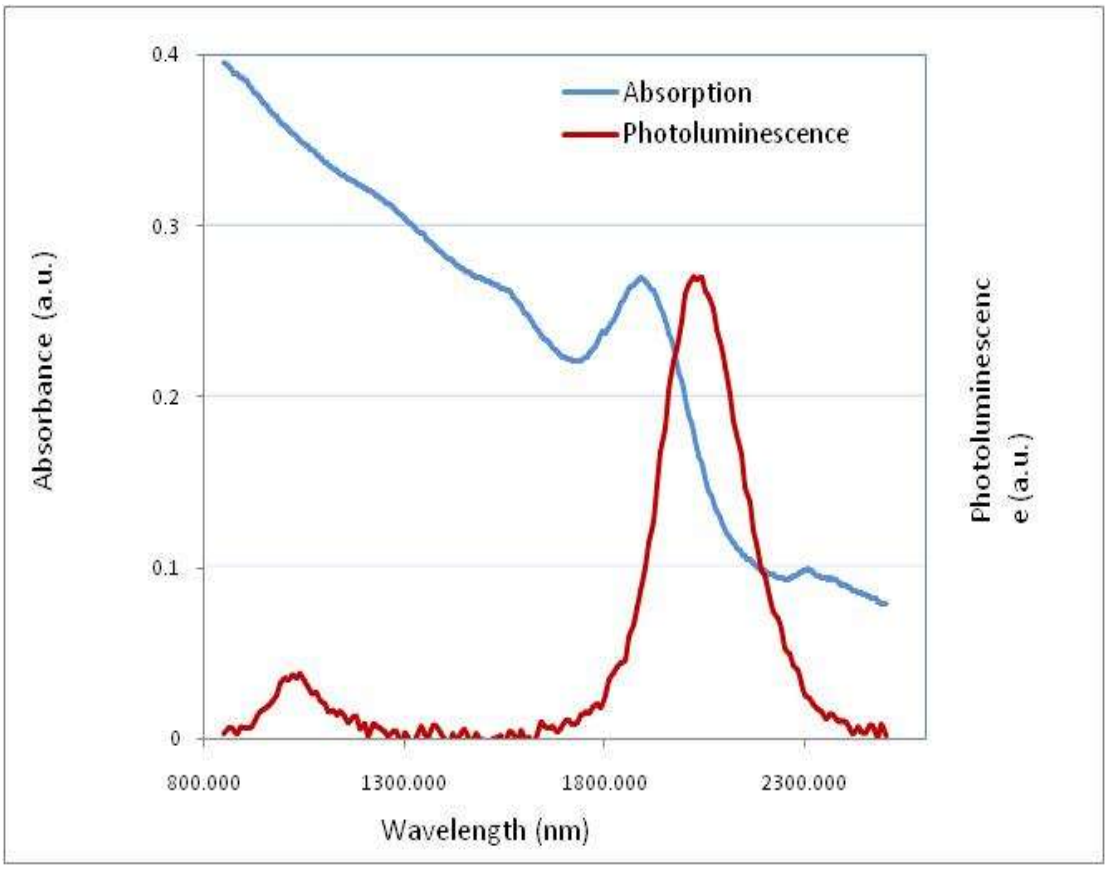

Fig. 4.9: Absorbance and Photoluminescence spectra of 9 nm PbSe semiconductor nanocrystals. (In collaboration with Dr. Jiang's lab)

Both spectra clearly show the strong near-infrared emission in as- synthesized PbSe semiconductor nanocrystals. In figure 4.9, the first absorption peak is positioned at 2105nm while the emission (Photoluminescence) peak is positioned at 2130nm. There is a 25nm Stokes shift, which is the energy difference between absorbed and emitted photon. In figure 4.9, the first absorption peak is positioned at 1905nm while the emission peak is positioned at 2040nm. There is a 135nm Stokes shift.

4.1.2. Structure, Morphology, and Optical Properties of PbSe Nanoparticle Coatings Deposited by LAS Process

After confirming the crystallinity and the quantum confinement of the PbSe semiconductor particles, they were dispersed in excess hexane for use as the precursor for Laser Assisted Spray deposition. Fig. 4.10 shows the comparison of absorption spectra between a LAS deposited coating of PbSe on a glass substrate and as-synthesized PbSe nanoparticles suspended in hexane.

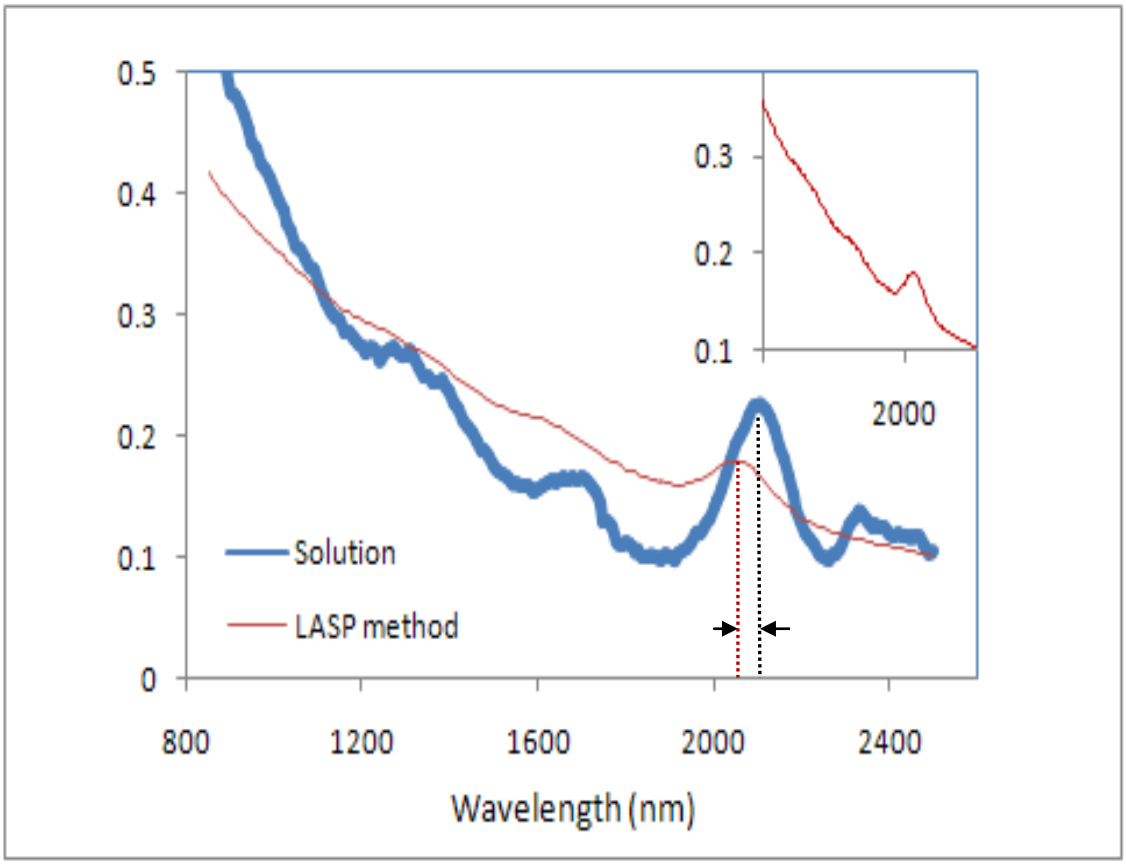

Fig. 4.10: Absorption spectra of 11 ± 1nm quantum dots in solution and after LASP deposition. There is a 29.1 Blue shift between them due to reduce QD sizes after burning the surfactant. Inside: Zoom in of LAS deposited PbSe absorption spectrum. (In collaboration with Dr. Jiang's lab)

The three peaks in the absorption spectra of the PbSe coatings clearly indicate the first inter-band transition (HOMO-LOMO transition), second inter-band transition ($1S_h$ to$1P_e$ and $1P_h$ to $1S_e$) and the third transition confirming the quantization of energy levels in the PbSe nanoparticle coating. However, the intensities are much smaller than that for the nanoparticles suspended in solution due to the much smaller absorption depth available for the particles on the film. One of the important outcomes of this result is the confirmation that the LAS process, under the growth conditions used, does not significantly alter the optical properties of the PbSe quantum dots. The only noticeable difference in optical properties is a 40.1nm blue shift in LAS deposited coating, most probably due to removal of surface layer along with the surfactant coating of the particles making the particles smaller. A similar blue shift had been reported by Edward when long oleic ligands were exchanged with short butylamine ligand, and also with completely removing the ligands from PbSe nanocrystals.[38] For further investigation of this surfactant burning effect, three samples were made on TEM grids with different plume temperatures and were characterized by Transmission Electron Microscopy (TEM).

Fig. 4.11 compares the TEM images of the samples prepared at three different plume temperatures. They are also being compared to a drop-casted film. Inter-particle separation of 2-5nm is noticeable in drop-casted films due to the presence of the surfactant (Fig. 4.11 (a)). When the laser-heated gas temperature is estimated to be 80-100 ^oC (Fig. 4.11 (b)), some of the particles become connected as their surfactants are burned off. As shown in Fig. 4.11 (c), for an estimated temperature of 150-200 ^oC, most of the particles are in close contact indicating surfactants have been removed

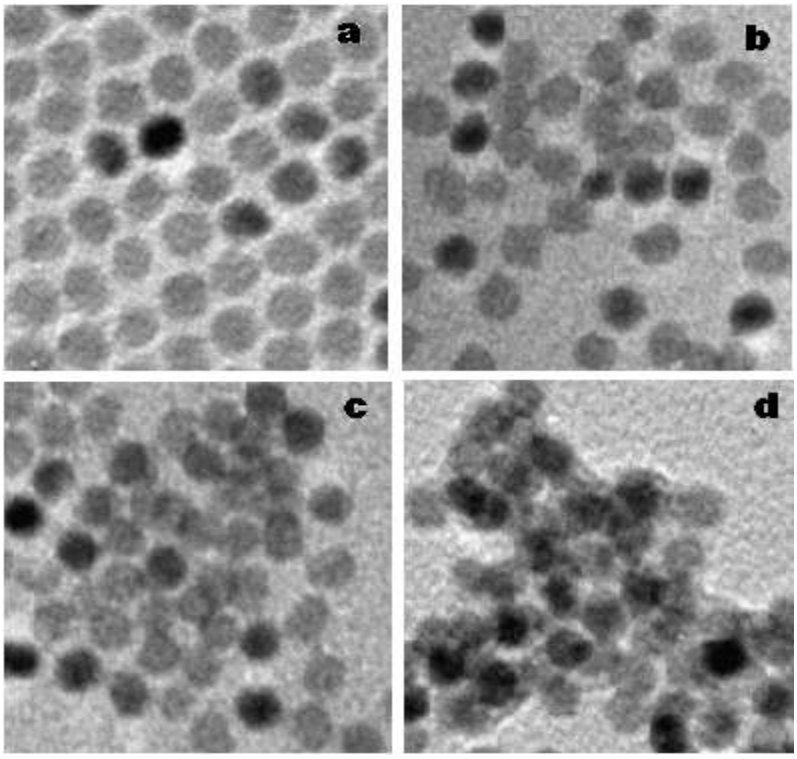

Fig. 4.11. TEM images of PbSe QDs deposited on carbon coated TEM grid for 1min with different plume temperatures. (a) drop-casted (b) 80-100^{o}C (c) 150-200^{o}C (d) 200-230^{o}C.

effectively, yet they are not coalescing into larger particles. At higher heating rates, particles appeared to coalesce together. Therefore, the optimum temperature of the laser heated gas was determined to be in the range of 150-200^{o}C. The high resolution TEM images (Fig. 4.12) clearly show the intimate contact between QDs while drop-casted film shows 2nm gaps between them. It provides clear evidence of burning the surfactant during the growth process. The same effect was also observed in vacuum annealed PbSe QDs, but at very high temperature (~ 523K) due to decomposition of ligands.[39]

Fig. 4.12: High resolution TEM images of (a) drop-casted and (b) LAS deposited PbSe NCs. LAS shows the intimate contact between the NCs while drop-casted shows a 1-2nm surfactant coating between them.

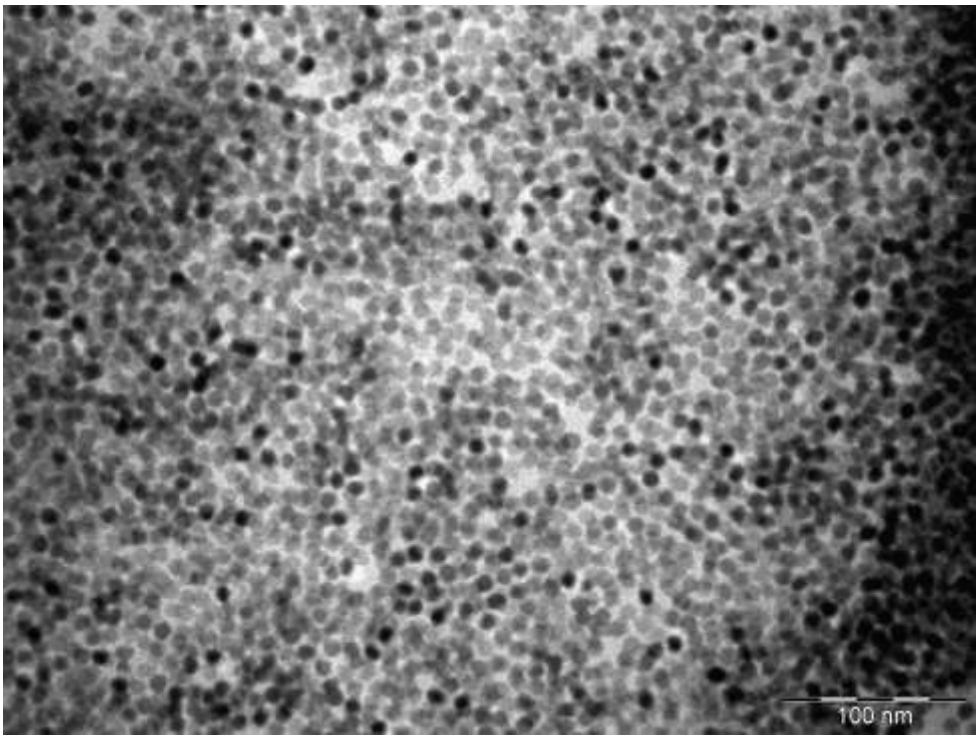

Fig. 4.13: TEM image of a coating deposited for 2mins at the optimum plume temperature 150 ^{o}C-200 ^{o}C.

Fig. 4.13 shows a TEM image of PbSe nanoparticles deposited on a TEM grid under the optimum growth condition. The uniform distribution and the continuous connectivity between the particles are apparent in this micrograph.

4.1.3. Electrical Conductivity of PbSe QD Coatings Deposited by the LAS Process

The conductivity of a film of surfactant-capped PbSe coating is expected to have a high resistance as the charge carriers will have to hop from particle to particle across the 2-5 nm insulating surfactant barrier. Therefore, the conductivity of a film consisting of surfactant-free PbSe nanoparticles, such as the film shown in Fig. 4.13, should be much higher than that for a capped PbSe film. We have measured the I-V characteristics of films deposited across 2, 5, 10, and 20 μm gaps prepared on Ti-Au electrodes shown in Fig. 3.4. The thickness of each film was about 300 nm. The I-V characteristics of films deposited by the LAS process with and without the laser heating have been compared.

Fig 4.14 shows the I-V measurements across a 2μm gap of the films deposited with and without the laser on by LAS technique. The graph shows a more than three orders of magnitude enhancement in current for films deposited with laser compared to that of a film deposited without laser heating. This is even higher than the measured conductivity of drop-casted or spin coated films published in literatures.[39,40,41]

It is clear that in absence of insulating organic ligands between adjacent particles, the hopping distance for charge carriers is significantly decreased resulting in higher conductivity. This similar to what was observed for a collection of PbSe nanoparticles that were washed and annealed to remove the surfactants.[39]

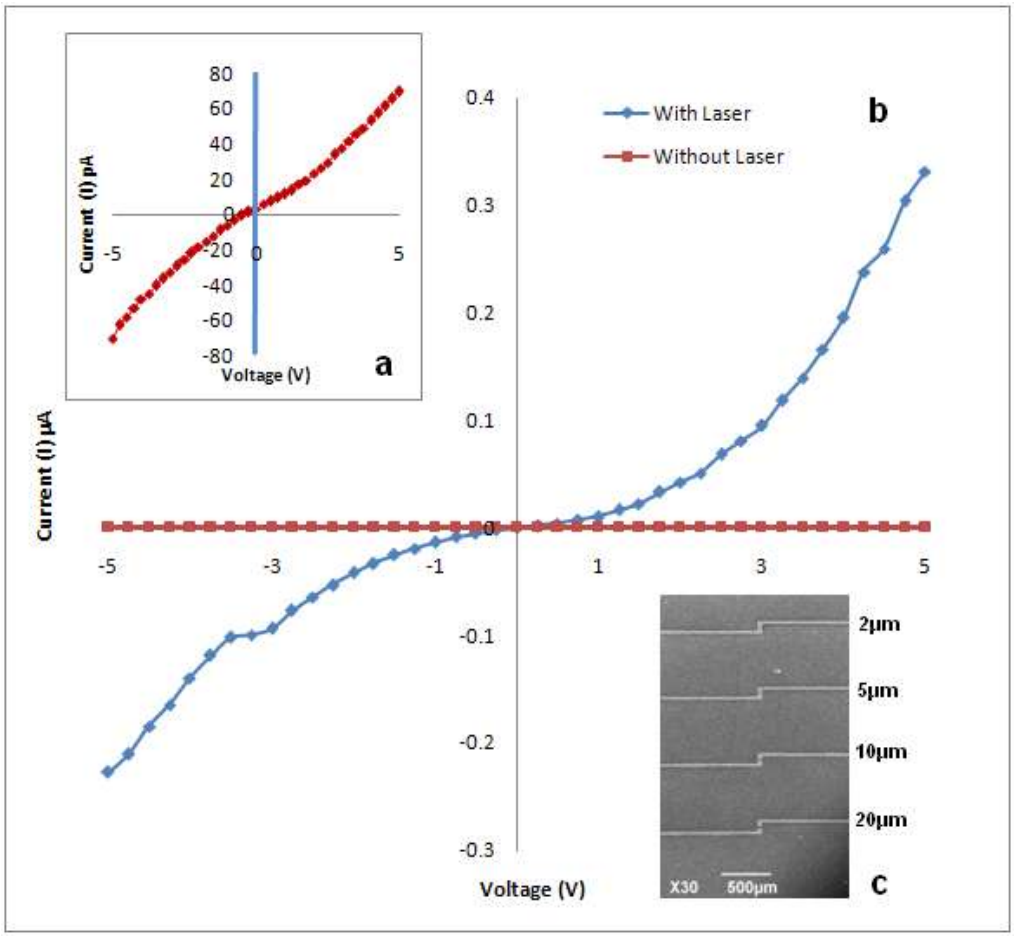

Fig. 4.14: I-V curve of PbSe Qd films deposited by LAS technique across 2µm gap between Ti/Au electrodes with and without the laser on. The inset (a) is the same graph as in (a), with current in pA scale to show the current in the film without the laser heating. (c) Au/Ti Electrodes on glass substrate. (In collaboration with Dr. Jiang's lab)

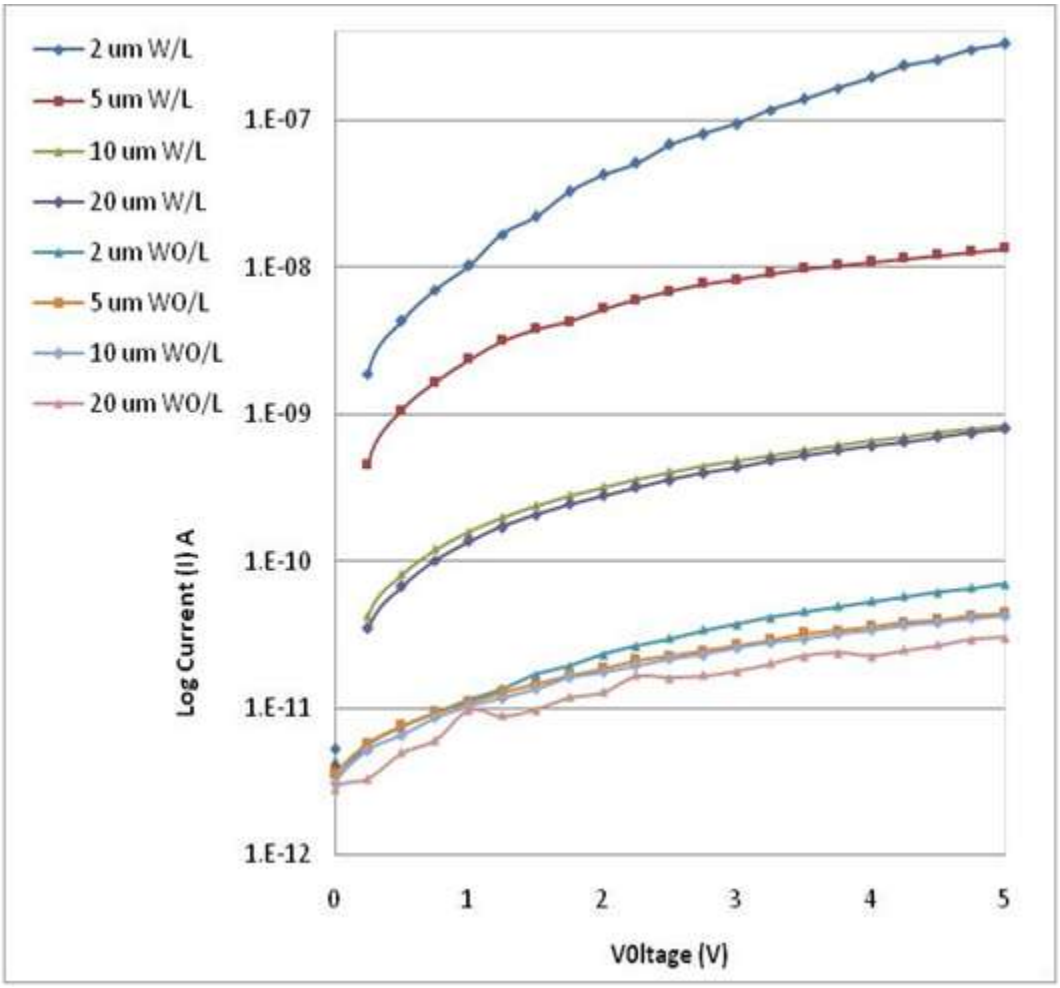

Fig. 4.15: Current Vs Voltage graph for different gap sizes. W/L: Laser is ON and WO/L: Laser OFF. (Provided by Dr. Jiang's lab)

The Fig 4.15 shows the current passed through the films deposited with laser ON compared to laser OFF for different gap sizes. Based on these results, summarized in Fig. 4.15, films of capped PbSe coatings showed very little variation in film resistance with the electrode gap size. That means electron conduction is dominated by the interparticle gap produced by the presence of the surfactant. On the other hand, the surfactant-free nanoparticle coatings show a drastic change in resistance with changing gap size. This is expected if the length of percolation paths, which depends on the dimensionality of the path, becomes shorter with decreasing gap spacing. However,

above a gap dimension of 10 µm, resistance change became negligible. (This will be discussed in section 5.1.3).

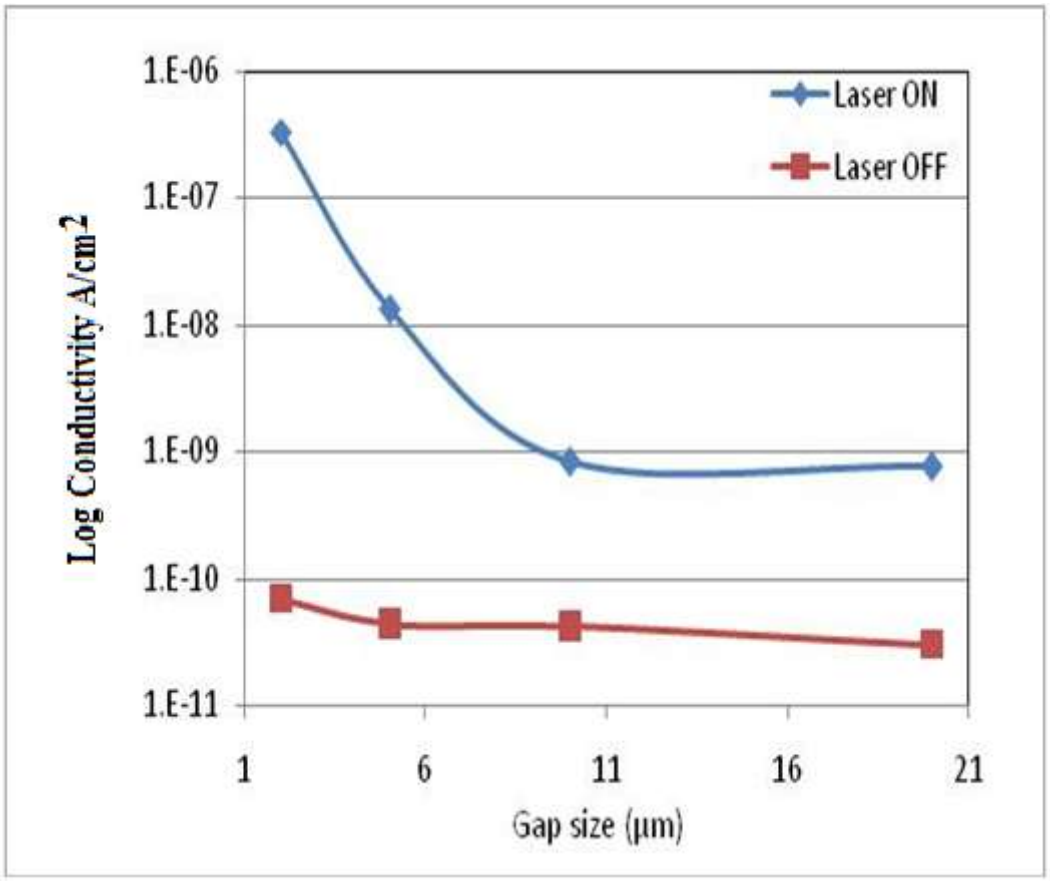

Fig. 4.16: Change in conductivity with the gap size. The current values were obtained at 5V bias voltage.

4.1.4. Temperature Dependent Conductivity Measurement

The temperature-dependent conductivity of surfactant free PbSe quantum dots was measured by using a four-point-probe method. The samples for this measurement were prepared by depositing surfactant-free PbSe films on glass substrates by the LAS process. The film thicknesses were in the range of 500-600 nm. Subsequent to film

growth, four aluminum contacts were deposited on the film by thermal evaporation through shadow mask as shown in Fig 4.17.

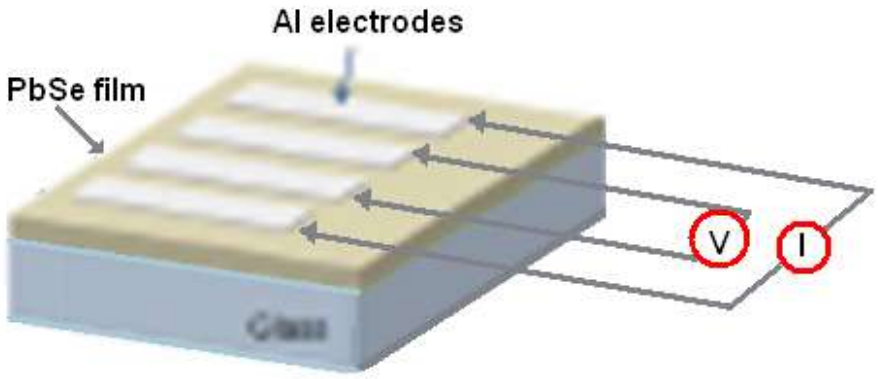

Fig 4.17: Sample made for temperature dependent conductivity measurements

The four-point-probe technique was used to measure the film conductivity, where current was applied across the outer contacts while the voltage was measured across the inner contacts (1mm apart) at different temperatures. The sample was mounted in a closed-cycle cryostat that enabled temperature variation from room temperature to 40 K. The temperature was reduced from 300K to 40K in 10K intervals and the variation in voltage was observed. Since the dimension of the conductive path was defined, the voltages were converted to conductivity (σ) using the relation $\sigma = I\,\ell/VA$. The graph in Fig. 4.17 shows the change in conductivity with the temperature.

The temperature dependent conductivity of QD films studied by a four-point technique indicated three different transport regimes (Fig. 4.18). In the region where the temperature is above 250 K the $\ln\sigma(T)$ vs. T plots showed a linear behavior describing a functional dependence of the form $\ln\sigma(T) = -(E/k_BT) + \ln\sigma_o$, where E is the activation

energy and σ_o the conductivity of the material at T= 0K. In the temperature range of 250K - 200K graph shows a behavior that fits an equation of the form $\ln\sigma(T) = -(T_o/T)^P + \ln\sigma_o$, which corresponds to hopping conduction, where P can fall within the range of ¼ to 1. (P=1/4 is known as Mott's variable Range Hopping (M-VRH) and P=1/2 known as Efros-Shklovskii variable range hopping (ES-VRH)) [39]. From 200 K to about 110 K, the conductance became less dependent on temperature, indicating a tunneling mechanism.

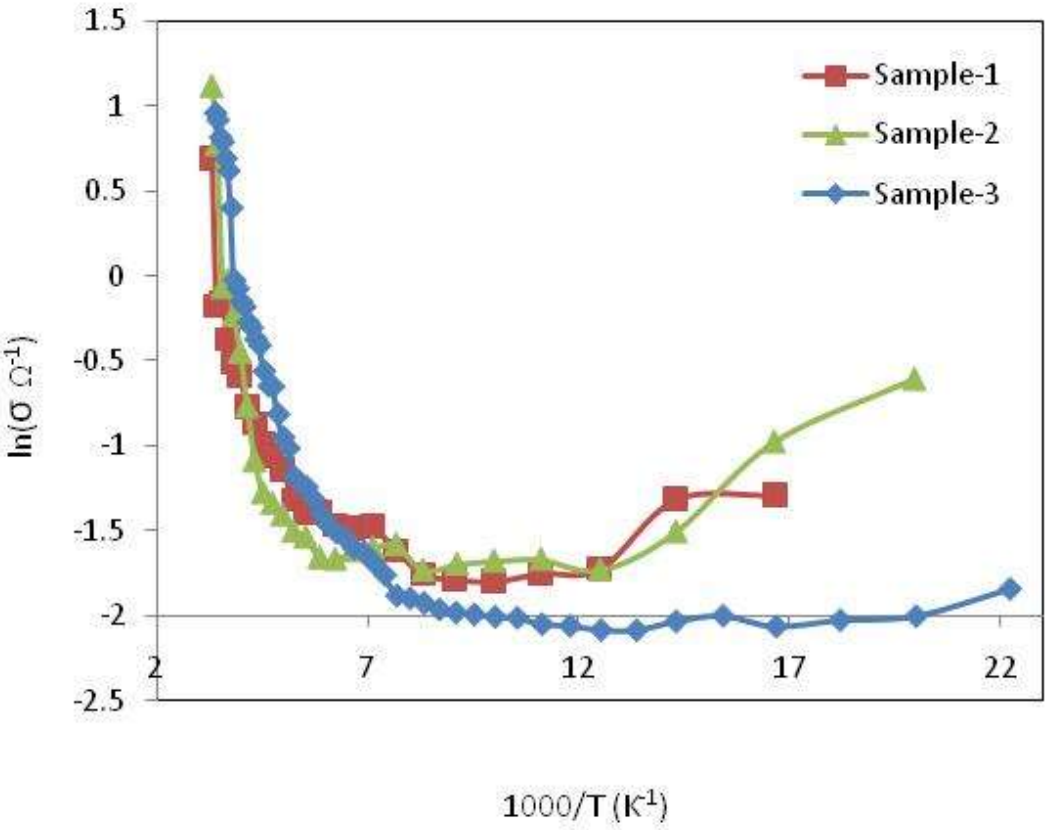

Fig. 4.18: The graph shows the conductivity σ (log scale) versus the inverse of T for three PbSe QDs samples deposited by LASP technique.

However below 110 K, conductance turns to metallic behavior that has not been observed for capped QD assemblies. This phenomenon can be explained by using theoretical models that have been developed based on the quantum mechanical coupling of energy levels of adjacent QDs, facilitated by negligible inter-particle separations [4,43,44]. The coupling energy between two neighboring QD is given by $h\Gamma$, where h is the Planck constant and Γ is the tunneling rate between two ground state orbitals. In the weak coupling regime where $h\Gamma << k_BT$, the tunneling is restricted to adjacent QDs. However, in the strong coupling regime ($h\Gamma > k_BT$), orbitals may extend over many QDs forming a continuous band that enhances carrier transport. This condition may be satisfied for our films at low temperatures since the inter-particle spacing is negligible.

4.1.5. Photocurrent Measurement

4.1.5.1. Direct Current (DC) Measurements

The PbSe QDs samples for studying photogenerated current were fabricated by depositing a 500nm PbSe quantum dot layer using Laser Assisted Spray technique on an Indium tin oxide (ITO) - coated glass substrate. The ITO- coated glass substrate is a commonly used transparent conducting film that has a surface resistivity of about 15Ω square $^{-1}$. The substrates were first cleaned by ultrasonication in acetone and methanol and dried in a nitrogen flow. First, PbSe QDs film was deposited on a cleaned ITO coated glass substrate. Then, Silver (Ag) electrodes (as shown in Fig 4.18) were made by thermal evaporation using a shadow mask. Current generated by application of a bias

voltage between -5V to 5V was measured by a Keithley SMU 2400 voltage source under an illumination intensity of 80mWm^{-2}.

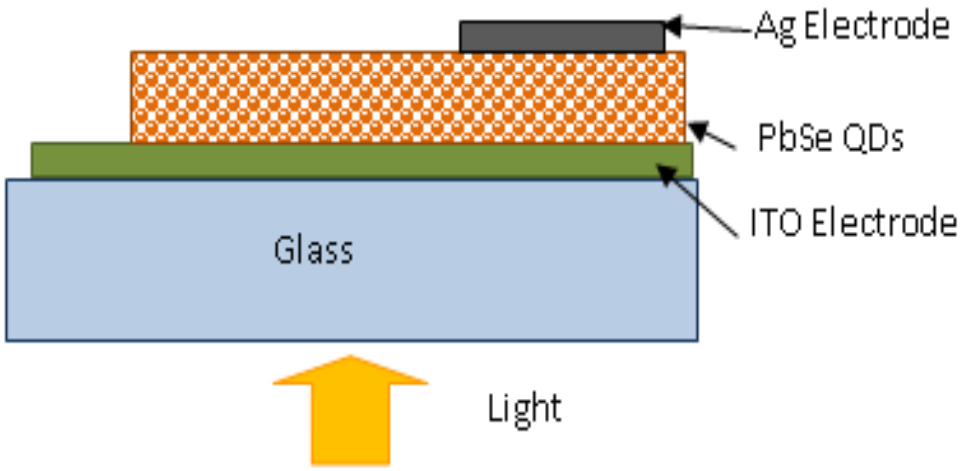

Fig. 4.19: Sample made for photocurrent measurement by Laser Assisted Spray technique.

Fig 4.20 shows the current response of the surfactant-free PbSe QD device under illumination. It is very clear that under illumination the current values at each voltage level are higher than the dark current values. This confirms the photo-induced carrier generation in the surfactant- free PbSe QDs. The different shapes in positive and negative voltage sides were observed due to the different work functions of the electrodes. The positive side forms a Schottky barrier at Ag (4.74eV) and PbSe (4.2eV) junction while negative side forms a near ohmic contact at PbSe (4.82 eV) and ITO (4.6eV) junction. This Schottky barrier formation can be described by a simple diode equation.

$$I = I_s\left[\exp\left(\frac{qV}{nk_BT}\right) - 1\right] \qquad 4.3$$

Where I_s is the saturation current, q is the electronic charge, V is the potential drop across the junction, n is the ideality factor, k_B is a Boltzmann's constant, and T is the temperature.

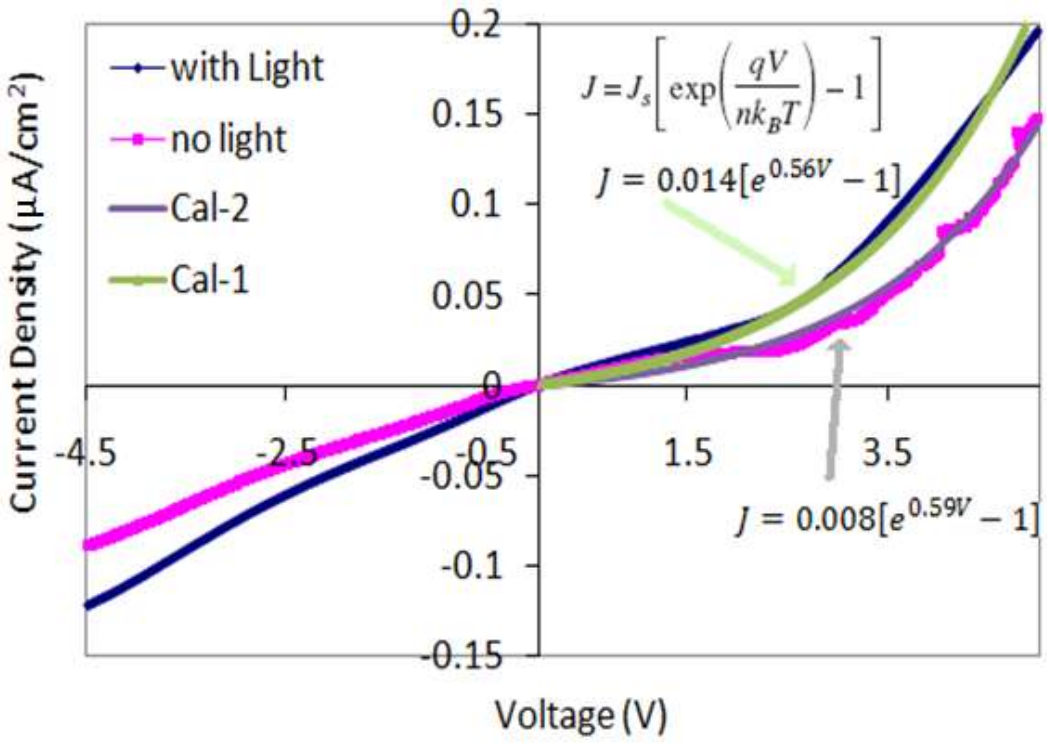

Fig. 4.20: The graph of applied voltage vs current density through surfactant free PbSe quantum dots film.

4.1.5.2. Photo-Generated Current by a Pulse Laser

The capacitance of the QD structure that is sandwiched between two metallic electrodes can become an active element of the circuit if the generated current changes with a specific frequency. A circuit has been designed with pulsed laser excitation to generate a photocurrent that follows the frequency of the laser pulses. The circuit used for these measurements is shown in Fig. 4.21. The photocurrent was measured

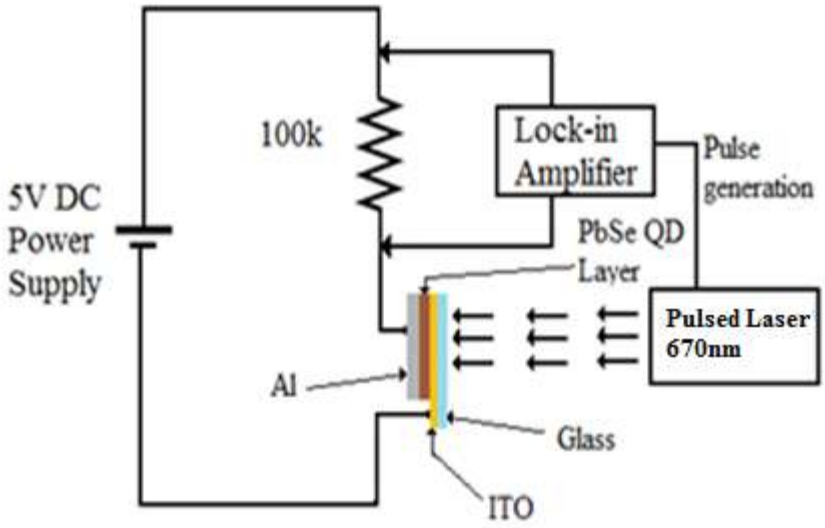

Fig. 4.21: Circuit diagram for detecting photocurrent generated by a pulsed laser.

under constant bias voltage applied between the device electrodes for various laser-pulse intensities. To generate carriers in the quantum dot layer that is sandwiched between the electrodes, laser pulses with a wavelength of 670nm were used. The circuit shown in Fig. 4.21 was used to measure the photo-generated current. The generated electrons and holes drift to opposite electrodes due to applied electric field across the device structure and flow out of the external circuit as a photocurrent. The generated photocurrent was measured with a "lock-in amplifier" synchronized with the pulse laser. The average laser power was changed from 0 to 4.2mW by changing the input voltage to the device from 0 to 5V. The lock-in amplifier allows the measurement of only the current generated by the laser pulse, which is the photocurrent. The series resistor in the circuit amplifies and converts the current passing through it to generate the measured voltage.

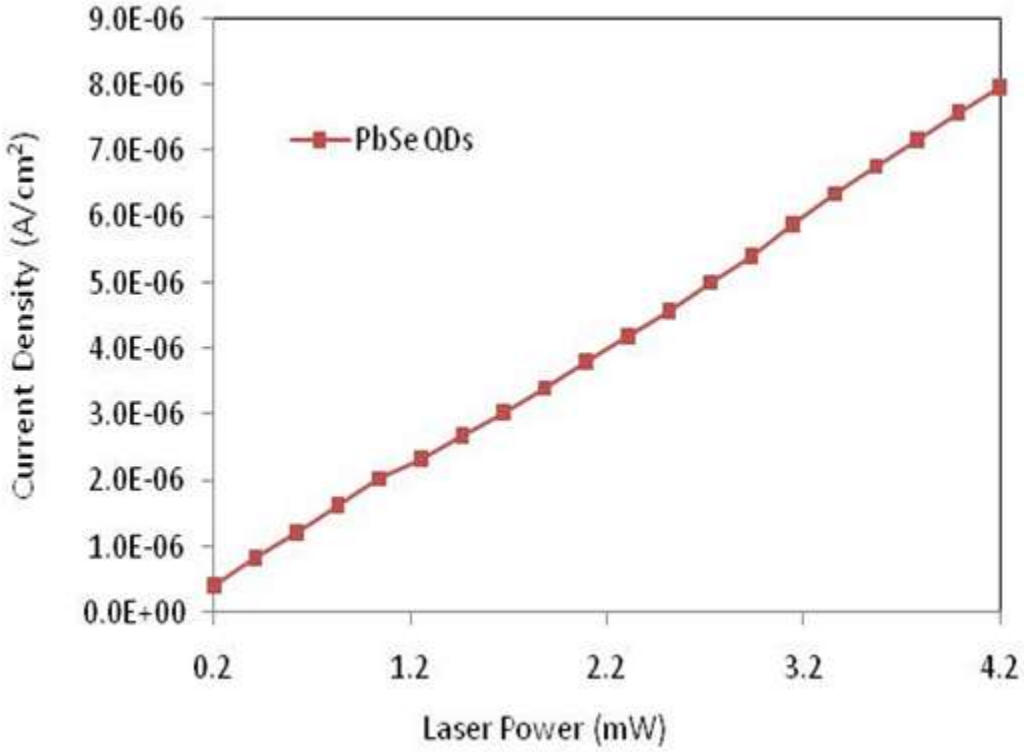

Fig. 4.22: The graph of photo-generated current from the QD device at various laser power levels.

The graph in Fig 4.22 shows the measured photo-generated current at various laser power levels. According to this result the carrier generation rate is proportional to the incident light intensity and did not show any hint of saturation up to the maximum power used.

4.2. Characterization of P3HT Polymer Coatings

4.2.1. Crystallinity

Crystallinity of the P3HT polymer was studied by X-Ray Diffraction method. Since P3HT has very low angle peaks, the scanning angles were set from 4^{o} to 30^{o} with

0.02^{o} increments in 3sec/steps. The Fig. 4.23 shows the XRD pattern of the P3HT polymer on the glass substrate deposited by LAS deposition technique that was used for the growth of QD layers, except the aerosol coming out of the nozzle was not heated by the laser.

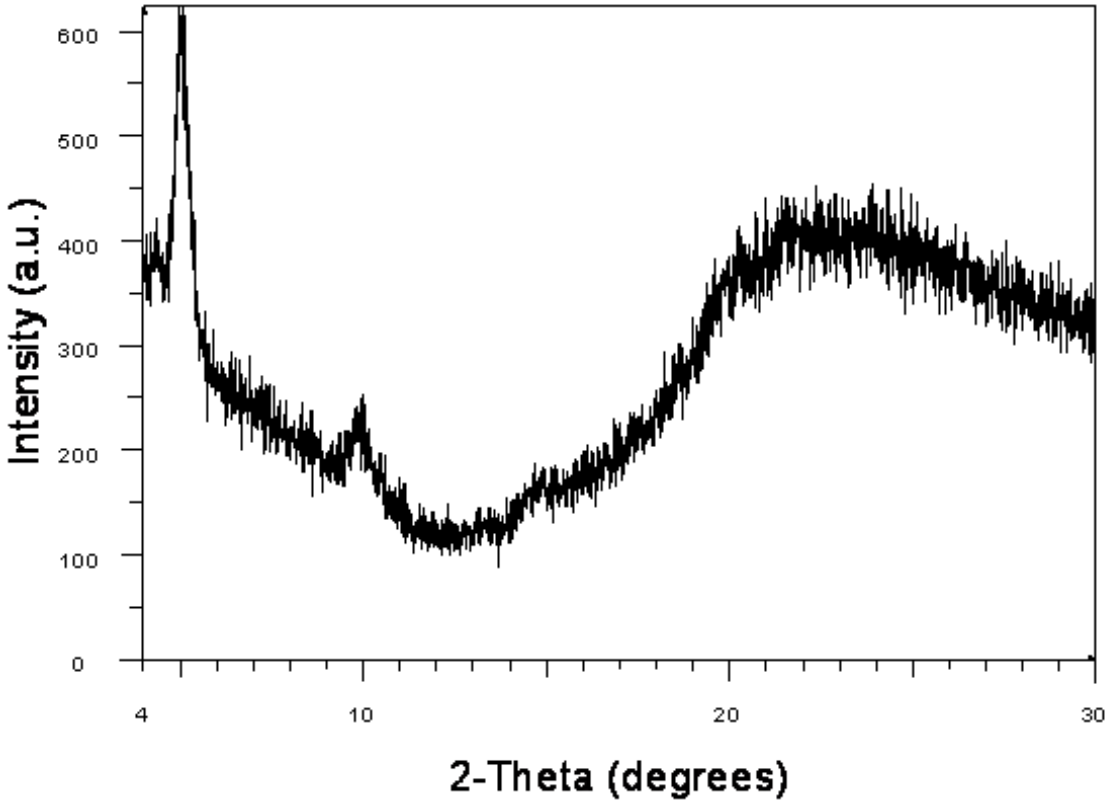

Fig. 4.23: XRD pattern of P3HT polymer coating deposited by LASP technique on glass substrate heat up to 60 ^{o}C.

XRD pattern clearly shows the crystalline peaks corresponding to P3HT polymer. The crystallinity of the P3HT films deposited by this method was very similar to the films deposited by spin coating.[45]

4.2.2. Optical Characterization

The optimum growth temperature was obtained by studying the optical properties of films deposited at different temperatures. Under ideal conditions the absorption by the film should resemble that for a high quality spin-coated film. Several samples were deposited at substrate temperatures of 200 ^{o}C, 100 ^{o}C and 60 ^{o}C and the absorptions were studied.

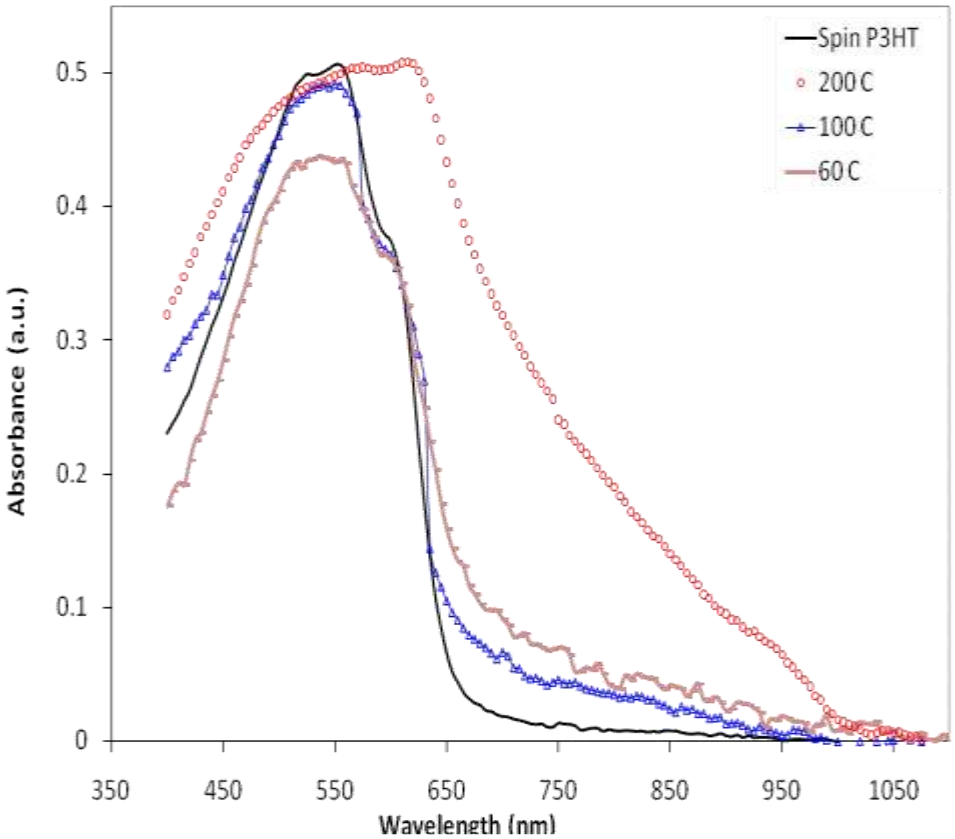

Fig. 4.24: Absorption spectrum of P3HT films deposited by Spray Pyrolysis at substrate temperature 200 ^{o}C, 100 ^{o}C and 60 ^{o}C compared to spin-coated film. (In collaboration with Dr. Jiang's lab)

Fig 4.24 shows the absorption spectra of P3HT films deposited by the spray process at different substrate temperatures. The spectra (except at 200^{o}C) clearly show first transition at 610nm, second transition at 555nm and third transition at 530nm, which confirms the unique absorption property of the P3HT material. But when the substrate temperature was at 200 ^{o}C, the material changed its absorption property due to decomposition of the polymer at high temperatures. The samples deposited at 100 ^{o}C and 60 ^{o}C show absorption spectra that are identical to that of spin-coated films. But when comparing 100 ^{o}C and 60 ^{o}C substrate temperatures, the 100^{o}C shows well defined peaks compared to those of the films deposited at 60 ^{o}C. Therefore, one can identify 100 ^{o}C as the optimum temperature for P3HT film deposition by the spray pyrolysis technique.

4.2.3. Photo-Generated Current by Pulse Laser Excitation

The experiment in section 4.1.5.2 was used to determine photo-generated current in P3HT polymer structure that is sandwiched between two metallic electrodes. The photocurrent was measured with various laser-pulse intensities under constant bias voltage applied between the device electrodes. The graph in Fig 4.25 shows the photo-generated current value recorded at various laser power levels. The graph shows the linear increment of photo-generated current with increasing laser power. This is very good evidence of photo-generated carriers in the fabricated polymer device.

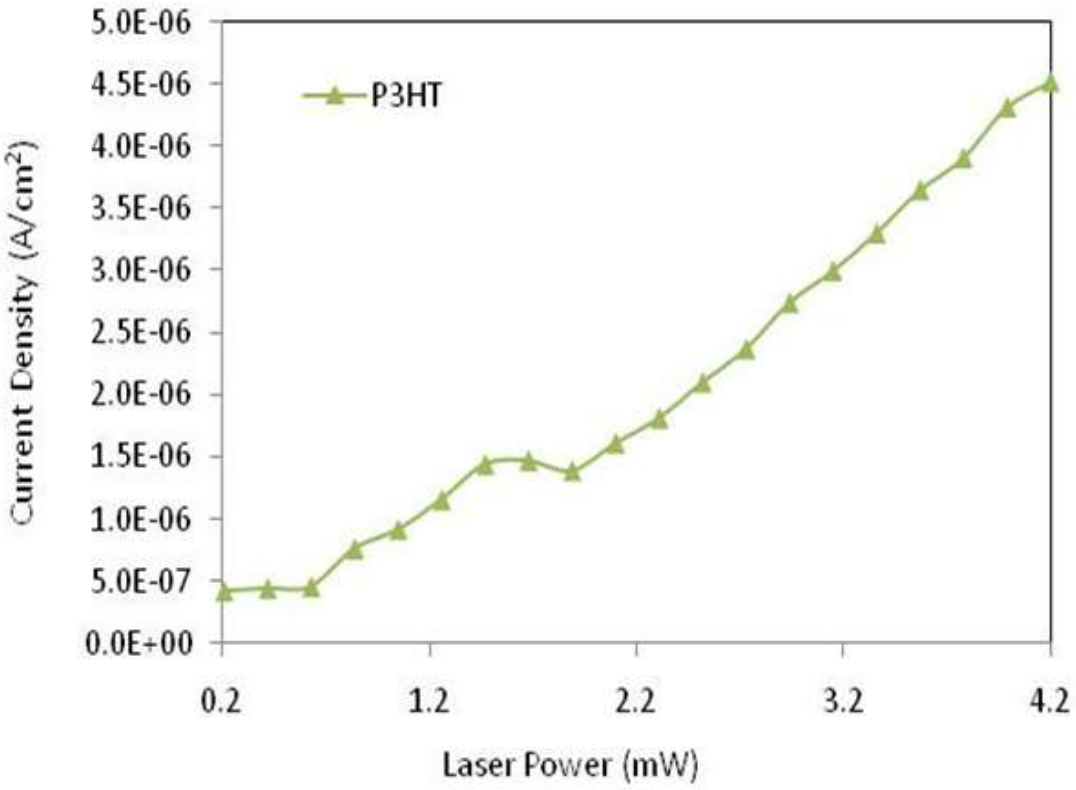

Fig. 4.25: The graph of photo-generated current in the P3HT layer sandwich between ITO and Al electrodes at various laser power levels.

4.3. Characterization of PbSe QDs/P3HT Hybrid Composite

Characterization of PbSe QDs/P3HT hybrid composite was done by using TEM and XRD studies. First, the XRD studies were performed on thicker samples to determine the crystallinity of the material. Since P3HT has very low angle peaks, the scanning angles were set from 4^{o} to 60^{o} with 0.02^{o} increments in 1sec/step. The results are shown in Fig. 4.26.

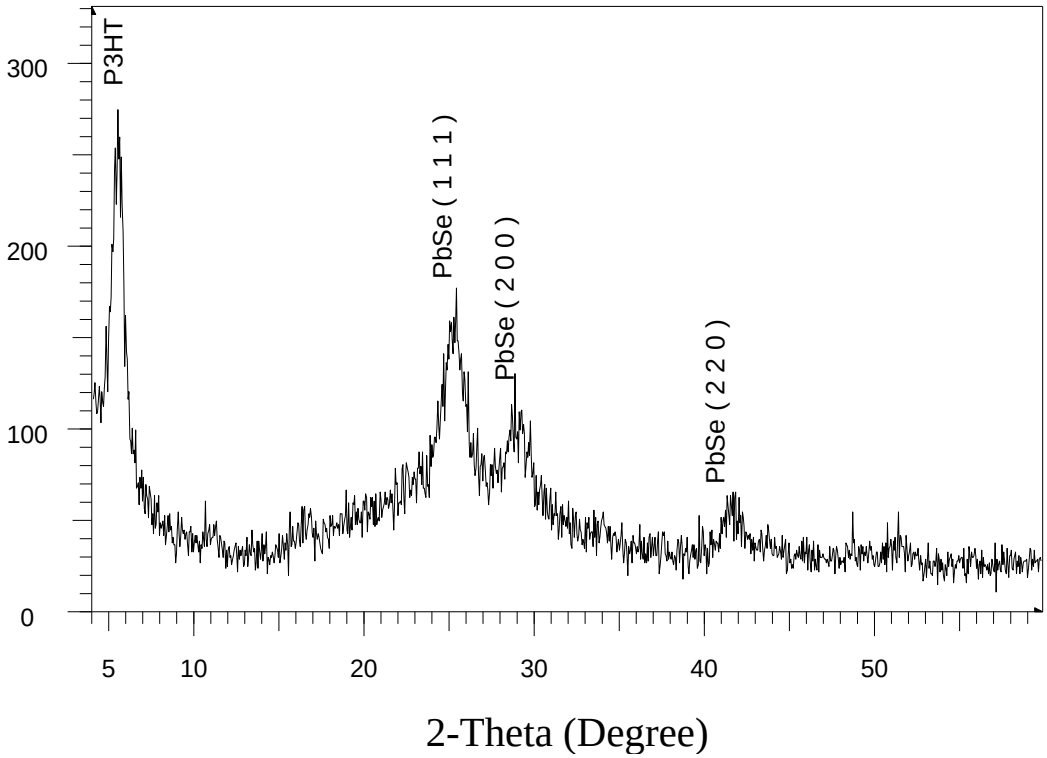

Fig. 4.26: XRD pattern of PbSe QDs/P3HT hybrid composite deposited by laser Assisted Co-Deposition.

XRD pattern clearly shows the crystalline peaks corresponding to P3HT polymer and the PbSe QDs. P3HT shows sharp crystalline peaks due to large crystalline particles while PbSe shows broad peaks due to nanocrystalline particles. Also proportionalized peaks of two materials in the films confirm the possibility of depositing two materials in Laser Assisted Co-Deposition system.

The samples for TEM were prepared on a carbon coated TEM grid, purchased from Electron Microscopy Sciences to investigate the initial formation of PbSe QDs/P3HT hybrid composite. The result is shown is Fig. 4.27.

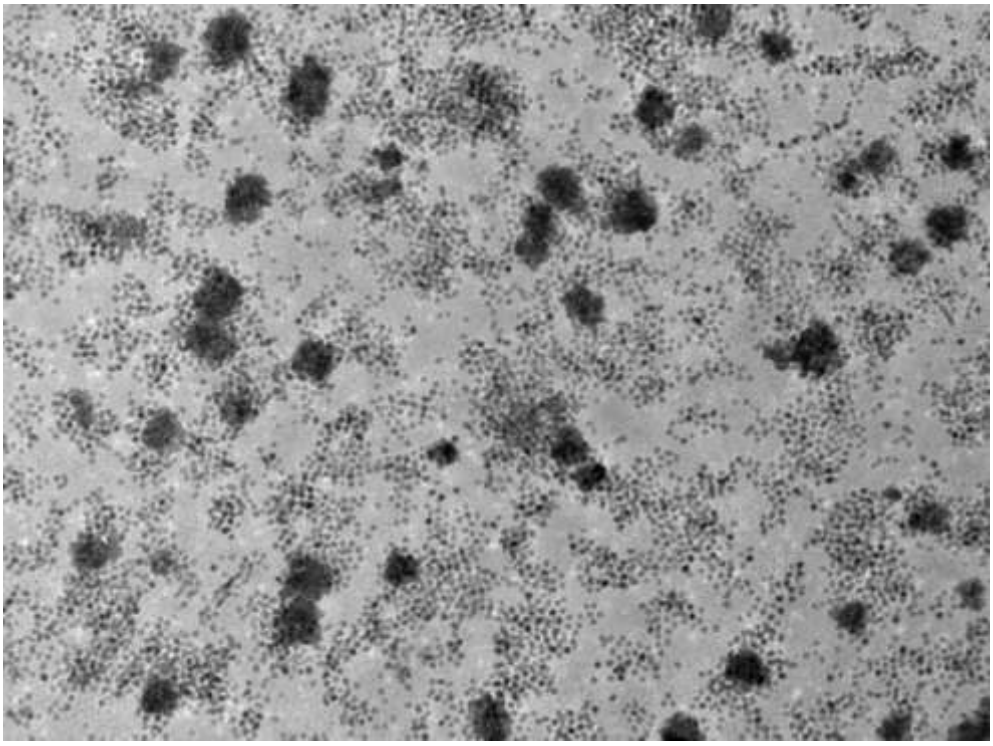

Fig. 4.27: TEM image shows the initial formation of P3HT polymer and the PbSe NC on the film.

The TEM image shows the initial formation of the hybrid composite on the carbon coated TEM grid. A high growth rate of PbSe nanocrystals is visible on the film. Also, the image clearly shows the uniform distribution of PbSe NC and P3HT in the hybrid composite.

4.3.1. Photo-Generated Current Measurements

The experiment in section 4.1.5.2 was repeated for measuring photo-generated current in the PbSe QDs/ P3HT polymer hybrid composite that is sandwiched between two metallic electrodes. As described in that section the photo-generated current was

measured at various laser energy levels. The graph in Fig 4.28 shows the change in photo-generated current in the PbSe QDs/ P3HT polymer composite.

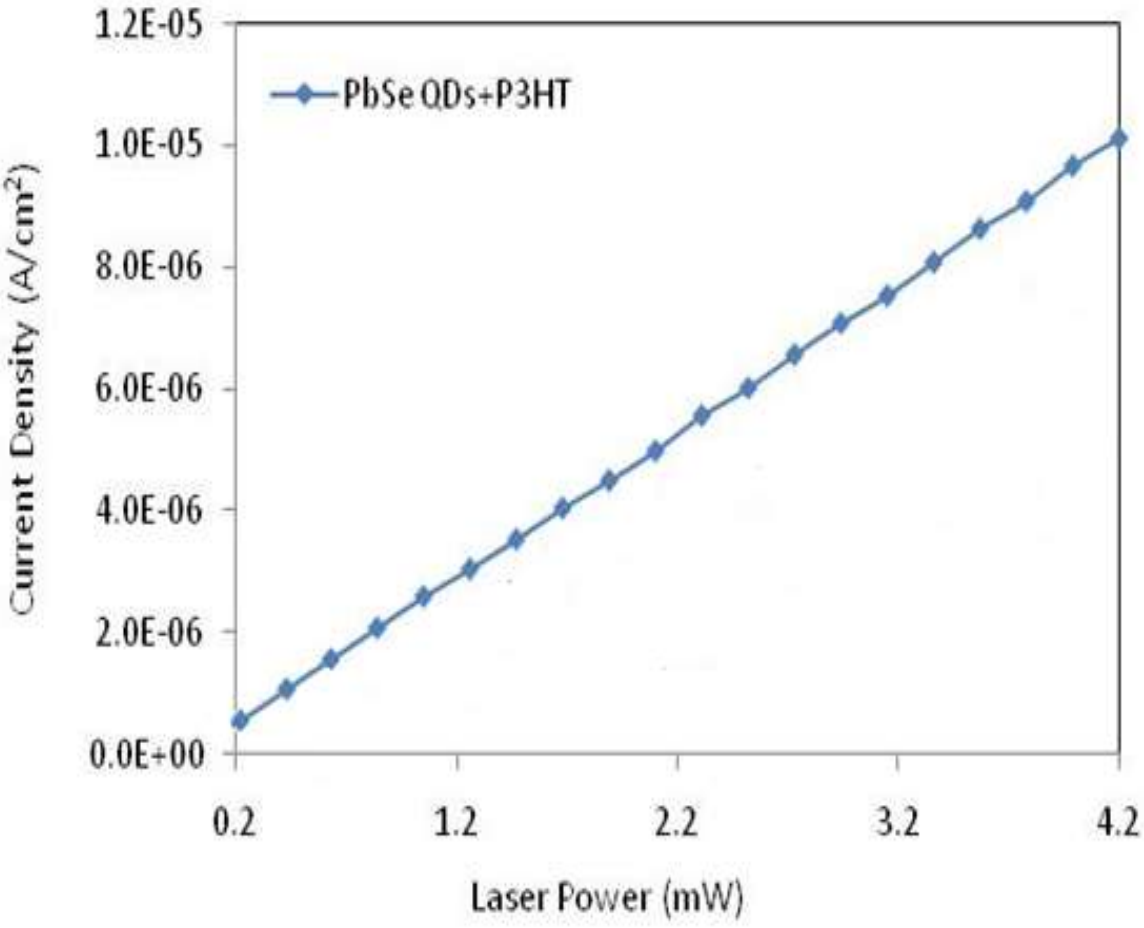

Fig. 4.28: The graph of normalized photo-generated current in the PbSe QDs/P3HT layer sandwich between ITO and Al electrodes at various laser power levels.

The graph in Fig 4.28 shows the normalized photo-generated currents in the samples of PbSe QDs/P3HT polymer hybrid composite. The graph clearly shows the photo-current generation in the new hybrid composite. The photocurrent of this composite arises from the efficient charge separation at the polymer- NQD/nanorod interface and the enhanced electron transport in the structure due to the relatively high intrinsic carrier mobility in inorganic semiconductor NQDs. When the light is illuminated

on this PbSe QDs/P3HT composite, both P3HT polymer and the PbSe QDs generate the electron and hole during the light absorption, the hole dissociated to the P3HT polymer due to overlap of wave-function between PbSe QD and the P3HT polymer while the electron hops between the PbSe QDs towards the Al electrodes. Since this composite contained surfactant free PbSe QDs, the process becomes much more efficient compared to the photo-generated current value reported in the literature [45]. Therefore, the deposition of PbSe QDs/ P3HT polymer composite by the Laser Assisted co-Deposition technique is very promising in producing highly efficient and low-cost hybrid photovoltaic composites.

4.3.2. Frequency-Dependent Photo-Generated Current Measurements

Further investigation of the PbSe QDs/P3HT polymer composite was performed by using frequency-dependent photo-generated current measurements. This experiment was designed to study the internal capacitance of the composite layer that consists of surfactant free PbSe QDs and the P3HT polymer. The experiment was designed by using the setup shown in section 4.1.5.2. During this experiment, laser power level was kept constant while changing the triggering frequencies of the laser pulse. The triggering frequency of the laser was changed via lock-in-amplifier.

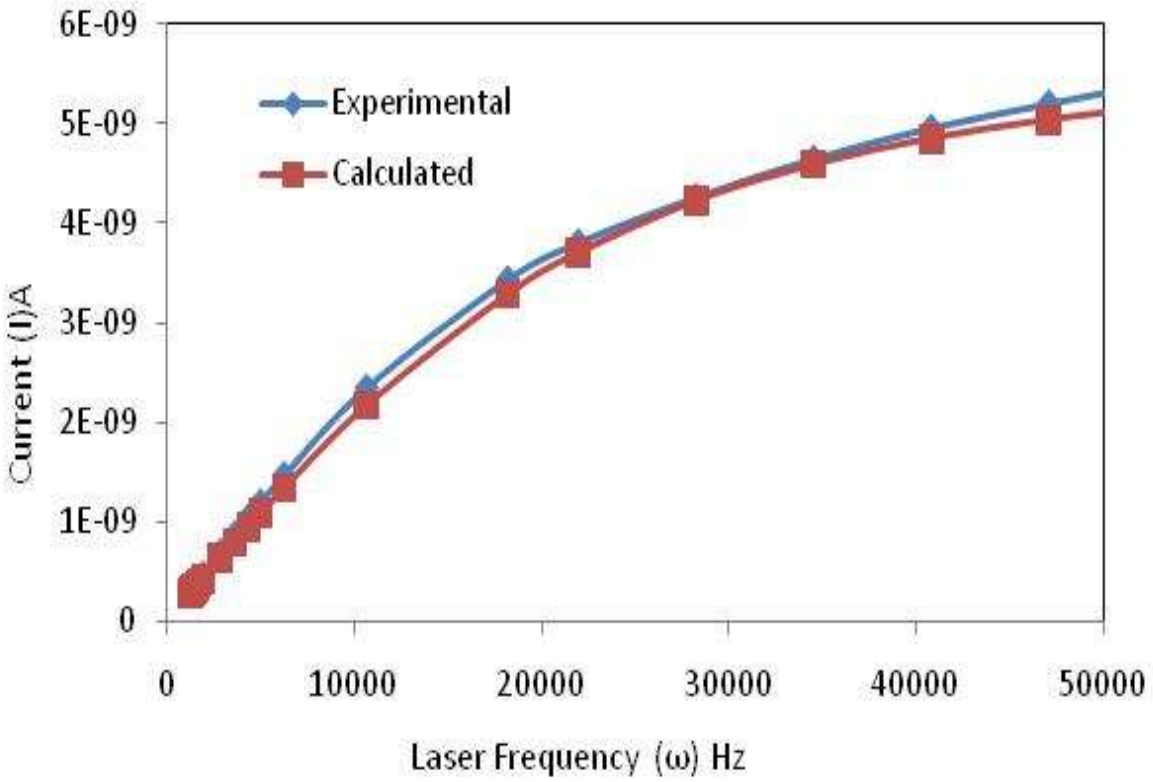

Fig. 4.29: The graph of calculated and experimental values for frequency-dependent photo-generated current through PbSe QDs/P3HT polymer composite.

The graph in Fig 4.29 shows the collected photo-generated current values and the values calculated from the model that was developed using the reactive capacitance of the composite. The graph shows the increment of photo-generated current across the device structure with increasing modulation frequency. This is very interesting since the power incident on the device is independent of the modulation frequency of the laser signal. This increment of this photo-current could be a result of changing reactive capacitance of the device structure. In order to investigate the result, we studied the changing reactive capacitance in an equivalent RC (Resistor-Capacitor) circuit under same frequency conditions. The voltage and capacitor values for the equivalent RC circuit were obtained by the equation that is derived below.

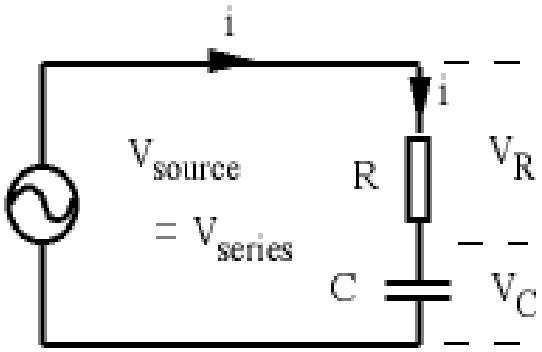

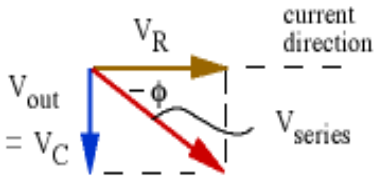

From Pythagoras' theorem:

$$V^2_{mRC} = V^2_{mR} + V^2_{mC}$$

$$V^2_{RC} = V^2_R + V^2_C$$

$$V^2_{RC} = (IR)^2 + \left(\frac{I}{\omega C}\right)^2$$

$$V_{RC} = \sqrt{(IR)^2 + \left(\frac{I}{\omega C}\right)^2}$$

$$= I\sqrt{R^2 + \left(\frac{1}{\omega C}\right)^2}$$

$$\frac{1}{I^2} = \frac{1}{V_{RC}^2 \omega^2 C^2} + \frac{R^2}{V_{RC}^2}$$

So, using the resistance and the capacitive reactance $\frac{1}{\omega C}$

This is similar to y = mx + c; and from the $1/I^2$ Vs $1/\omega^2$ graph one can calculate Source Voltage (V_{RC}) and the Capacitance (C).

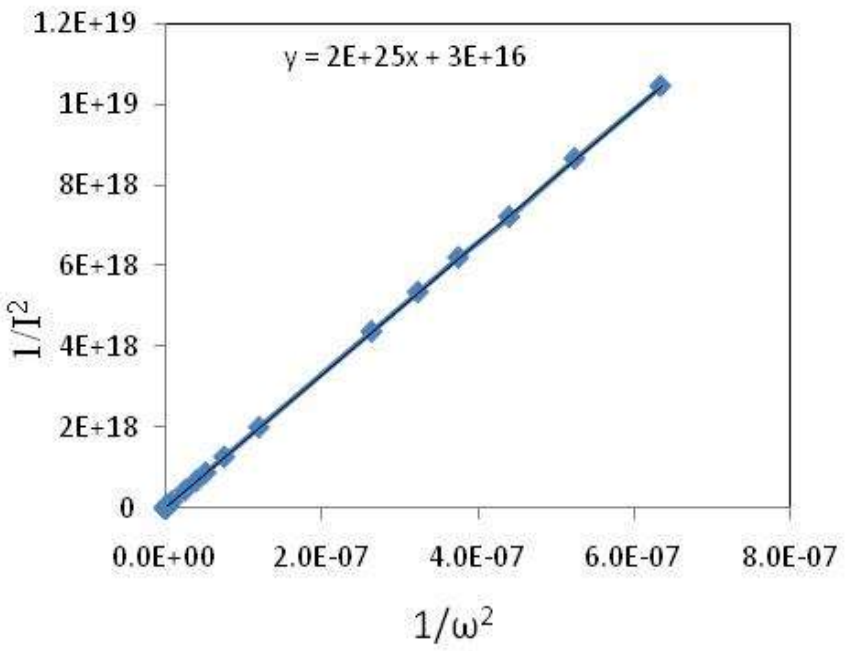

Fig. 4.30: Graph of $1/I^2$ Vs $1/\omega^2$

From the model that uses an equivalent RC circuit to explain the results, the capacitance and the photo-generated voltage of the device can be computed as $C = 3.8 \times 10^{-10}$ F and $V_{RC} = 5.773 \times 10^{-3}$V, respectively.

The experiment was extended for different DC bias voltages across the device. The corresponding capacitances were found at each bias voltage. This experiment was performed for investigating the carrier generation, built-in voltage, and depletion region within this material system. This C-V method has been used by several other groups in calculating interface properties of the semiconductor quantum dots films sandwiched between Aluminum and ITO electrodes [40]. The capacitance values obtained in this experiment were used to study the accumulated effect of each PbSe QD/P3HT polymer interfaces. The graph of C^{-1} vs V_{bias} was plotted due to hybrid nature of the interfaces. The following equation shows the C-V relationship in our material system.

$$\frac{1}{C} = \frac{1}{qN_a}\left(V_{bi} - V\right) \qquad 4.3$$

where N_a is a carrier density, V_{bi} is built-in voltage and q is charge of an electron. The graph in Fig 4.31 shows the C^{-1} for the device structure at several V_{bias} conditions. Here, the slope of the graph provides information about carrier density while intercept of the graph shows the built-in voltage of the device structure. The graph shows a linear increment of 1/C as the bias voltage changes from positive values to negative values. From the slope of the graph, number of carrier N_a and the built-in voltage V_{bi} of the device structure can be calculated as 1.04×10^9 and 0.833eV, respectively.

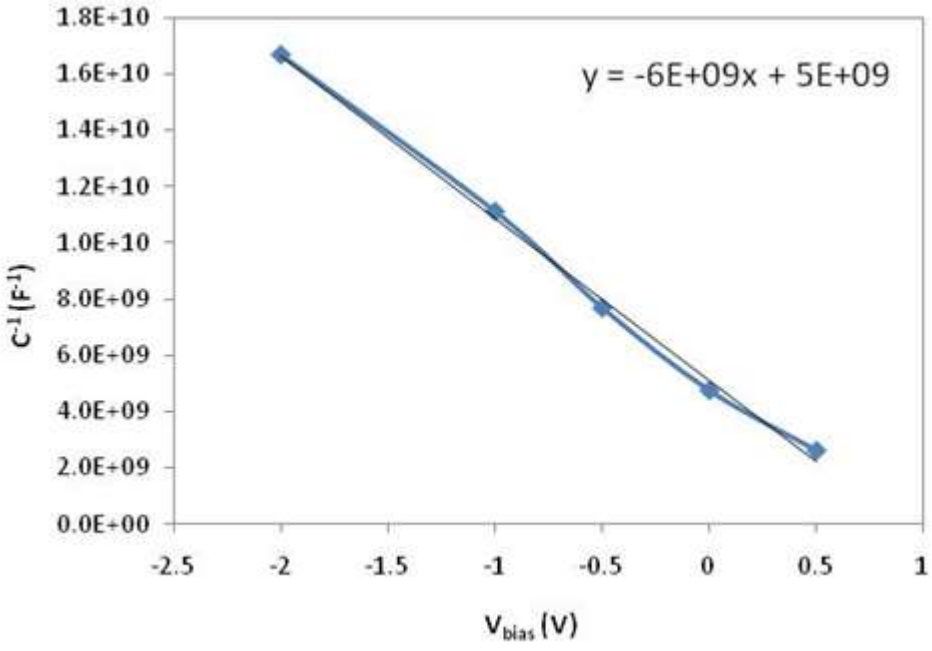

Fig. 4.31: Graph of 1/C Vs bias Voltage applied to the device structure.

4.4. Photo-Generated Current Measurement of the Solar Cell Structure

The photocurrent measurement of the solar device fabricated in section 3.6 was studied by using the experimental set up designed in section 4.1.5.2. The generation of photocurrent at various power levels of the laser was measured. In this experiment, the device was connected in two opposite configurations named toward built-in Electric field (the positive side of the DC power supply is connected to the Al electrode while negative side is connected to the ITO electrode) and Opposite to built-in Electric field (the negative side of the DC power supply is connected to the Al electrode while positive side is connected to the ITO electrode).

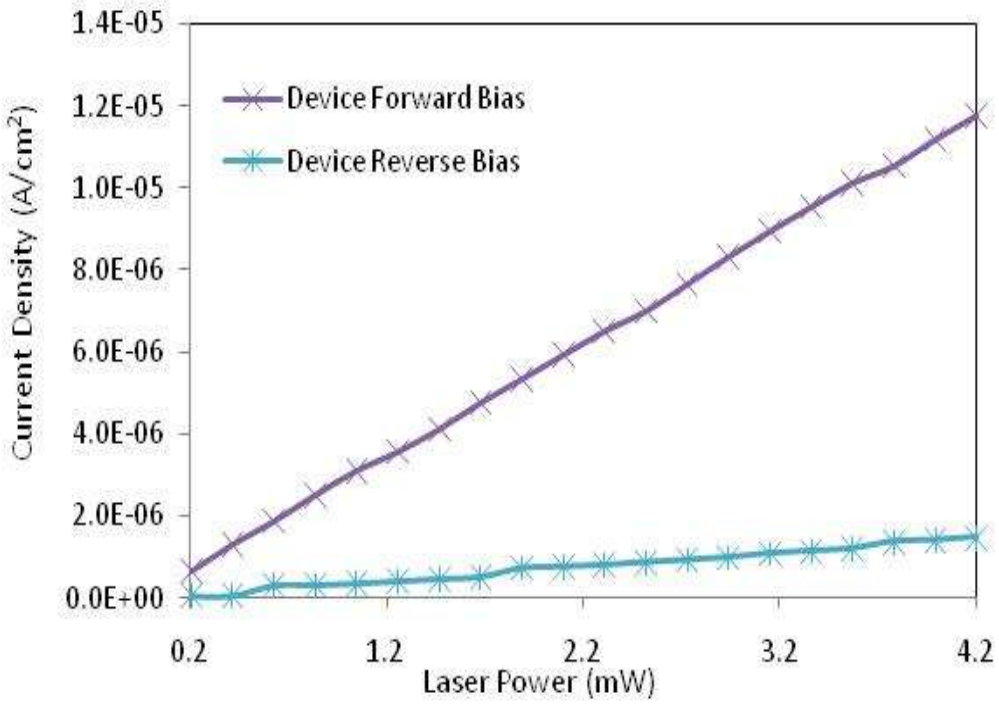

Fig. 4.32: The graph of photo-generated current in the PbSe QDs/P3HT Solar Device at various laser power levels when Forward and Reverse bias condition.

The graph in Fig. 4.32 shows the photo-generated current values at different laser power levels**.** The graph shows a higher current for forward bias condition and a lower current for reverse bias condition. Also, when comparing the same bias condition with Al/PbSe-P3HT/ITO and Al/PbSe-P3HT/PEDOT/ITO structures, the one which has PEDOT shows higher current values indicating higher charge extraction. The reason for this higher current can be explained using the work function of ITO layer. The work function of ITO is 4.6eV.When the ITO is coated with PEDOT, due to the interface effect, it reduces the work function of the ITO below 4.6eV. Then, the electric field created by the structure containing PEDOT is higher than electric field created by ITO-Al electrodes. At higher electric fields, a higher electron dissociation rate is possible. The "Opposite to the E. field" configuration shows low current because of the potential barrier between PbSe QDs and P3HT.

CHAPTER 5

DISCUSSION

5.1. Synthesis of PbSe Nanocrystals

A noncoordinating solvent method has been used successfully to synthesize PbSe nanocrystals. This method not only eliminates the extremely toxic organometallic precursors and most phosphine-containing solvents used in other methods but also provides a low-cost technique for the growth of high-quality semiconductor nanocrystals. Since the nucleation of PbSe largely depends on the reaction temperature, lowering the temperature can completely stop the nucleation process, and thus control the particle size distribution very easily. The particles were found to be single crystal as-grown and the optical absorption investigations showed them to be in quantum confined states.

5.2. LAS Deposition of Surfactant Free PbSe Nanocrystals

The conventional method of synthesizing semiconductor quantum dots always consists of 1-2nm surfactant coating around the quantum dot even after thorough cleaning/washing. The surfactant around the quantum dot significantly lowers the conductivity in a coating containing a collection of QDs. The presence of the surfactants

is also expected to hinder the dissociation of the excitons generated in photo absorption. Use of the LAS methods enabled the fabrication of PbSe QDs without the surfactants. In this process the droplets containing PbSe quantum dots and hexane pass through a laser heated region that helps to evaporate the solvent as well as the organic surfactants forming surfactant-free QDs. It was shown that the temperature of the plume can be controlled by controlling the flow rate in the process, and the optimum temperature to form closely packed QDs without noticeable recrystallization was found to be between 150-200^{o}C. The deposition of the films at optimum temperature showed that the crystallinity and the optical properties of the quantum dots can be retained. The 40.1 nm absorption peaks shift towards high energy observed in the absorption spectrum of the LAS deposited films corresponds to a reduction in quantum dot size.

5.2.1. Charge Transport in QD Films

The surfactant around the quantum dots reduces the electron mobility between the quantum dots. The studies have revealed that the low electronic conductivity in semiconductor nanocrystal arrays is because of poor exchange coupling and large concentrations of surface dangling bonds that trap carriers in mid-gap states.[4, 46] Annealing the nanocrystalline film into a high temperature can increase the film conductance due to the removal of the surfactants. However, annealing has also been shown to depredate the QD. In LAS deposition technique, the removal of the ligands is completely achieved by the laser interaction, and therefore, prolonged heating at the substrate is not required. As observed in TEM micrographs the removal of ligand allows

the formation of intimate contacts between adjacent nanocrystals while preserving the distinct excitonic features. Also, the mobility of the electron is increased due to removal of trap states around the nanocrystals and overlap of wavefuctions.

The current-voltage (I-V) characteristics of LAS deposited and drop-casted films were conducted by depositing films within a 2 μm gap between two Ti-gold electrodes deposited on a glass substrate. The measurements were made at room temperature for films with similar thicknesses. The films do not show a threshold voltage for current flow resulting from Coulomb blockade that has been reported for monolayers of self-assembled metal and semiconductor nanoparticle arrays[4,47]. If present, such a threshold in our measurements may have been masked by the parasitic conduction in glass at room temperature. Fig.4.14 shows the measured current for an applied voltage across the 2 μm gap. The current produced by the LAS deposited film is more than three orders of magnitude larger than that measured for the drop-casted film, which indicates a low resistant carrier percolation path across the electrodes. Several previous experiments on mono and multilayered nanoparticle arrays have shown the IV characteristics to follow a functional dependence of the form $I \propto V^{\xi}$ where ξ is a scaling exponent[39,47,48]. The value of the exponent is related to the number of percolation paths available for current flow, and thus depends on the dimensionality of the junction[49]. For 1D arrays where only one path could carry the majority of the current, $\xi \approx 1$. For 2D arrays of lithographically-formed tunnel junctions, the experimentally observed dependence is $1.6 < \xi < 2.1$. For a junction of dimensionality slightly higher than 2D, the observed dependency is $2.1 < \xi < 2.7$. This mode of transport is in agreement with the 2.19 exponent we observed for the films grown by the LAS process.

5.2.2 Photoconductivity

Generation of photocurrent in both QD and QD/Polymer composite films have been demonstrated in this project. When the bias voltage exceeds more than the reverse voltage, very low current can be observed due to net movement of electron in the conduction band towards the potential drop. When the light is illuminated on the sample, large current can be observed due to increase of the number of free electron in the conduction. To cause this electron excitation to the conduction band, the light that strikes the semiconductor must need a minimum energy. Therefore, illumination of right wavelength is important to observe a large current enhancement compared to the dark condition. In our experiment, the illuminated light shows a considerable improvement over the dark current due to high mobility of electrons and holes and less trap states in surfactant free PbSe quantum dots. Since the number of new electron-hole pairs generated during the light illumination is proportional to the number of incident photons, higher intensity will generate higher current.

5.2.3. Temperature Dependent Conductivity

According to the Fig 4.18, the electron mobility of the nanocrystals was changed with changing temperature. Four distinct regions in the graph were observed at different temperature regions indicating four different transport mechanisms of nanocrystals. When lowering the temperature of the sample, each mechanism becomes more prominent within that temperature range. These mechanisms are independent of each other and

largely depend on the exchange coupling energy between the nanocrystals and the Coulomb energy of the nanocrystal array. When temperature was reduced from room temperature to 250K, the graph shows a linear drop of $ln\sigma$ accordance with Arrhenius-type behavior, *i.e.* $ln\sigma = -(E_a/k_BT) + ln\sigma_o$; where E_a is the activation energy. According to the graph, activation energy for surfactant free PbSe is $E_a = 52.2meV$. This thermally activated conductance is due to the effect of electron-electron repulsion (Coulomb blockage).[4,39] When temperature was reduced further from 250K to 150K, the graph shows a drop of $ln\sigma$ accordance with hopping mechanism (*i.e.* $ln\sigma = -(T_o/T)^P + ln\sigma_o$). According to the graph, there are two hopping mechanisms which can be identified. From 250K to 240K the $ln\sigma$ reduced in accordance with $P=0.95$ while from 240K to 200K the $ln\sigma$ reduced accordance with $P=0.5$. When $P=0.5$ the hopping regime can be identified as Efros-Shklovskii variable range hopping (ES-VRH). When temperature was reduced from 200K to 110K, the drop becomes almost zero due to diminishing of hopping mechanism. In this region, the tunneling mechanism becomes prominent over other competing mechanisms. Since tunneling contributes weakly to the conductance, it is been neglected in the region from 300K to 200K. There is a slight increment of electron conduction in the temperature below 110K. This could be due to semiconductor to metal transition in surfactant free quantum dots, which occurs as a result of entering into strong coupling regime at the low temperatures.

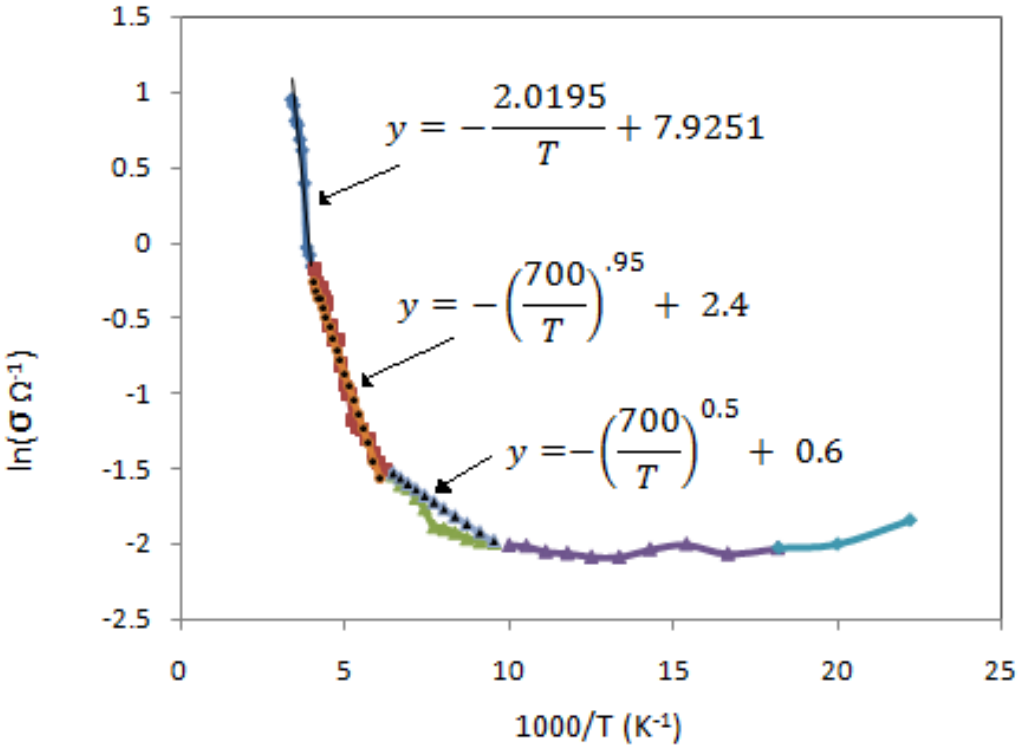

Fig. 5.1: The graph shows the conductivity σ (in log scale) versus the inverse of T for PbSe QDs samples deposited by LASP technique comparison with the calculated curves.

5.3. Fabrication of PbSe QDs/P3HT Hybrid Structure by LA Co-Deposition

The main advantage of the Laser-Assisted Co-Deposition technique is co-deposition of the surfactant free quantum dots and the polymer. This provides a way to deposit the hybrid composite structures with uniform coverage. The XRD and TEM results in section 4.3 confirm the formation of PbSe QDs/ P3HT polymer hybrid composite by laser assisted co-deposition technique. The photo-generated current measurements of the deposited PbSe QDs/P3HT composites confirm the generation and dissociation of excitons during the light illumination. In this PbSe QDs/P3HT composite, as confirmed in section 4.1 and 4.2, both PbSe QDs and the P3HT polymer absorb visible

and NIR spectrum and generate electrons and holes which eventually separate at each PbSe QD- P3HT interface. The mechanism taking place in this heterostructure can be explained by using a simplified band diagram as shown in Fig 5.2.

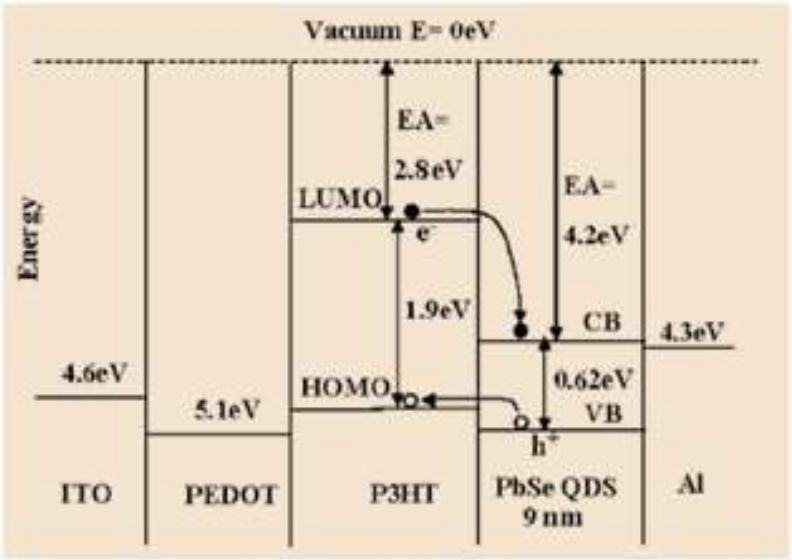

Fig. 5.2: Energy level diagram of the PbSe QDs/P3HT based hybrid composite.

The illustrated band-gap energy of PbSe NQDs and P3HT was estimated from the lowest excitonic absorption peak in Fig. 4.6 and Fig. 4.24, respectively. It has been assumed that the conduction and valence bands in the nanoparticle shift by the same energies relative to the bulk material due to the nearly equal effective masses for holes and electrons in PbSe.[50] Since the lowest unoccupied molecular orbital (LUMO) and the highest occupied molecular orbital (HOMO) of P3HT lie above the conduction-band (CB) and valence-band (VB) edges of PbSe NQDs (9.5nm), respectively, the PbSe NQD/P3HT composite forms a type-II heterojunction at the nanocrystal/polymer interface. Charge separation is therefore favored between the high electron-affinity

inorganic semiconductors and the low ionization potential polymer.[51] The ionization potential energy of PEDOT is close to that of P3HT to minimize the hole extraction barrier at the anode surface by work function of ITO at the interface.

REFERENCES

1. H. Gleiter, Progress *in Materials Science 33:4* (1990).

2. E. Anisimovasa, A. Matulisa and F.M. Peetersb, *Proceedings of the 12th International Symposium UFPS, Vol. 107, page 187-192* (2004).

3. Yu. P. Rakovich, J. F. Donegan, S. A. Filonovich, M. J. M. Gomes, D. V. Talapin, A. L. Rogach, A. Eychmüller, *Physica E , 17, 99-100*.2003.

4. G. A. Prinz and J. H. Hathaway, *Physics Today **48** (4), 24* (1995)*;* P. Grünberg, *Physics Today **54**(5), 31* (2001); G. A. Prinz, *Science **282**, 1660* (1998).

5. D. Vanmaekelbergh and P. Liljeroth, *Chem. Soc. Rev. 34. Page 299-312* (2005).

6. A. S. Edelstein and R. C. Cammarata, *Nanomaterilas: Synthesis, Properties and Applications.*

7. V. I. Klimov. *J. Phys. Chem. B**,** 104, 6112-6123* (2000).

8. N. Peyghambarian, S. W. Koch, and A. Mysrowicz. *Introduction to Semiconductor Optics*. Englewood Cliffs: Prentice Hall, (1993).

9. A. Marti, G. L. Araujo, *Sol. Energy Mater. Sol. Cells, Vol.43, 203-222* (1996).

10. R. D. Schaller, M. A. Petruska, and V. I. Klimov, *Applied Phys. Lett. 87, 253102*(2005).

11. C.A. Leatherdale, C.R. Kagan, N.Y. Morgan, S.A. Empedocles,M.A. Kastner, and M.G. Bawendi, *Phys. Rev. B 62, 2669* (2000).

12. A. Franceschetti and A. Zunger, *Phys. Rev. Vol 63, 153304* (2000).

13. M.Tamborra, M. Striccoli, R. Comparelli, M. L. Curri, A. Petrella and A. Agostiano, *Nanotechnology, Vol. 15, S240–S244* (2004).

14. S. J. Kim, W. J. Kim, Y. Sahoo, A. N. Cartwright and P. N. Prasad, *App. Phys. Lett, 92, 031107* (2008).

15. J.H. Warner, A. R. Watt, E. Thomsen, N. Heckenberg, P. Meredith, and H. Rubinsztein-Dunlop, *J. Phys. Chem. B., Vol 109, Page 9001-9005* (2005).

16. N. Greenham, X. Peng, and A. Alivisatos, *Phys. Rev. B, 54, 17628* (1996).

17. F. Chang, S. Musikin, L. Bakueva, L. Levina, M. Hines, P. Cry, E. Sargent, *Appl. Phys. Lett., Vol 84, Page 4295* (2004).

18. A. Soloviev, D. Ivanov, R. Tufeu, A. V. Kanaev, *J. Materials Science Letters, Vol. 20, Number 10, Page 905-906* (2001).

19. Z.C. Xu, C. M.Shen, C. W. Xiao, T.Z. Yang, H.R. Zhang, J.Q. Li, H.L. Li and H.J. Gao, *Nanotechnology 18 115608, Page 5* (2007).

20. E. V. Shlyakhova, N. F. Yudanov, A. V. Okotrub, Yu. V. Shubin, L. I. Yudanova and L. G. Bulusheva, *Journal of Inorganic Materials, Vol. 44, No. 3, Page 213-218* (2008).

21. T. Tani, L. Mädler and S. E. Pratsinis, *Journal of Nanoparticle Research, Vol. 4, No. 4, Page 337-343* (2002).

22. H. Maskrot, N. H. Boime, Y. Leconte, K. Jursikova, C. Reynaud and J. Vicens, *Journal of Nanoparticle Research, Vol. 8, No. 3-4, Page 351-360* (2006).

23. M. Eslamin, M. Ahamed and N. Ashgiz, *Nanotecnology, Vol 17, Page 1674-1685* (2006).

24. T. Kyprianidou-Leodidou, W. Caseri, and V. Suter. *J. Phys. Chem. 98:8992* (1994).

25. C.C. Wang, Z. Zhang, and J.Y. Ying. *Nanostructured Mater. 9:583* (1997).

26. T. Gacoin, L. Malier, and J.P. Boilot. *Chem. Mater. 9:1502* (1997).

27. V. Sankaran, J. Yue, R.E. Cahen, R.R. Schrock, and R.J. Silbey. *Chem. Mater. 5:1133* (1993).

28. Y. Yuan, J. Fendler, and I. Cabasso. *Chem. Mater*. 4:312 (1992).

29. B. L. Justus, R.J. Tonucci, and A.D. Berry. *Appl. Phys. Lett*. 61:3151 (1992).

30. S.A. Majetich, and A.C. Canter. *J. Phys. Chem*. 97:8727 (1993).

31. M. Liu, M.L. Zhou, L. H. Zhai, D.M. Liu, X. Gao and W. Liu., *Physica C* 386, 366 (2003).

32. N. Herlin, X. Armand, E. Musset, H. Martinengo, M. Luce and M. Cauchetier., *J. Eur. Ceram. Soc.* 16, 1063 (1996).

33. A. Muller, N. Herlin-Boime, F. Tenegal, X. Armand, F. Berger, A. M. Flank, R. Dez, K. Muller, J.Bill and F. Aldinger., *J.Eur Ceram. Soc.* 23, 37 (2003).

34. P. S. Patil., *Mater. Chem. Phys*. 59, 185 (1999).

35. C. P. Poole and F. J. Owens, *Introduction to Nanotechnology, Page 194-19, Page 90-91, Page 232.*

36. S. Ostapenko, I. Tarasov, J. P. Kaljas, C. Haessler and E. U. Reisner, *Semicond. Sci. Technol. Vol. 15, Page 840-848* (2000).

37. E. Bundgaard, S. E. Shaheen, F. C. Kerbs, D. S. Ginley,. *Solar Energy Materials & Solar Cells, Vol 91, Page 1631-1637* (2007).

38. D. C. Jian, T. Zhu, G. Paradee, S. Ashok, *Appl. Phys. Lett. Vol 88, 183111*(2006).

39. E. Sargent, Method of making quantum dots. US Patent Application: 20070174939, (2007).

40. H. E. Remero and M. Drndic, *Appl. Rev. Lett. Vol 95, 156801* (2005).

41. J. P. Clifford, K. W. Johnston, L. Levina, and E. H. Sargent, *Appl. Phys. Lett. Vol 91, 253117* (2007).

42. S. Gunes, K. P. Fritz, H. Neugebauer, N. S. Sariciftci, S. Kumar, and G. D. Scholes, *Solar Energy Materials & Solar Cells, Vol 91, Page 420-423* (2007).

43. V. A. Tkachenko, Z. D. Kvon ,O. A. Tkachenko, D. G. Baksheev, O. Estibals,and J. C. Portal, *Physica E: Low-dimensional Systems and Nanostructures, Volume 21, Issues 2-4, Pages 469-473* (2004).

44. G. Markovich, C. P. Collier, H. C. Henriches, F. Remacle, R. D. Levine and J. R. Heath, *Acc. Chem. Res. 32, 415* (1999).

45. F. Remacle, *J. Phys. Chem. A 104, 4739* (2000).

46. D. Cui, J. Xu, T. Zhu, G. Paradee, and S. Ashok, *Appl. Phys. Lett. Vol. 88, page 183111*(2006).

47. N. Y. Morgan et al., *Phys. Rev. B 66, 075339* (2002).

48. R. Parthasarathy, X. M. Lin, and H. M. Jaeger, *Phys. Rev. Letts. 87, 186807* (2001).

49. B. L. Wehernberg, D. Y. Jaisen Ma and P. Guyot-Sionnest, *J. Phys. Chem. B 109, 20192* (2005).

50. C. T. Black, C. B. Murray, R. L. Sandstrom, and S. Sun, *Science 290, 1131* (2000).

51. P. Capper, *Narrow Gap II-VI Compounds for Optoelectronic and Electromagnetic Applications, 1st ed., edited ,Springer, Berlin,* (1997).

52. J. Nozik, *Physica E (Amsterdam) 14, 115* (2002).

53. C. B. Murray, S. Sun, W. Gaschler, H. Doyle, T. A. Betley and C. R. Kagan, *Organic electronics, Vol. 45, No. 1* (2001).

54. S.Witanchchi, G. Dedigamuwa and P. Mukherjee, *Journal of Material Research, vol 22, page 649-654*, (2007).

ABOUT THE AUTHOR

Gayan Dedigamuwa was born and raised in Sri Lanka. He attended the University of Kelaniya as an undergraduate where he specialized in Physics. He joined the University of South Florida, Department of Physics in the spring of 2003 and started working as a Research Assistant in Laboratory for Advanced Materials Sciences and Technology (LAMSAT) under Prof. Sarath Witanachchi. In 2005, he finished his Masters of Science degree and continued toward his PhD. He has published several scientific papers on thin film fabrication and surfactant free QD film fabrication by using Laser Assisted Spray process developed in his laboratory. In summer 2008, he was awarded the Fred L. and Helen M. Tharp Physics Graduate Scholarship. In April 2009, he joined the United Solar Ovonic located in Auburn Hills, MI as a Process Engineer/Physicist. He currently resides in Rochester Hills, MI with his wife, Nilusha and lovely little daughter, Luhansa.